CONTENTS

CHAPTER 1

INTRODUCTION

1.1 Motivation and Objectives of This Thesis

During the last decades, MEMS technology has undergone rapid development, leading to the successful fabrication of miniaturized mechanical structures integrated with microelectronic components. Accelerometers are in great demand for specific applications ranging from guidance and stabilization of spacecrafts to research on vibrations of Parkinson patients' fingers. Generally, it is desirable that accelerometers exhibit a linear response and a high signal-to-noise ratio. Among the many technological alternatives available, piezoresistive accelerometers are noteworthy. They suffer from dependence on temperature, but have a DC response, simple readout circuits, and are capable of high sensitivity and reliability. In addition, this low-cost technology is suitable for multi degrees-of-freedom accelerometers which are high in demand in many applications.

In order to commercialize MEMS products effectively, one of the key factors is the streamlining of the design process. The design flow must correctly address design performance specifications prior to fabrication. However, CAD tools are still scarce and poorly integrated when it comes to MEMS design. One of the goals of this thesis is to outline a fast design flow in order to reach multiple specified performance targets in a reasonable time frame. This is achieved by leveraging the best features of two radically different simulation tools: Berkeley SUGAR, which is an open-source academic effort, and ANSYS, which is a commercial product.

There is an extensive research on silicon piezoresistive accelerometer to improve its performance and further miniaturization. However, a comprehensive analysis considering the impact of many parameters, such as doping concentration, temperature, noises, and power consumption on the sensitivity and resolution has not been reported. The optimization process for the 3-DOF micro accelerometer

which is based on these considerations has been proposed in this thesis in order to enhance the sensitivity and resolution.

1.2 Overview of MEMS

Microelectromechanical systems (MEMS) are collection of micro sensors and actuators that sense the environment and react to changes in that environment [46]. They also include the control circuit and the packaging. MEMS may also need micro-power supply and micro signal processing units. MEMS make the system faster, cheaper, more reliable, and capable of integrating more complex functions [5].

In the beginning of 1990s, MEMS appeared with the development of integrated circuit (IC) fabrication processes. In MEMS, sensors, actuators, and control functions are co-fabricated in silicon. The blooming of MEMS research has been achieved under the strong promotions from both government and industries. Beside some less integrated MEMS devices such as micro-accelerometers, inkjet printer head, micro-mirrors for projection, etc have been in commercialization; more and more complex MEMS devices have been proposed and applied in such varied fields as microfluidics, aerospace, biomedical, chemical analysis, wireless communications, data storage, display, optics, etc.

At the end of 1990s, most of MEMS transducers were fabricated by bulk micromachining, surface micromachining, and LIthography, GAlvanoforming, moulding (LIGA) processes [7]. Not only silicon but some more materials have been utilized for MEMS. Further more, three-dimensional micro-fabrication processes have been applied due to specific application requirements (e.g., biomedical devices) and higher output power micro-actuators.

Micro-machined inertial sensors that consist of accelerometers and gyroscopes have a significant percentage of silicon based sensors. The accelerometer has got the second largest sales volume after pressure sensor [56]. Accelerometer can be found mainly in automotive industry [62], biomedical application [30], household electronics [69], robotics, vibration analysis, navigation system [59], and so on.

Various kinds of accelerometer have increased based on different principles such as capacitive, piezoresistive, piezoelectric, and other sensing ones [22]. The concept of accelerometer is not new but the demand from commerce has motivated continuous researches in this kind of sensor in order to minimize the size and improve its performance.

1.3 Reviews on Silicon Micro Accelerometers

Silicon acceleration sensors often consist of a proof mass which is suspended to a reference frame by spring elements. Accelerations cause the proof mass to deflect and the deflection of the mass is proportional to the acceleration. This deflection can be measured in several ways, e.g. capacitively by measuring a change in capacitance between the proof mass and additional electrodes or piezoresistively by integrating strain gauges in the spring element. The bulk micromachined techniques have been utilized to obtain large sensitivity and low noise.
However, surface micromachined is more attractive because of the easy integration with electronic circuits and no need of using wafer bonding as that of bulk micromachining. Recently, some structures have been proposed which combine bulk and surface micromachining to obtain a large proof mass in a single wafer process.
To classify the accelerometer, we can use several ways such as mechanical or electrical, active or passive, deflection or null-balance accelerometers, etc.
This thesis reviewed following type of the accelerometers [67]:

- Electromechanical
- Piezoelectric
- Piezoresistive
- Capacitive
- Resonant accelerometer

Depending on the principles of operations, these accelerometers have their own subclasses.

1.3.1 Electromechanical Accelerometers

There are a number of different electromechanical accelerometers: coil-and-magnetic types, induction types, etc. In these sensors, a proof mass is kept very close to a neutral position by sensing the deflection and feeding back the effect of this deflection. A corresponding magnetic force is generated to eliminate the motion of the proof mass deflected from the neutral position, thus restoring this position like the way a mechanical spring in a conventional accelerometer would do. This approach can offer a better linearity and elimination of hysteresis effects when compare to the mechanical springs [21].

1.3.2 Piezoelectric Accelerometers

Piezoelectric accelerometers are suitable for high-frequency applications and shock measurement. They can offer large output signals, small sizes and no need of external power sources [53]. These sensors utilize a proof mass in direct contact with the piezoelectric component as shown in Fig 1. 1. There are two common piezoelectric crystals are lead- zirconate titanate ceramic (PZT) and crystalline quartz. When an acceleration is applied to the accelerometer, the piezoelectric component experiences a varying force excitation (F = ma), causing a proportional electric charge q to be developed across it. The disadvantage of this kind of accelerometer is that it has no DC response.

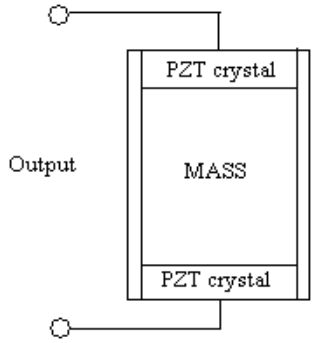

Fig 1. 1 A compression type piezoelectric accelerometer arrangement.

1.3.3 Piezoresistive Accelerometers

Piezoresistive accelerometers (see Fig 1. 2) have held a large percentage of solid-state sensors [79],[83]. The reason is that they have a DC response, simple readout circuits, and are capable of high sensitivity and reliability even if they suffer from dependence on temperature. In addition, it is a low-cost technology suitable for

high-volume production. The operational principle is based on piezoresistive effect where the conductivity would change due to an applied strain. Piezoresistive accelerometers are useful for static acceleration measurements and vibration analysis at low frequencies. The sensing elements are piezoresistors which forms Wheatstone bridge to obtain the voltage output without extra electronic circuits.

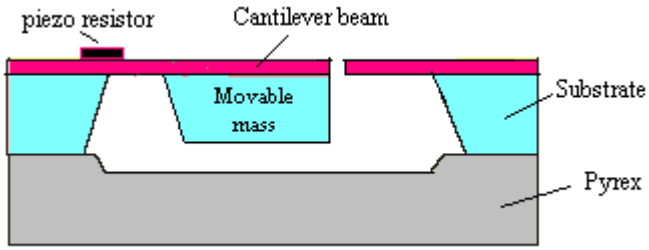

Fig 1. 2 Piezoresistive acceleration sensor.

1.3.4 Capacitive Accelerometers

Capacitive accelerometers are based on the principle of the change of capacitance in proportion to applied acceleration. Depending on the operation principles and external circuits they can be broadly classified as electrostatic-force-feedback accelerometers, and differential-capacitance accelerometers (see Fig 1. 3) [37].

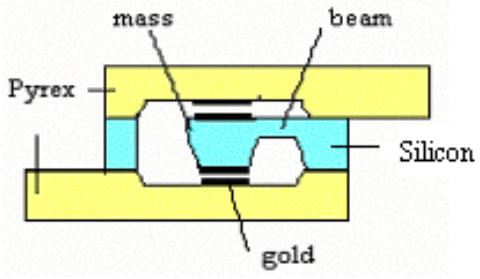

Fig 1. 3 Capacitive measurement of acceleration.

The proof mass carries an electrode placed in opposition to base-fixed electrodes that define variable capacitors. By applying acceleration, the seismic mass of the accelerometer is deflected, leading to capacitive changes. These kinds of accelerometer require wire connecting to external circuits which in turn experience

parasitic capacitances. The advantages of capacitive sensors are high sensitivity, low power consumption and low temperature dependence.

1.3.5 Resonant Accelerometers

The structures of resonant accelerometers are quite different from other sensors (see Fig 1. 4). The proof mass is suspended by stiff beam suspension to prevent large deflection due to large acceleration. By applying acceleration, the proof mass changes the strain in the attached resonators, leading a shift in those resonant frequencies. The frequency shift is then detected by either piezoresistive, capacitive or optical readout methods and the output can be measured easily by digital counters.

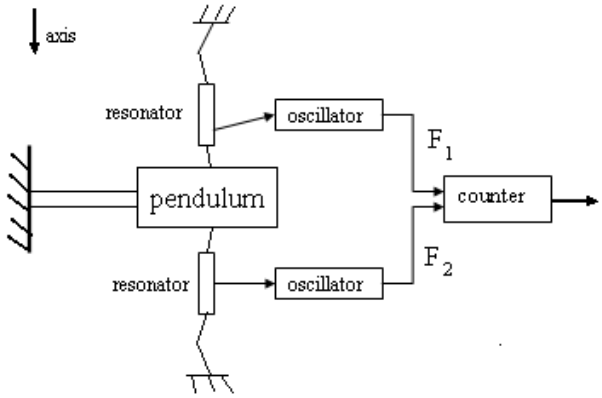

Fig 1. 4 Resonant accelerometer

Resonant accelerometers provide high sensitivity and frequency output. However, the use of complex circuit containing oscillator is a competitive approach for high precision sensing in long life time.

1.4 Reviews on Development of Multi-Axis Accelerometers

As we know, the realistic applications create a huge motivation for the widely research of MEMS based sensors, especially accelerometer. In this modern world, applications require new sensors with smaller size and higher performance [1],[12],[57]. In practice, there are rare researches which can bring out an efficient and comprehensive methodology for accelerometer designs.

T.Mineta et al [68] presents design, fabrication, and calibration of a 3-DOF capacitive acceleration which has uniform sensitivities to three axes. However, this sensor is more complex than piezoresistive one and is not economical to fabricate with MEMS technology.

In 2004, Dzung Viet Dao et al [16] presented the characterization of nanowire p-type Si piezoresistor, as well as the design of an ultra small 3-DOF accelerometer utilizing the nanowire Si piezoresistor. Silicon nanowire piezoresistor could increase the longitudinal piezoresistance coefficient $\pi_{l\ [011]}$ of the Si nanowire piezoresistor up to 60% with a decrease in the cross sectional area, while transverse piezoresistance coefficient $\pi_{t\ [011]}$ decreased with an increase in the aspect ratio of the cross section. Thus, the sensitivity of the sensor would be enhanced.

In 1996, Shin-ogi et al [60] presented an acceleration sensor fabricated on a piezoresistive element with other necessary circuits and runs parallel to the direction of acceleration. The accelerometer utilizes lateral detection to obtain good sensitivity and small size. The built-in amplifier has been formed with a narrow width, and confirmed operation.

In 1998, Kruglick E.J.J et al [40] presented a design, fabrication, and testing of multi-axis CMOS piezoresistive accelerometers. The operation principle is based on the piezoresistive behavior of the gate polysilicon in standard CMOS (see Fig 1. 5). Built-in amplifiers were designed and built on chip and have been characterized.

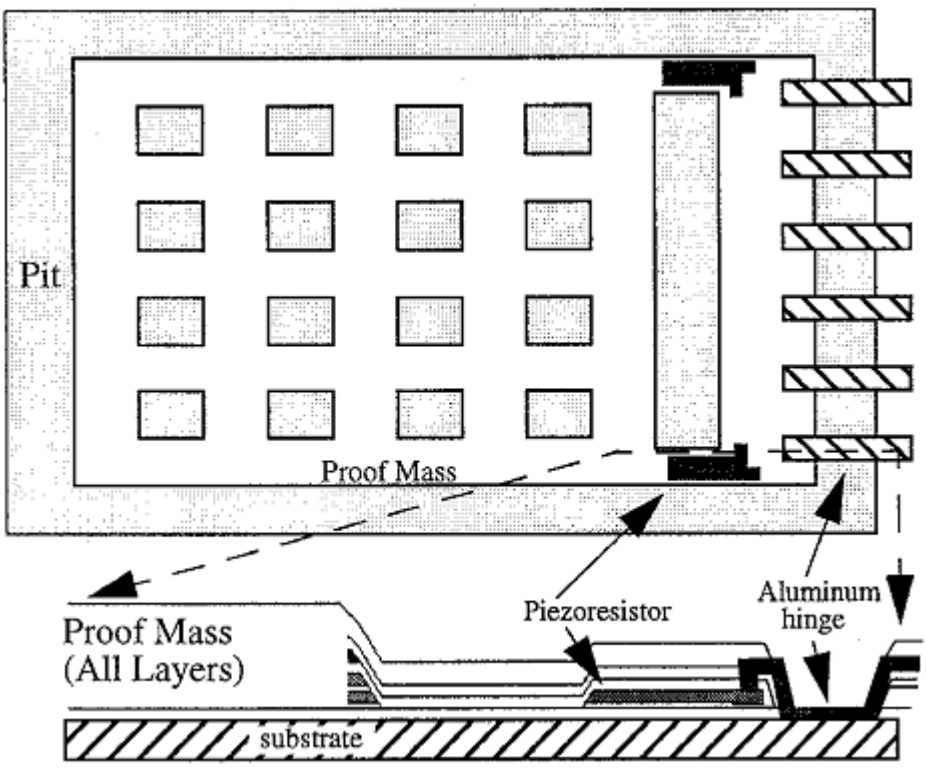

Fig 1. 5 Overview of accelerometer design.

In 2006, Dzung Viet Dao et al [17] presented the development of a dual axis convective accelerometer (see Fig 1. 6). The working principle of this sensor is based on the convective heat transfer and thermo-resistive effect of lightly-doped silicon. This accelerometer utilizes novel structures of the sensing element which can reduce 93% of thermal-induced stress. Instead of the seismic mass, the operation of the accelerometer is based on the movement of a hot tiny fluid bubble from a heater in a hermetic chamber. Thus, it can overcome the disadvantages of the ordinary "mechanical" accelerometers such as low shock resistance and complex fabrication process.

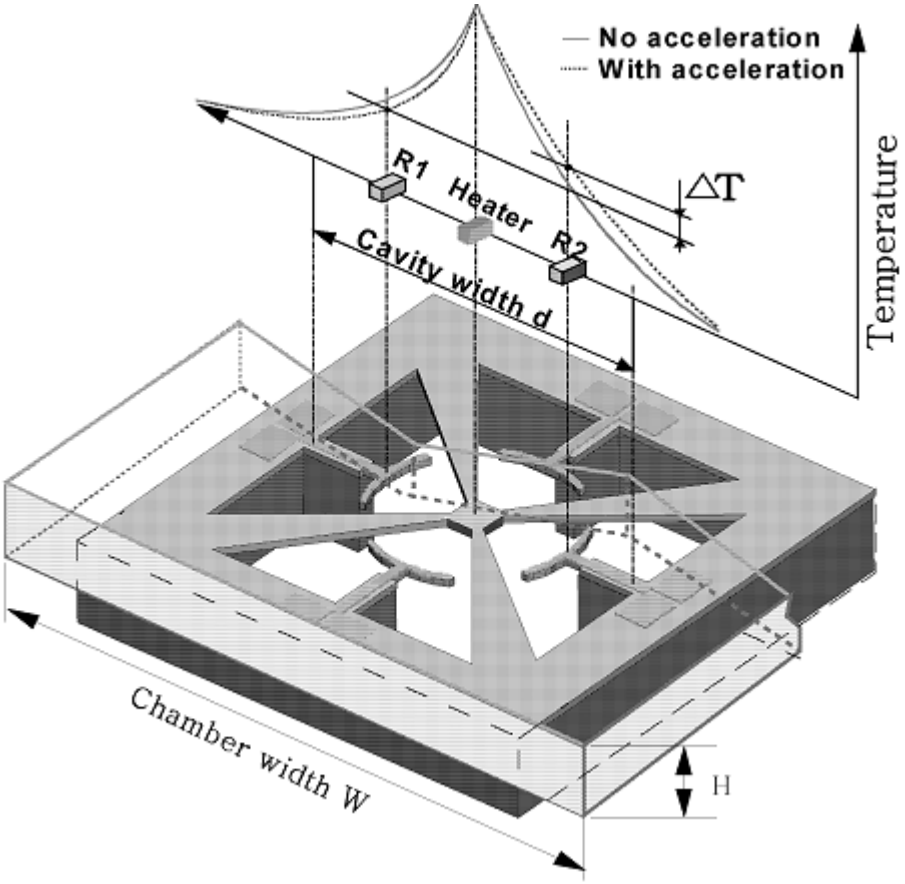

Fig 1. 6 Schematic view shows working principle of the sensor

1.5 Reviews on Performance Optimization of Multi-Axis Accelerometers

In fact, there are lacks of researches focusing to optimize the multi-axis accelerometer's performance.

In 1997, J. Ramos [32] presented a lateral capacitive structure that could enhance the sensitivity by width optimization. An optimum assignment is found for the distribution of area in surface micromachined lateral capacitive accelerometers between stationary and moving of the sensor.

In 2000, Harkey J.A et al [27] presented 1/f noise considerations for the design and process optimization of piezoresistive cantilevers. In this paper, data was shown which validates the Hooge model for 1/f noise in piezoresistive cantilevers. From equations for the Hooge noise, Johnson noise, and sensitivity, an expression was derived to predict force resolution of a piezoresistive cantilever based on its geometry and processing. Using this expression, an optimization analysis was performed.

In 2004, Sankar et al [58] presents temperature drift analysis of silicon micromachined peizoresistive accelerometer. The result is quite simple in terms of the variation of the output voltage at different accelerations and temperatures. The optimization targets have not mentioned in this paper yet.

In 2006, Maximillian Perez and Andrei M. Shkel [44] focused on the detailed analysis of a single sensor of such a series and evaluates the performance trade-offs. This work provides tools required to characterize and demonstrate the capabilities of transmission-type intrinsic Fabry-Perot accelerometers. This sensor is more complex than piezoresistive one and it can only sense acceleration in one dimension.

In 2006, C Pramanik et al [4] presented the design optimization of high performance conventional silicon-based pressure sensors on flat diaphragms for low-pressure biomedical applications have been achieved by optimizing the doping concentration and the geometry of the piezoresistors. A new figure of merit called the performance factor (PF) is defined as the ratio of the product of sensor sensitivity (S) and sensor signal-to-noise ratio (SNR) to the temperature coefficient of piezoresistance (TCPR). PF has been introduced as a quantitative index of the overall performance of the pressure sensor for low-range biomedical applications.

In 2002, Rodjegard H. et al [55] presented analytical models for three axis accelerometers based on four seismic masses. The models make it possible to better understand and to predict the behavior of these accelerometers. Cross-axis sensitivity, resolution, frequency response and direction dependence are investigated for variety of sensing element structures and readout methods. With the maximum sensitivity direction of the individual sensing elements inclined 35.3^{o} with respect to the chip surface the properties become direction independent, i.e. identical resolution and frequency response in all directions.

In 2005, Zhang Y. et al [80] presented a hierarchical MEMS synthesis and optimization architecture has been developed for MEMS design automation. The architecture integrates an object-oriented component library with a MEMS simulation tool and two levels of optimization: global genetic algorithms and local gradient-based refinement. Surface micro-machined suspended resonators are used as an example to introduce the hierarchical MEMS synthesis and optimization process.

In 2007, Xin Zhao et al [85] presented a novel MEMS design methodology that combined with top-down and bottom-up conceptions. Besides, Virtual Fabrication Process and Virtual Operation are also utilized in the design process which could exhibit 3D realistic image and real-time animation of microfluidic device. IP (Intellectual Property) library is established to support hybrid top-down and bottom-up design notions. Also an integrated MEMS CAD composed of these design ideas is developed. However, the optimization considerations have not been concerned in this method yet and it seemed to be time-consuming works.

1.6 Content of the Thesis

The thesis consists of 5 chapters.

Chapter 1 gives a thorough review on motivation of the thesis, silicon accelerometers, multi-axis acceleration sensors, and optimization problems in MEMS sensor's designs.

Chapter 2 presents fundamental principle of open loop accelerometer and the piezoresistance effect in silicon. This kind of phenomena is later used for designing of the 3-DOF acceleration sensor. Principles of FEM and MNA methods are also described in order to perform structure optimum in the next chapter.

In Chapter 3, a hierarchical MEMS design synthesis and optimization process are developed for and validated by the design of a specific MEMS accelerometer. The iterative synthesis design is largely based on the use of a MNA tool called SUGAR in order to meet multiple design specifications. After some human interactions, the design is brought to FEM software such as ANSYS for final validation and further optimization (such as placement of the piezoresistors in our case study).

The structural analysis, a very important step that can provide the stress distribution on the beams, is presented in the next section. The chapter 3 also describes more details of the design that multi-physic coupling for thermal–mechanical–piezoresistive fields was established in order to evaluate the sensor characteristics. The design of the photo masks is mentioned at last.

Chapter 4 presents the whole process to fabricate the 3-DOF MEMS based accelerometers. After that, static and dynamic measurements have been performed on these sensors. The Allan variance method was combined with the Power spectrum density (PSD) to specify the error parameters of the sensor and electronic circuit.

Chapter 5 presents the design optimization for a high performance 3-DOF silicon accelerometer. The target is to achieve the high sensitivity or high resolution. The problem has been solved based on considerations of junction depth, the doping concentration of the piezoresistor, the noise, and the power consumption. The result shows that the sensitivity of the optimized accelerometer is improved while the resolution is small compared to previous experimental results.

CHAPTER 2

TRENDS IN DESIGN CONCEPTS FOR MEMS: APPLIED FOR PIEZORESISTIVE ACCELEROMETER

2.1 Open-loop Accelerometers

The operational principle of an accelerometer is based on the Newton's second law. Upon acceleration, the proof mass (seismic mass) that is anchored on the frame by mechanical suspensions experiences an inertial force F (= -ma) causing a deflection of the proof mass, where *a* is the frame acceleration. Under certain conditions, the displacement is proportional to the input acceleration:

$$x = \frac{ma}{k} \tag{2.1}$$

where *k* is the spring constant of the suspension. The displacement can be detected and converted into an electrical signal by several sensing techniques. This simple principle underlies the operation of all accelerometers.

From a system point of view, there are two major classes of silicon micro-accelerometers: open-loop and force-balanced accelerometers [48]. In open-loop accelerometer design, the suspended proof mass displaces from its neutral position and the displacement is measured either piezoresistively or capacitively. In force-balance accelerometer design, a feedback force, typically an electrostatic force, is applied onto the proof mass to counteract the displacement caused by the inertial force. Hence, the proof mass is virtually stationary relative to the frame. The output signal is proportional to the feedback signal.

In this section, the behavior of only open-loop accelerometers will be described and its steady state, frequency, and transition response will be studied analytically. The force-balanced accelerometers are not the subject of this thesis. The reason is that this thesis intends to focus to the piezoresistive sensing method which is applied mainly for the open-loop accelerometer type, whereas in the force balanced one the capacitive sensing method is needed to be used.

An open-loop accelerometer can be modeled as a proof mass suspended elastically on a frame, as shown in Fig 2. 1. The frame is attached to the object whose acceleration is to be measured. The proof mass moves from its neutral position relative to the frame when the frame starts to accelerate. For a given acceleration, the proof mass displacement is determined by the mechanical suspension and the damping.

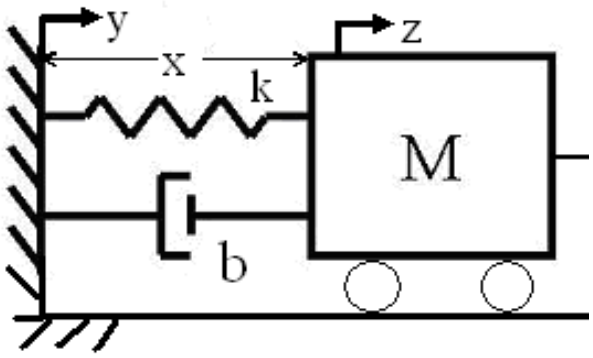

Fig 2. 1 Model of the open loop accelerometer

As shown in Fig 2. 1, y and z are the absolute displacement (displacement with respect to the earth) for the frame and the proof mass, respectively. The acceleration y is the quantity of the interest in the measurement of this sensor. Let x be the relative displacement of the proof mass with respect to the frame, its value is the difference between the absolute displacements of the frame and the proof mass, or $x = z - y$.

In the following analysis, the displacement refers to the relative displacement of the proof mass to the frame (x) in one-dimensional problems, unless otherwise specified. In the three dimensional problems, y and z will denote the relative displacements in the remain coordinate axes, y and z, respectively. We also note that the lower cases x, y, and z denote the displacement in the time domain, whereas the upper cases X, Y. and Z are respectively their Laplace transforms in the s-domain.

Let's go back to the one dimensional problem of Fig. 2.1, when the inertial force displaces the proof mass, it also experiences the restoring force from the mechanical spring and the damping force from the viscous damping. Since the proof mass is

usually sealed in the frame, the damping force is proportional to the velocity relative to the frame, rather than to the absolute velocity. The equation of motion of the proof mass can be thus written as:

$$m\frac{d^2z}{dt^2} = -kx - b\frac{dx}{dt} \tag{2.2}$$

where k is the spring constant of the suspension and b is the damping coefficient of the air and any other structural damping (see Fig. 2.1).

Using x=z-y the following equation of motion can be obtained:

$$\frac{d^2x}{dt^2} + \frac{b}{m}\frac{dx}{dt} + \frac{k}{m}x = -\frac{d^2y}{dt^2} = -a(t) \tag{2.3}$$

The negative sign indicates that the displacement of the proof mass is always in the opposite direction of the acceleration. Equation (2.3) can also be re-written as:

$$\frac{d^2x}{dt^2} + 2\xi\omega_n\frac{dx}{dt} + \omega_n^2 x = -\frac{d^2y}{dt^2} \tag{2.4}$$

where $\omega_n = \sqrt{\frac{k}{m}}$ is natural resonant frequency, $\xi = \frac{b}{2m\omega_n}$ is damping factor.

This is the governing equation for an open loop accelerometer relating its proof mass displacement and the input acceleration. The performance of an open-loop accelerometer can be characterized by the natural resonant frequency ω_n and the damping factor ζ. The damping is determined by the viscous liquid or the chamber pressure. For silicon micro accelerometers, gas damping is most commonly used and the damping factor is controlled by the chamber pressure and the gas properties. Critical damping is desired in most designs in order to achieve maximum bandwidth and minimum overshoot and ringing.

The natural resonant frequency is another important parameter in an open loop accelerometer design. It is designed to satisfy the requirements on the sensitivity and the bandwidth. The natural resonant frequency can be measured either dynamically by resonating the accelerometer or statically by measuring the displacement for a given acceleration. From its definition, the natural resonant frequency can be re-written as:

$$\omega_n = \sqrt{\frac{k}{m}} = \sqrt{\frac{a}{x}} \tag{2.5}$$

where a is the acceleration and x is the displacement. Therefore, the natural resonant frequency can be determined conveniently by measuring the displacement due to the gravitational field.

Steady-State Response: For a constant acceleration, the proof mass is stationa1y relative to the frame so that equation (2.4) becomes:

$$\omega_n^2 x = -\frac{d^2 y}{dt^2} = -a \tag{2.6}$$

or

$$x = -\frac{m}{k} a \tag{2.7}$$

The static sensitivity of the accelerometer is shown to be:

$$\frac{x}{a} = \frac{m}{k} = \frac{1}{\omega_n^2} \tag{2.8}$$

Therefore, the proof mass displacement is linearly proportional to the input acceleration in the steady state. The sensitivity is determined by the ratio m/k or the inverse of the square of natural resonant frequency. Hence, the resonance frequency of the structure can be increased by increasing the spring constant and decreasing the proof mass, while the quality factor of the device can be increased by reducing damping and by increasing proof mass and spring constant. Last, the static response of the device can be improved by reducing its resonant frequency.

Fig 2. 2 shows the SIMULINK model of an open loop accelerometer which was derived from the mechanical simulation of the accelerometer presented in Fig 2. 1. This high level model can be utilized to analyze the frequency and transient responses of the sensor.

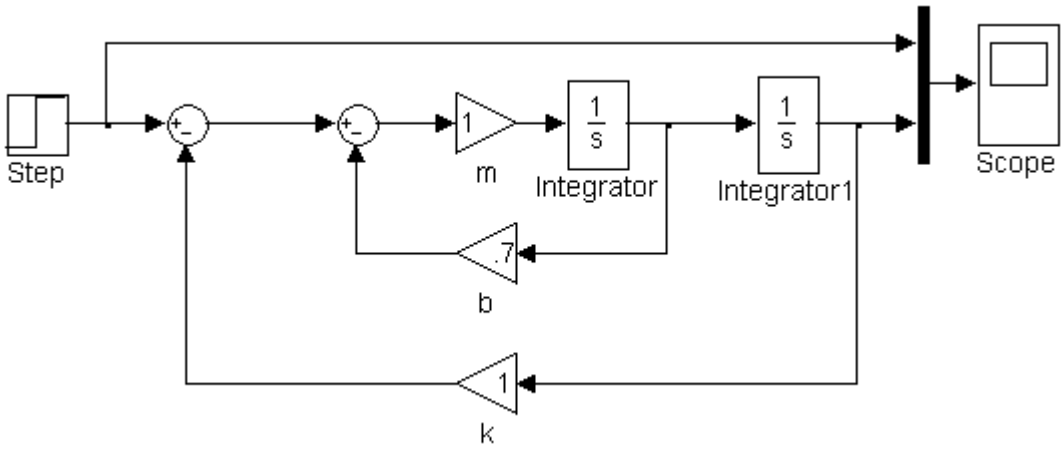

Fig 2. 2 The SIMULINK model of the open-loop accelerometer

Frequency Response: Frequency response is the acceleration response to a sinusoidal excitation. Let the frame be in harmonic motion

$$a(t) = \frac{d^2 y}{dt^2} = -Y\omega^2 \sin \omega t \tag{2.9}$$

Note that magnitude of accelerator is $-Y\omega^2$. The motion governing equation, eq 2.4 becomes:

$$\frac{d^2 x}{dt^2} + 2\xi\omega_n \frac{dx}{dt} + \omega_n^2 x = Y\omega^2 \sin \omega t \tag{2.10}$$

The frequency response can be obtained by solving this equation either in the time domain or in the s-domain using Laplace transforms. To solve it in the time domain, assuming that the initial velocity and displacement are both zero, we can transform equation (2.10) into *s* domain and obtain:

$$X(s) = \frac{Y\omega^3}{\left(s^2 + \omega^2\right)\left(s^2 + 2\xi\omega_n s + \omega_n^2\right)} \tag{2.11}$$

The frequency response in the time domain can be obtained by applying invert Laplace transforms to equation (2.11)

$$x(t) = -\frac{Y\omega^2}{\omega_n^2} \frac{\sin(\omega t - \phi)}{\sqrt{\left(1 - \frac{\omega^2}{\omega_n^2}\right)^2 + \left(2\xi \frac{\omega}{\omega_n}\right)^2}} \tag{2.12}$$

where ϕ is phase lag and:

$$\tan\phi = \frac{2\xi\dfrac{\omega}{\omega_n}}{1-\left(\dfrac{\omega}{\omega_n}\right)^2} \tag{2.13}$$

The sensitivity of an accelerometer can be defined as $S(j\omega)=\dfrac{X(j\omega)}{a(j\omega)}$.

Substituting $j\omega$ for s in equation (2.11), the amplitude response can be plotted with various damping coefficients and is presented in Fig 2. 3(a). It shows that there are big overshoot and ringing for under-damped accelerometers, and the cut-off frequency for over-damped accelerometers is lower than for critically damped accelerometers. The phase lag ϕ can also be plotted for various damping coefficients, as shown in the Fig. 2.3 (b). The experimental result on critical damping control can be found in [72].

At low frequency$(\omega << \omega_n)$, we can obtain $S_0 = -\omega_n^{-2} = -\dfrac{m}{k}$ from equation (2.12), which agrees with the steady state response state (equation 2.7). At high frequency$(\omega >> \omega_n)$, the mechanical spring cannot respond to the high frequency vibration and relax its elastic energy. Therefore, for a given acceleration, the proof mass displacement decrease as the frequency increases. From equation (2.12), we can obtain $S(j\omega)=-\dfrac{\omega}{\omega_n}$ so the slope of the asymptote is $-\dfrac{\omega^2}{\omega_n^2}$ at high frequencies.

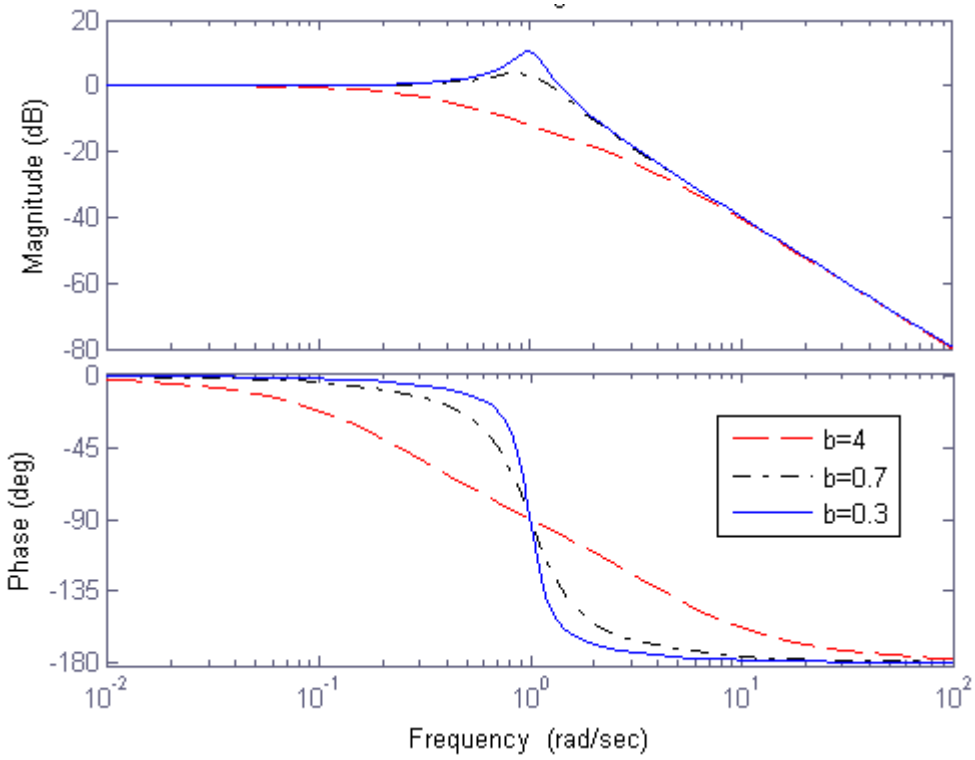

Fig 2. 3 Frequency response with various damping coefficient b

The accelerometer can also be used to measure velocity and displacement in addition to acceleration, although the velocity measurements using accelerometers have very limited applications. The displacement is proportional to the acceleration when the frequency is below a natural resonant frequency, as shown in Fig 2. 3. The accelerometer therefore can be used as a vibro-meter (or displacement meter) for frequencies well above the resonant frequency. From equation (2.12), we find that

$$\frac{x(t)}{Y} = -\frac{m}{k}\frac{\omega^2 \sin(\omega t - \phi)}{\sqrt{\left(1-\frac{\omega^2}{\omega_n^2}\right)^2 + \left(2\xi\frac{\omega}{\omega_n}\right)^2}} \tag{2.14}$$

In other words, the response of the vibrometer is the ratio of the vibration amplitude of the proof mass and the amplitude of applied vibration.

Similar to the analysis for the frequency response, we can obtain the transient response in the time domain:

$$x(t) = \frac{m}{k} Y \left(1 - \frac{e^{-\xi \omega_n t}}{\sqrt{1-\xi^2}} \sin\left(\sqrt{1-\xi^2}\, \omega t + \phi \right) \right) \tag{2.15}$$

where $\phi = \tan^{-1} \dfrac{\sqrt{1-\xi^2}}{\xi}$ is the phase lag.

The transient responses in the time domain with various damping are shown in Fig 2. 4 when the acceleration input is a step function.

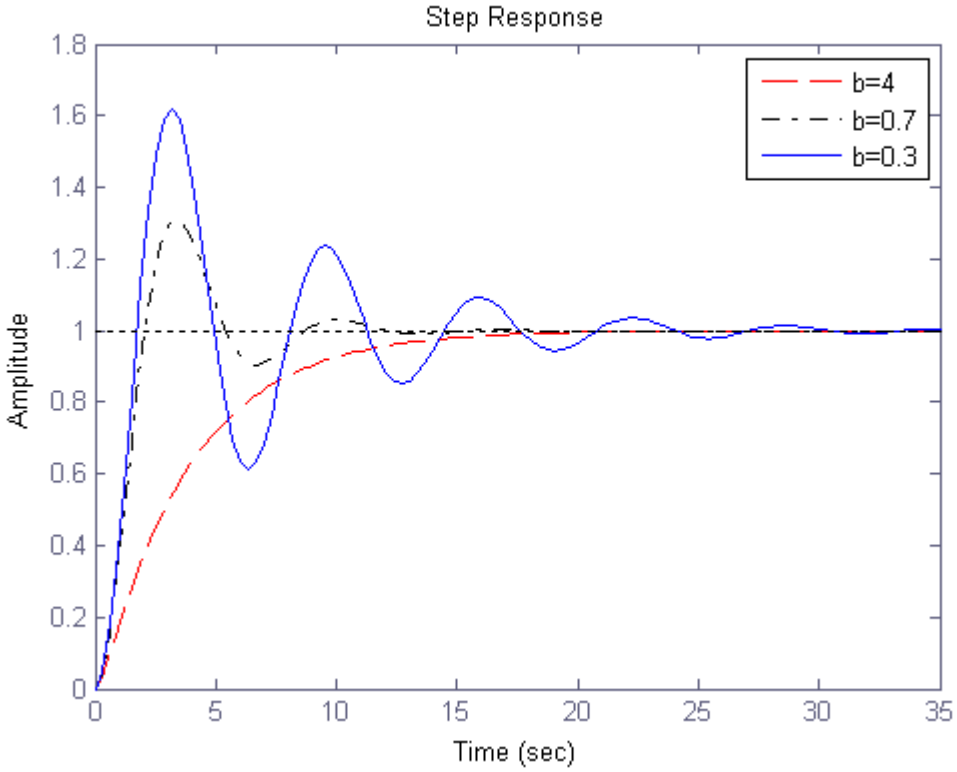

Fig 2. 4 Transient responses of the accelerometer with various damping coefficients

The bandwidth of an open loop accelerometer is set by the ratio of the spring constant and the proof mass, which has to compromise with the sensitivity.

2.2 Piezoresistive Accelerometer

Piezoresistive accelerometer is a typically open-loop system that utilizes the material advance of silicon. Silicon owns brittle mechanical characteristics to become a good material for MEMS devices [65][75]. This thesis focuses to single

crystal silicon piezoresistive accelerometer. Therefore it is meaningful to give an overview of the mechanical properties of silicon in the single crystal state.

Apart from using the excellent mechanical properties of silicon for the accelerometer structure, another interesting property of this material, the piezoresistive effect is also utilized for detecting the deformation of this structure from which acceleration can be derived [46]. Therefore, in this section a brief description of this piezoresistive effect of silicon will also be presented.

2.2.1. Mechanical properties of single crystal silicon

Silicon has proved the powerful advantage in mechanical sensors by its mechanical properties. Table 2. 1 shows some mechanical properties of single crystal silicon and some other materials. In this table, the Young's modulus of silicon is nearly equal to that of stainless steel but the mass density is three times smaller. Silicon is also twice times harder than iron and most common glasses. Further more, its tensile yield is quite large, so that it is really suitable for growth of large single crystals [75].

Table 2. 1 Comparing mechanical properties among several materials in Ref. [18] which are extracted from [Julian W. Gardner, 1994]

	Mass density (10^3 kg.m^{-3})	Yield strength (GPa)	Knoop hardness (10^9 kg/m^2)	Young's modulus (GPa)	Thermal Expansion (10^{-6}/^{o}C)
Si	2330	7	0.85	170*	2.33
SiO_2	2500	8.4	0.82	73	0.55
Si_3N_4	3100	14	3.48	385	0.8
SiC	3200	21	2.48	700	3.3
Steel	7900	4.2	1.5	210	12
Al	2700	0.17	0.13	70	25
Iron	7800	12.6	0.4	196	12

* This value is average in isotropic approximation.

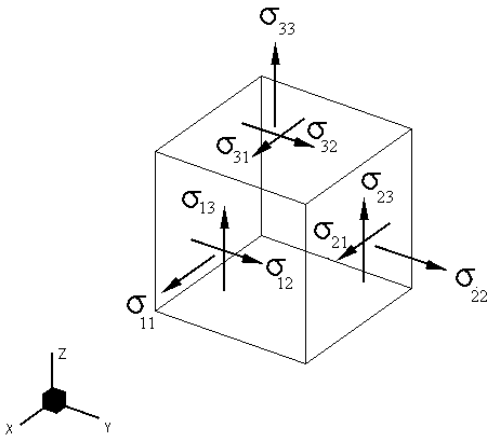

Fig 2. 5 Stress components of an infinitesimal single crystal silicon cube

Concerning the mechanical properties, we consider the stress at three faces of an infinitesimal cube instead of six (see Fig 2. 5). The forces across opposite faces are equal and opposite in the case of equilibrium [76].

$$\sigma_{ij} = \lim_{\delta A \to 0} \frac{\delta F_j}{\delta A_i} \qquad \text{i,j=1,2,3} \tag{2.16}$$

where δA_i is the area of the i^{th} face, and δF_j is the j^{th} force acting across the i^{th} surface. We can derive the second-rank stress as following:

$$\sigma_{ij} = \begin{bmatrix} \sigma_{11} & \sigma_{12} & \sigma_{13} \\ \sigma_{21} & \sigma_{22} & \sigma_{23} \\ \sigma_{31} & \sigma_{32} & \sigma_{33} \end{bmatrix} \tag{2.17}$$

The three σ_{ij} (with i=j) components are diagonal and they are called normal stress components. When $i \neq j$, the σ_{ij} are called the shear stress ones. By applying the condition of equilibrium, we can obtain $\sigma_{ij} = \sigma_{ji}$ with $i \neq j$. It also means that we can reduce from nice force components to six independent ones.

Strain is a dimensionless quantity. Strain expresses itself as a relative change in size and/or shape. This deformation is also described by a symmetric second-rank tensor:

$$\varepsilon_{ij} = \begin{bmatrix} \varepsilon_{11} & \varepsilon_{12} & \varepsilon_{13} \\ \varepsilon_{21} & \varepsilon_{22} & \varepsilon_{23} \\ \varepsilon_{31} & \varepsilon_{32} & \varepsilon_{33} \end{bmatrix} \tag{2.18}$$

Similar to the stress, we also derive $\varepsilon_{ij} = \varepsilon_{ji}$ for $i \neq j$, this symmetry means that there are only six independent components in the strain tensor.

In case of an elastic deformation, deformations of materials are reversible. The Hooke's law in these cases states that the stress is linearly proportional to the strain. This relation can be expressed in the tensor notation as:

$$\sigma_{ij} = C_{ijkl}\varepsilon_{kl} \quad \text{i, j, k, l} = 1, 2, 3 \tag{2.19}$$

where C_{ijkl} is a elastic stiffness tensor that represents the resistance of a material to the elastic deformation. Inversely, we can obtain:

$$\varepsilon_{ij} = S_{ijkl}\sigma_{kl} \tag{2.20}$$

where S_{ijkl} is an elastic compliance tensor of the material. It is a measure of the ease of deformation.

By utilizing the symmetric properties, we get $C_{ijkl} = C_{jikl} = C_{ijlk} = C_{jilk}$. Thus, we can reduce the size of C_{ijkl} from 81 to 36. Further more, we can use matrix notation instead of tensor notation. It means that we use only one index for σ_{ij} and ε_{ij}, and two indices for C_{ijkl} and S_{ijkl} (see Table 2. 2).

Table 2. 2. Index transformation scheme.

Tensor notation indices	11	22	33	12	21	13	31	23	32
Matrix notation indices	1	2	3	6		5		4	

We now can convert the relation between stress and strain into the matrix form as follows:

$$\sigma_m = C_{mn}\varepsilon_n \tag{2.21}$$

and

$$\varepsilon_m = S_{mn}\sigma_n \text{ (m, n = 1, 2, …, 6).} \tag{2.22}$$

In single crystal silicon where the coordinate system has three orientations: <100>, <010>, <001>, the number of independent compliances is reduced to three, and the matrix S_{mn} can be written as [64]:

$$S_{mn} = \begin{bmatrix} S_{11} & S_{12} & S_{12} & & & \\ S_{12} & S_{11} & S_{12} & & & \\ S_{12} & S_{12} & S_{11} & & & \\ & & & S_{44} & & \\ & & & & S_{44} & \\ & & & & & S_{44} \end{bmatrix} \tag{2.23}$$

2.2.2. Piezoresistive effect

Lord Kelvin discovered the piezoresistive effect in 1856 with copper and iron wires. After 100 years, the piezoresistive effect in semiconductors was found to be much larger than metals by C. S. Smith with germanium and silicon [61].

The phenomenon where resistance of crystal material varies when subjected to mechanical stress is called the piezoresistive effect. It is caused by the anisotropic characteristics of the energy resolution of the crystal space.

For simplicity, at first we consider a silicon cylindrical wire. In this case of one dimension, the equation for resistance is simply expressed as:

$$R \equiv \rho \frac{L}{S} \tag{2.24}$$

where L is the length of the wire, S is the cross-sectional area, and ρ is the resistivity of the wire material. After differentiating this equation, we obtain:

$$dR = \frac{\rho}{S} dL + \frac{L}{S} d\rho - \frac{\rho L}{S^2} dS \tag{2.25}$$

or

$$\frac{dR}{R} = \frac{dL}{L} + \frac{d\rho}{\rho} - \frac{dS}{S} \tag{2.26}$$

Another important quantity of the silicon wire under consideration is the *Poisson's ratio* which can be defined by ratio of the transverse strain to the longitudinal strain:

$$v = -\frac{\varepsilon_t}{\varepsilon_l} = -\left(\frac{dD}{D}\right)\left(\frac{dL}{L}\right)^{-1} \tag{2.27}$$

where ε_t is the transverse strain, ε_l is the longitudinal strain, and D is the diameter of the wire. Furthermore, we also have the relation between diameter change and cross-section area change:

$$\frac{dS}{S} = 2\frac{dD}{D} \tag{2.28}$$

where the cross-sectional area S can be calculated from the wire diameter D as:

$$S = \frac{\pi D^2}{4} \tag{2.29}$$

Combining equations (2.26) and (2.29) we obtain:

$$\frac{dR}{R} = \varepsilon(1+2v) + \frac{d\rho}{\rho} \tag{2.30}$$

Gauge factor of the piezoresistive sensor can be defined as:

$$K = \frac{dR/R}{\varepsilon_t} = (1+2v) + \frac{1}{\varepsilon_l}\frac{d\rho}{\rho} \tag{2.31}$$

In silicon, because its Poisson's ratio v is smaller than 0.403 so that the first term in the right hand side of the equation (2.31) is neglibly:

$$(1+2v) << \frac{1}{\varepsilon_l}\frac{d\rho}{\rho} \tag{2.32}$$

We can assume that the gauge factor to be due only to the stress-induced change of resistivity:

$$K \approx \frac{1}{\varepsilon_l}\frac{d\rho}{\rho} \tag{2.33}$$

Applying Hooke's law for stress and strain, equation (2.33) can be rewritten by:

$$\pi = \frac{1}{\sigma}\frac{\Delta\rho}{\rho} = -\frac{1}{\sigma}\frac{\Delta\theta}{\theta} \tag{2.34}$$

where π is the *piezoresistance coefficient*; σ is the stress and θ is conductivity. We can obtain the relationship between the stress-induced change of resistivity and the induced stress as:

$$\frac{\Delta\rho}{\rho} = \pi\sigma \tag{2.35}$$

The more general phenomenological theory of piezoresistance starts with Ohm's Law:

$$E_i = \rho_{ij} J_j \tag{2.36}$$

where E is the electrical field intensity, and J the current density,

In the three dimensional anisotropic crystal, ρ_{ij} are the components of the electrical resistivity tensor. Similar to above considerations, ρ_{ij} are reduced from nine to six and the tensor is found to be symmetric. If there is no stress, the diagonal components of ρ_{ij} are constant and the cross axis ones are zeros. It can be represented by:

$$\rho_{ij} = \rho_{0ij} + \Delta\rho_{ij} \tag{2.37}$$

where $\Delta\rho_{ij}$ are the stress induced resistivity change.

$$\frac{\Delta\rho_{ij}}{\rho_0} = \pi'_{ijkl}\sigma_{kl} \tag{2.38}$$

where π'_{ijkl} is the piezoresistance tensor in an arbitrary Cartesian coordinate system.

From the above considerations, the stress tensor and the resistivity change tensor are symmetric. Thus, the piezoresistance tensor is also symmetric. It means that we can also reduce its components from 81 to 36. The equation (2.38) thus can be expressed as:

$$\frac{1}{\rho_0}\begin{bmatrix}\Delta\rho_{11}\\ \Delta\rho_{22}\\ \Delta\rho_{33}\\ \Delta\rho_{23}\\ \Delta\rho_{13}\\ \Delta\rho_{12}\end{bmatrix} = \begin{bmatrix}\pi'_{1111} & \pi'_{1122} & \pi'_{1133} & \pi'_{1123} & \pi'_{1113} & \pi'_{1112}\\ \pi'_{2211} & \pi'_{2222} & \pi'_{2233} & \pi'_{2223} & \pi'_{2213} & \pi'_{2212}\\ \pi'_{3311} & \pi'_{3322} & \pi'_{3333} & \pi'_{3323} & \pi'_{3313} & \pi'_{3312}\\ \pi'_{2311} & \pi'_{2322} & \pi'_{2333} & \pi'_{2323} & \pi'_{2313} & \pi'_{2312}\\ \pi'_{1311} & \pi'_{1322} & \pi'_{1333} & \pi'_{1323} & \pi'_{1313} & \pi'_{1312}\\ \pi'_{1211} & \pi'_{1322} & \pi'_{1233} & \pi'_{1223} & \pi'_{1213} & \pi'_{1212}\end{bmatrix}\begin{bmatrix}\sigma_{11}\\ \sigma_{22}\\ \sigma_{33}\\ \sigma_{23}\\ \sigma_{13}\\ \sigma_{12}\end{bmatrix} \tag{2.39}$$

This equation can also be expressed in the matrix form by applying the following conventions:

$$11 \to 1 \quad 22 \to 2 \quad 33 \to 3 \quad 23 \to 4 \quad 13 \to 5 \quad 12 \to 6$$

In the matrix form, equation (2.38) turns out to be:

$$\frac{\Delta\rho_m}{\rho_0} = \pi'_{mn}\sigma_n \tag{2.40}$$

where $\Delta\rho_m$, π'_{mn} and σ_n are the resistivity change, piezoresistance coefficient, and stress in the matrix notation, respectively.

Expanding this equation, we can obtain:

$$\frac{1}{\rho_0}\begin{bmatrix}\Delta\rho_1\\ \Delta\rho_2\\ \Delta\rho_3\\ \Delta\rho_4\\ \Delta\rho_5\\ \Delta\rho_6\end{bmatrix}=\begin{bmatrix}\pi'_{11} & \pi'_{12} & \pi'_{13} & \pi'_{14} & \pi'_{15} & \pi'_{16}\\ \pi'_{21} & \pi'_{22} & \pi'_{23} & \pi'_{24} & \pi'_{25} & \pi'_{26}\\ \pi'_{31} & \pi'_{32} & \pi'_{33} & \pi'_{34} & \pi'_{35} & \pi'_{36}\\ \pi'_{41} & \pi'_{42} & \pi'_{43} & \pi'_{44} & \pi'_{45} & \pi'_{46}\\ \pi'_{51} & \pi'_{52} & \pi'_{53} & \pi'_{54} & \pi'_{55} & \pi'_{56}\\ \pi'_{61} & \pi'_{62} & \pi'_{63} & \pi'_{64} & \pi'_{65} & \pi'_{66}\end{bmatrix}\begin{bmatrix}\sigma_1\\ \sigma_2\\ \sigma_3\\ \sigma_4\\ \sigma_5\\ \sigma_6\end{bmatrix} \tag{2.41}$$

For the single silicon crystal, the number of independent coefficients can be more reduced by utilizing the crystal symmetry as:

$$\pi_{mn}=\begin{bmatrix}\pi_{11} & \pi_{12} & \pi_{12} & & & \\ \pi_{12} & \pi_{11} & \pi_{12} & & & \\ \pi_{12} & \pi_{12} & \pi_{11} & & & \\ & & & \pi_{44} & & \\ & & & & \pi_{44} & \\ & & & & & \pi_{44}\end{bmatrix} \tag{2.42}$$

It can be noted that there remain only three independent coefficients π_{11}, π_{12}, and π_{44}. These components for both p-type and n-type silicon have been measured experimentally by Smith (see Table 2. 3).

Table 2. 3 Three independent piezoresistive coefficients for single crystal silicon

	ρ (Ω.cm)	π_{11} (10^{-11} Pa^{-1})	π_{12} (10^{-11} Pa^{-1})	π_{44} (10^{-11} Pa^{-1})
p-type Si	7.8	6.6	-1.1	138
n-type Si	11.7	-102.2	53.4	-13.6

The more detail of calculation of piezoresistive coefficients can be found in [82]
From equation (2.40) we obtain [18]:

$$\frac{\Delta R}{R}\approx\frac{\rho_1^{'}-\rho_0}{\rho_0}=\pi'_{11}\sigma_1+\pi'_{12}\sigma_2+\pi'_{13}\sigma_3+\pi'_{14}\sigma_4+\pi'_{15}\sigma_5+\pi'_{16}\sigma_6 \tag{2.43}$$

When we place piezoresistors on the surface of a beam, the piezoresistors is stressed in only two dimensions at the surface. Thus, we can rewrite the equation (2.43) as following:

$$\frac{\Delta R}{R}=\pi'_{11}\sigma_1+\pi'_{12}\sigma_2+\pi'_{16}\sigma_6 \tag{2.44}$$

For convenience, the relative change of resistance can be expressed by using the longitudinal and transverse piezoresistance coefficients as follows:

$$\frac{\Delta R}{R} = \pi_l \sigma_l + \pi_t \sigma_t + \pi_s \sigma_s \tag{2.45}$$

Based on the piezoresistive effect, this thesis has focused to design, fabricate and calibrate a specific 3-DOF piezoresistive accelerometer with high performances. A novel design and optimization methodology has also been proposed in order to apply for new structures whose working principle is based on this effect.

2.2.3 Physical properties of Piezoresistive Effect

In this section, some importance characteristics of piezoresistive effect must consider to not only understand its physical aspect but also optimize accelerometers' performance in the chapter 5.

2.2.3.1 Relationship between resistance of piezoresistor and impurity concentration

The sensor's performance depends not only on the structure and the positions of piezoresistors, but also on the length, the cross-sectional area, doping concentration of piezoresistor.

For diffusion technique, thermal diffusion is used frequently. We are able to control the characteristic of piezoresistance desirably. The type of conduction of the regions where Boron ion was diffused in is converted from n-type into p-type. Those p-type regions are electrically separated from the other n-type regions. The value of resistance R is expressed by:

$$R \equiv \rho \frac{l}{wt} \equiv \rho_s \frac{l}{w} \tag{2.46}$$

where ρ is the resistivity; ρ_s is the sheet resistivity; l, w, and t are the length, width and thickness of the piezoresistor, respectively.

The resistivity ρ is dependent on the amount of boron ion diffused.

$$\rho = \frac{1}{\sigma} = \frac{1}{q(\mu_n n + \mu_p p)} \tag{2.47}$$

where n and p are the concentration of electrons and holes under non-equilibrium conditions, respectively; q is charge carrier and μ_n and μ_p are the mobility of electrons and holes in bulk silicon.

The minority carrier mobility also depends on the total impurity density, using the curve which corresponds to the minority carrier type. The curves are calculated from the empiric expression:

$$\mu = \mu_{\min} + \frac{\mu_{\max} - \mu_{\min}}{1 + (\frac{N}{N_r})^{\alpha}} \tag{2.48}$$

where μ_{min}, μ_{max}, α and N_r are fit parameters. These parameters for Arsenic, Phosphorous and Boron doped silicon are provided in the Table 2. 4 [3].

Table 2. 4 Fit parameters for calculation of the mobility

	Arsenic	Phosphorous	Boron
$\mu(cm^2/Vs)$	52.2	68.5	44.9
$\mu(cm^2/Vs)$	1417	1414	470.5
Nr (cm^{-3})	$9.68\ 10^{16}$	$9.20\ 10^{16}$	$2.23\ 10^{17}$
α	0.68	0.711	0.719

The dependences of the mobility of the carriers and the resistivity on the doping density for n-type and p-type silicon are shown in Fig 2.6 and Fig 2.7, respectively [3].

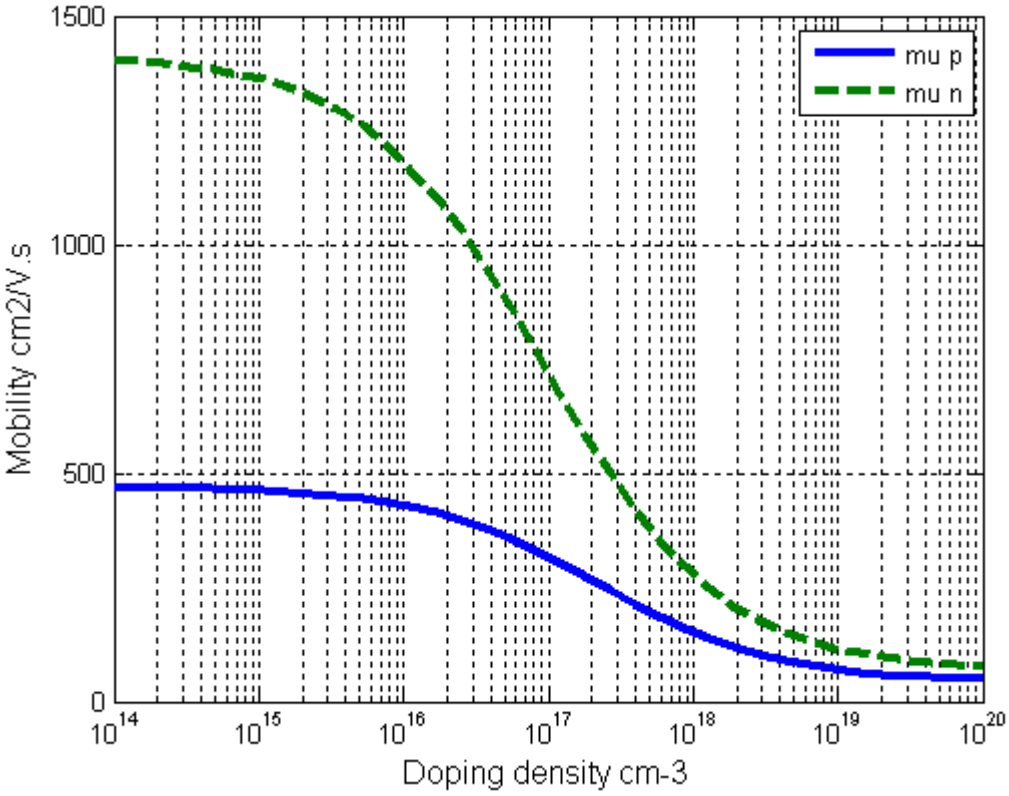

Fig 2.6 Electron and hole mobility versus doping density for n-type (dotted curve) and p-type (solid curve) silicon

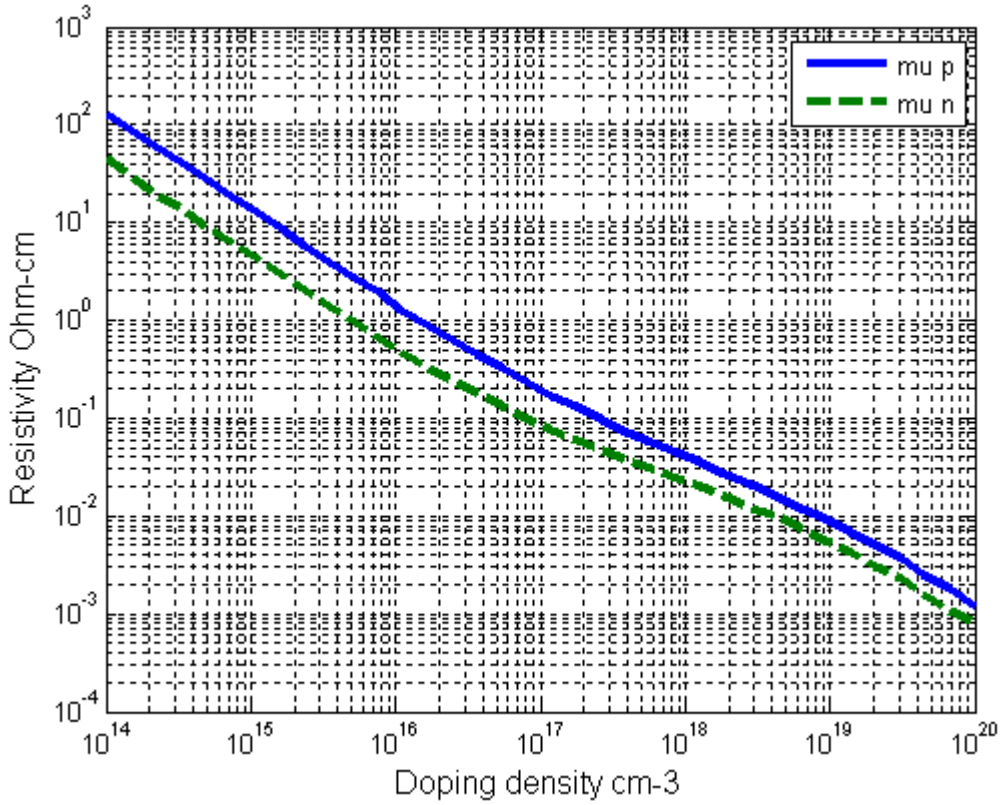

Fig 2.7 Resistivity of n-type (dotted curve) and p-type (solid curve) silicon versus doping density

2.2.3.2 The dependence of the piezoresistive (PR) coefficient on the impurity concentration at a given temperature T

The performance of the silicon-diffused piezoresistors is highly affected by temperature fluctuations primarily due to the change in the piezoresistive coefficient with the temperature. Temperature affects the piezoresistive coefficient though a change in the mobility and carrier concentration *N* in the respective bands. The dependence of the piezoresistive (PR) coefficient on the impurity concentration at a given temperature *T* can be obtained by multiplying the PR factor P(N,T) by the PR coefficient at room temperature (*To*) as follows:

$$\pi(T) = \pi(T_0)P(N,T) \tag{2.49}$$

where

$$P(N,T) = \frac{300}{T}\frac{F'_{s+.5}(E_F / k_B T)}{F_{s+.5}(E_F / k_B T)} \tag{2.50}$$

The Fermi integral is the function of the temperature and the Fermi energy (Fig 2. 8). The Fermi energy is determined from N by using the following relation:

$$N = v\frac{\sqrt{2}}{\pi^2}\left(\frac{m_d^* k_B T}{h}\right)^{3/2} F_{.5}(E_F / k_B T) \tag{2.51}$$

where m_d^* is the density of state effective mass and *v* is the number of valleys.

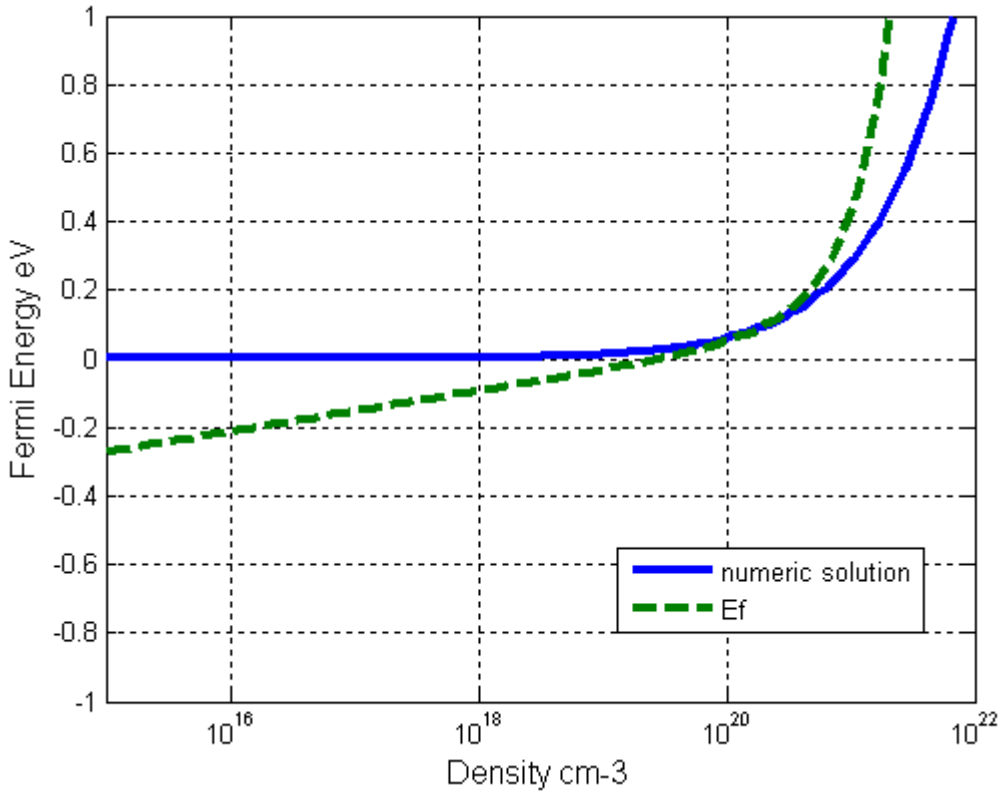

Fig 2. 8. Carrier density versus the Fermi energy

The graph of P(N,T) is shown in Fig 2.9. Temperature strongly determines the value of factor. The higher it, he smaller is the effect. Also larger concentration decreases the value of factor P(N,T) . Both of these occurrences are caused by the increased electron concentration.

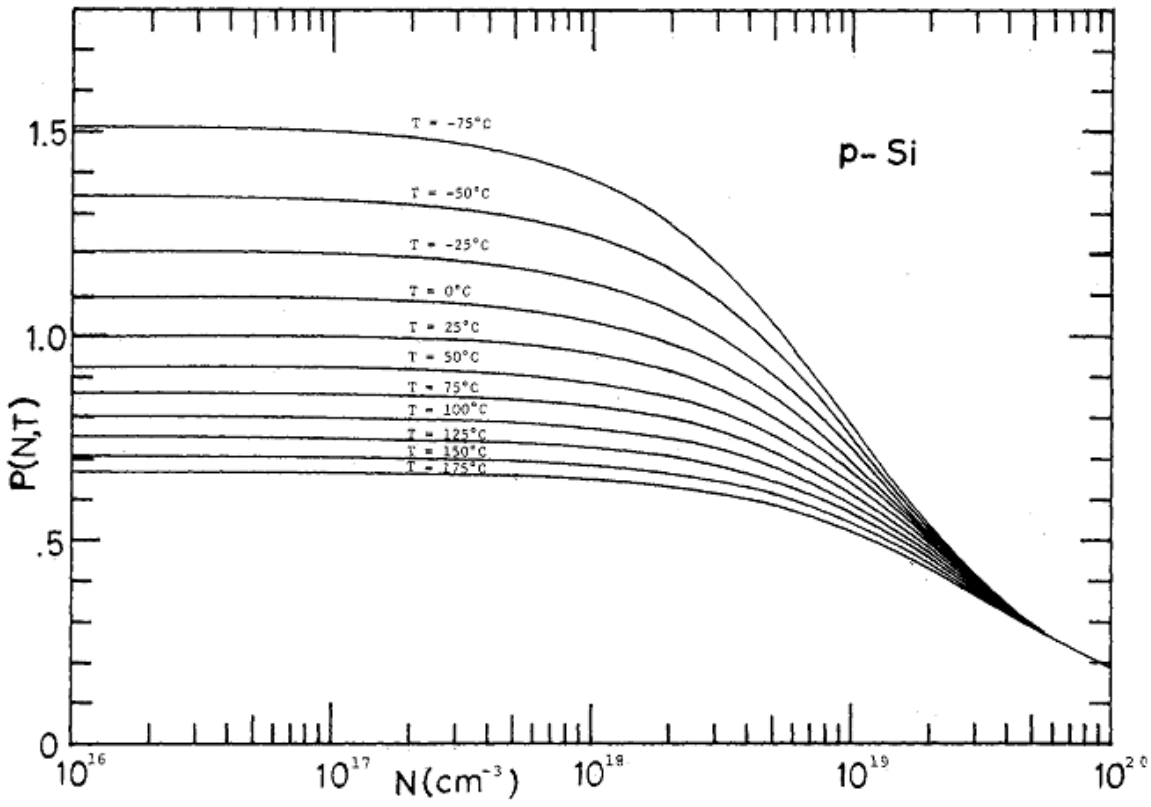

Fig 2.9 Piezoresistance factor P(N, T) as a function of impurity concentration and temperature for p-Si [38].

The information in Fig 2.9 is useless to apply in the optimum process that would be mentioned in latter chapter. Thus, the dependent of PR coefficient impurity concentration at different temperatures was built by a MATLAB program (see Abbreviation). The experimental measurement of piezoresistive coefficients can also be found in [35][36]. To extend the range of the problem, the piezoresistance effect nonlinearity in p-Si was mentioned in [39][14].

We note that in a piezoresistor, the doping density is varies through the thickness of its layer. Thus, the doping density value we mentioned in this chapter is the average one (see Abbreviation) with assumed that the piezoresistor is formed on Gaussian profile [19], [49].

2.2.3.3 The dependence of piezoresistor's temperature on power consumption

It is absolutely necessary to estimate the temperature rise in a single piezoresistor after a certain operating time due to Joule's heating alone even if the ambient temperature is constant. Such analysis of internal temperature rise will be beneficial

not only to design the temperature compensation circuit but also to choose a suitable package for the chip, which can act as a heat sink to protect the circuitry from excessive temperature rise.

The effects of electrical heating in a silicon MEMS piezoresistive acceleration sensor have been analyzed analytically and verified experimentally. The temperature rise due to internal heating has been computed for different dimensions of the sensor as well as for different operating times. The relation between the steady state of temperature rise v and power consumption P can be expressed as [64]:

$$v = \frac{R_T P}{1 + \alpha_R R_T P} \approx R_T P \tag{2.52}$$

where α_R and R_T are the temperature coefficient of resistance (TCR) and is the thermal resistance, respectively.

This relationship is supposed to be approximately linear as illustrated schematically in Fig 2. 10. The more details of this heating effect can be found in the Abbreviation.

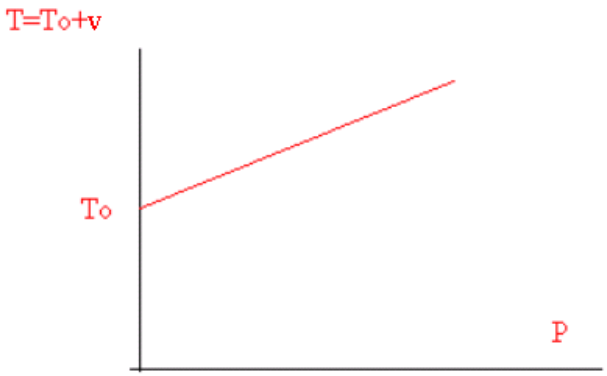

Fig 2. 10 Relation between power consumption and temperature of the piezoresistor

2.3 Overview of MNA and FEM Softwares

2.3.1 Overview of a MNA Software: SUGAR

Recently, the MEMS community has achieved such great results in fabrication techniques, but simulation capabilities in MEMS are still quite limited. Many circuit designers often use circuit simulation tools like SPICE, but MEMS designers have to calculate by spare programs.

We all know that simulation tool plays a very important role in the design of complicated MEMS. Moreover, the demands for optimization and evolutionary synthesis require a huge of computations.

SUGAR is a tool that inherits SPICE's philosophy. A MEMS designer can easily design a device in a compact netlist format. This structure can be simulated quickly to predict the device's behavior. A designer can debug a design or try out new ideas by using SUGAR. Further more, the designer can check the structure for more details by splitting the structure in smaller parts.

SUGAR is embedded in MATLAB to make it easier to install and develop. SUGAR builds structure components by using parameterized subnets. These components can be various kinds of physical functions such as beams, electrostatic gaps, etc. The designer has ability to build his own definable model functions that expand widely SUGAR's modeling capabilities. Thus, large and complex systems can be modeled easily. The user can control and modify input parameters (material property and geometry) such as Young's modulus, beam widths, number of comb arrays, etc. It is hardly to do so when we use other CAD software.

Nodal analysis decomposes the structure into N-terminal devices. Each device is modeled by ordinary differential equations (ODEs). The coefficients of these ODEs are parameterized by device geometry, and material properties that can be obtained from measurements or standard processes. Devices are linked together at their nodes to build a system of nonlinear ODEs. It can be solved using nodal analysis.

To simulate MEMS devices, SUGAR uses three basic elements: beam, gap, and anchors. With each element, a specific ODE model is built. The system equations are formulated based on connectivity information provided in the input file, and solved using nodal analysis.

In the following sections, some details of applying nodal analysis in MEMS design are described.

Nodal Analysis Approach

SUGAR espouses the philosophy of the venerable IC simulation tool SPICE. It provides quick and accurate results at the system level [33], [34], although it does employ some approximations to make the device "fit" within its simulation mechanics.

SUGAR uses the law of static equilibrium applied to each node [84]. Following this law, the sum of the forces and moments on the nodes are equal to zero. This is similar to Kirchhoff's current law in circuit analysis in which forces can be seen as currents and displacements at each node can be seen as voltages. The forces and displacements on each node depend on structural models.

To demonstrate the method of SUGAR, the structure shown in Fig 2. 11 is chosen. It contains one beam element, three anchor elements, and an electrostatic gap element. Because anchor elements are fixed to the substrate (i.e. no degree of freedom), we only need to care about beams and gaps in the analysis.

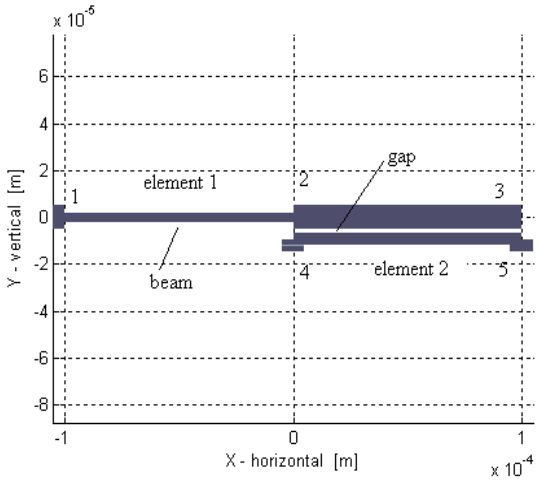

Fig 2. 11 A simple MEMS structure

In the first step, we have to formulate the individual element. For the beam element that connects from node 1 to node 2 we have:

$$f_n^1 = f_n^1(q_1, q_2) \qquad \text{n=1, 2} \qquad (2.53)$$

And for the gap element (nodes 2, 3, 4, 5) we have

$$f_n^2 = f_n^2(q_2, q_3, q_4, q_5) \qquad \text{n=2, 3, 4, 5} \qquad (2.54)$$

where f_n represents the forces $\{F_{x,n}, F_{y,n}, M_n\}$ applied at node n, and q_n represents the node displacements $\{x_n, y_n, \theta_n\}$. The super- and subscripts on f are the element number and node number, respectively. Each node has three degrees of freedom in the 2-D case: x, y direction and rotation. Note that the f's are the internal nodal forces.

Due to the law of static equilibrium, the sum of such internal forces at each node is equal to the external load *P*. In this case, P is the electrostatic forces generated at nodes *2, 3, 4,* and *5*. The system equations for each node are:

$$\begin{aligned} P_1 &= f_1^1(q_1, q_2) \\ P_2 &= f_2^1(q_1, q_2) + f_2^2(q_2, q_3, q_4, q_5) \\ P_3 &= f_3^2(q_2, q_3, q_4, q_5) \\ P_4 &= f_4^2(q_2, q_3, q_4, q_5) \\ P_5 &= f_5^2(q_2, q_3, q_4, q_5) \end{aligned} \tag{2.55}$$

Because the displacements for anchor nodes *1, 4*, and *5* are zero, they are removed. The final system equations become:

$$\begin{aligned} P_2 &= f_2^1 + f_2^2 = f_2^1(q_2) + f_2^2(q_2, q_3) \\ P_3 &= f_3^2(q_2, q_3) \end{aligned} \tag{2.56}$$

By using this method, we can formulate the system's equations of motion. We can found that there are different model levels in SUGAR, which allow the user to trade off accuracy and speed.

2.3.2 Overview of a FEM Software: ANSYS

Most of MEMS devices have been simulated by using FEM softwares [47]. Finite element methods (FEM) can be defined as techniques used for finding approximate solutions of partial differential equations (PDE) or integral equations. The method is relied on reducing the differential equations to linear equations or a system consisted of ordinary differential equations.

There are two solutions for the FEM: the first one is the direct variational method such as Rayleigh–Ritz method and the second one is the method of weighted residuals such as Galerkin method. This section will explain how to obtain the basic equations for the FEM utilized the Galerkin method.

Let us consider a simple boundary value problem:

$$\begin{aligned} &L[u(x)] = f(x) \quad (a \le x \le b) \\ &Boundary\ \ condition:\ \ u(a) = u_a \quad u(b) = u_b \end{aligned} \tag{2.57}$$

where L is a linear differential operator, f(x) a function of x, u_a and u_b are one-dimensional boundaries of the region D.

At first, we divide the region a≤x ≤b into n sub-regions (see Fig 2. 12). These sub-regions are *elements* in the FEM.

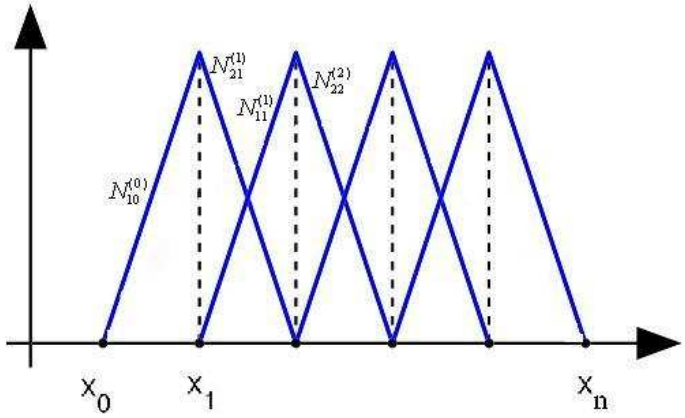

Fig 2. 12 Division of the domain and the interpolation functions.

We can express an approximate solution of *u*:

$$\hat{u}(x) = \sum_{i=1}^{n+1} u_i N_i(x) \tag{2.58}$$

where $\hat{u}$ is an approximate solution of u, u_i is the value of u in element "e" at a boundary point "i" between two one-dimensional elements, and $N_i(x)$ are piecewise linear functions which creates a straight line in each sub-region. The functions are also called interpolation or shape functions of the nodal point "i:"

$$\begin{aligned} N_{1e}^{(e)} &= \frac{x_{e+1} - x}{x_{e+1} - x_e} = \frac{x_{2e} - x}{x_{2e} - x_{1e}} = \frac{h^{(e)} - \xi}{h^{(e)}} \\ N_{2e}^{(e)} &= \frac{x - x_e}{x_{e+1} - x_e} = \frac{x - x_{1e}}{x_{2e} - x_{1e}} = \frac{\xi}{h^{(e)}} \end{aligned} \tag{2.59}$$

where:

e (e =1, 2, . . . , n) is the element number

x_i is the global coordinate of the nodal point i (i=1, . . . , e −1, e, . . . n, n+1)

1e and 2e denote the number of two nodal points of the e^{th} element.

$N_{ie}^{(e)}$ is the value of the interpolation function at the nodal point i_e (i_e =1_e, 2_e) which belongs to the e^{th} element

ξ is the local coordinate of an arbitrary point in the e^{th} element, ξ = x−x_e = x−x_{1e} (0≤ξ ≤$h^{(e)}$)

$h^{(e)}$ is the length of the e^{th} element which can be expressed as $h^{(e)} = x_{e+1} - x_e = x_{2e} - x_{1e}$.

The quadric interpolation is better than the linear one. To get the better solutions, the interpolation function is often the quadric one.

In the Galerkin method-based FEM, the weighting functions $w_i(x)$ is the interpolation functions $N_i(x)$:.

$$w_i(x) = N_i(x) \qquad (i = 1,2,..,n+1) \tag{2.60}$$

Thus, the approximation is good if the integral of R over the region of interest weighted by N_i functions is zero:

$$\int_D N_i R.dv = 0 \tag{2.61}$$

where D is the region considered and R is the error that can be expressed by:

$$R = L[\hat{u}(x)] - f(x) \tag{2.62}$$

In the FEM, simultaneous algebraic equations for u(x) at u_i and $(du/dx)_i$ are derived by integrating Equation (3.11) by parts and applying boundary conditions. These equations can be solved by computers to calculate the unknown variables u_i and $(du/dx)_i$ at all the nodal points.

ANSYS is a FEM software for numerically solving a wide variety of mechanical problems such as structural, heat transfer, fluid, acoustic and electro-magnetic analyses, etc. Recently, ANSYS is often utilized to analyze many different structures of MEMS devices [10].

A finite element solution may be simply divided into the three following steps:

1) Preprocessing: we can define the problem as:
   - Define key-points/lines/areas/volumes
   - Define element type and material/geometric properties
   - Mesh lines/areas/volumes
   - The more detail will depend on the dimensionality of the analysis (i.e. 1D, 2D, or 3D).
2) Solution: applying loads, constraints and solving.
3) Post-processing: processing and viewing of the results such as:
   - Lists of nodal displacements
   - Element forces and moments
   - Deflection plots
   - Stress contour diagrams

2.4 Summary

This chapter presented the basic working principle of the open-loop accelerometer that has been utilized in the next chapters. After that, the mechanical and piezoresistive properties of silicon were discussed. These contents are necessary to optimize the sensor's performance in the chapter 5. The overview of two typical methodologies (FEM and MNA) concerned in the last section of this chapter is very important premise to invent a novel design process that would mentioned in the next chapter: combining FEM and MNA methods in structural design.

CHAPTER 3

DESIGN PRINCIPLES AND ILLUSTRATING APPLICATION: A 3-DOF ACCELEROMETER

3.1 Introductions

This chapter presents the whole of the design and simulation procedures of a 3-DOF accelerometer. At first, the novel synthesis design of a three-degree of freedom silicon piezoresistive accelerometer is presented in order to achieve the structure's parameters that met desired performances. It has been performed based on combination of a FEM software (ANSYS) and a MNA one (SUGAR). The optimal configuration was reached by exploiting the advantages of both types of simulations.

In the next step of the design procedure, the structural analysis plays the very important role in our design process when it can provide the stress distribution in the beam system. Based on this distribution, piezoresistors are positioned to eliminate cross-axis sensitivities and to maximize the sensing sensitivity to the three acceleration components.

This chapter also presents comprehensive analyses for thermal – mechanical – piezoresistive fields in order to evaluate the sensor characteristics. The results are very helpful to further improve and optimize the performance of the device.

Finally, in order to bring this sensor to fabrication process, the photo masks will be described as the last step of the design process.

3.2 Working Principle for a 3-DOF Accelerometers

The three-degrees-of-freedom accelerometer always requires small cross-axial acceleration, high and linear sensitivity. We proposed a flexure configuration that is shown in Fig. 3. 1 in order to meet these critical characteristics. Fig. 3. 2 shows the cross-sectional view of typical motion along the X, Y and Z axes.

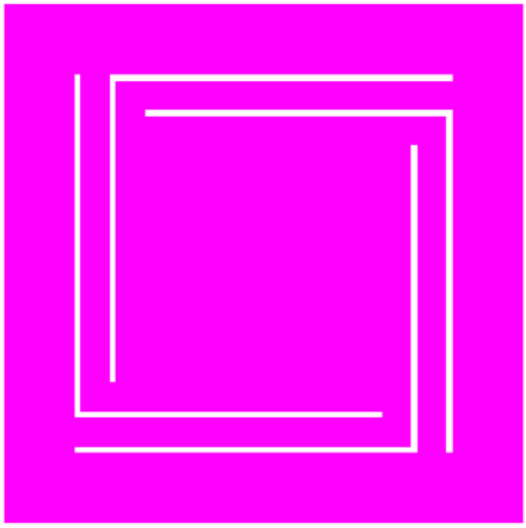

Fig. 3. 1 Plane view of the 3-DOF Piezoresistive accelerometer

The operation of the device is based on inertia. An external acceleration results in a force being exerted on the mass. This force results in deflection of the proof mass. The acceleration component (Az) causes the mass to move vertically up and down. The second type of motion is caused by the X or Y component of transversal accelerations. The deflection of the proof mass causes stress variations on the four beam surfaces. This phenomenon in turn provokes resistance variations in the piezoresistors embedded on the surface of the beam structure.

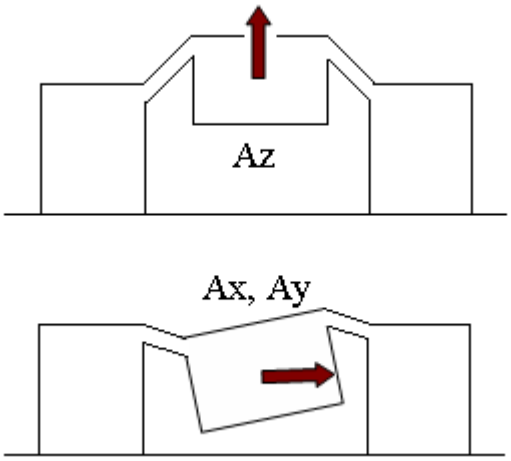

Fig. 3. 2 Cross-sectional view of motion along X, Y and Z axes

Such variations are converted into electrical signals by using three Wheatstone bridge circuits. They are simple and it is possible to integrate electronic circuitry directly on the sensor chip for signal amplification and temperature compensation. These Wheatstone bridge circuits were built by interconnecting twelve p-type piezoresistors. These p-type piezoresistors were chosen to diffuse on the surface of these four beams because they can provide the maximal resistance variations. These piezoresistors were aligned with the crystal directions <110> and <1$\bar{1}$0> of n-type silicon (100). These piezoresistors were designed to be identical and fabricated by diffusion method.

The piezoresistance effect is caused by the anisotropic characteristics of the energy resolution in crystal space. In silicon material, there are only three independent coefficients π_{11}, π_{12} and π_{44}. The longitudinal piezoresistance coefficient π_l is defined in the case the stress parallels with the direction of the electric filed and current density. Similarly, the transverse piezoresistance coefficient π_t is defined in the case the stress is perpendicular with the direction of the electric filed and current density. In directions <110> and <1$\bar{1}$0> of n-type silicon (100), we can show these two coefficients thanks to three independent coefficients π_{11}, π_{12} and π_{44} as the following equation:

$$\begin{aligned} \pi_l &= \frac{1}{2}\left(\pi_{11} + \pi_{12} + \pi_{44}\right) \\ \pi_t &= \frac{1}{2}\left(\pi_{11} + \pi_{12} - \pi_{44}\right) \end{aligned} \tag{3.1}$$

We can calculate the relative change of resistance due to the normal stress as the following equation:

$$\frac{\Delta R}{R} = \pi_l \sigma_l + \pi_t \sigma_t \tag{3.2}$$

3.3 A Systematic and Efficient Approach of Designing Accelerometers

In this section, the piezoresistive accelerometer mentioned in section 3.1 is chosen to be subject of the design synthesis.

The design flow must correctly address design performance specifications prior to fabrication. However, CAD tools are still scarce and poorly integrated when it comes to MEMS design. This often results in an excessively lengthy design cycles

[9][50]. One of the goals of this thesis is to propose a fast design flow in order to reach multiple specified performance targets in a reasonable time frame. This is achieved by leveraging the best features of two radically different simulation tools: Berkeley SUGAR, which is an open-source academic effort, and ANSYS, which is a commercial product.

In this method, SUGAR was utilized to quickly sketch out the structure of the accelerometer. It is comprised of a center mass connected to four flexure beams comprised of a series of beams and anchors. Design goals for our configuration consist of desired resonant frequencies at the 1^{st}, 2^{nd} and 3^{rd} mode. After iterating in SUGAR to converge towards these goals, an acceptable preliminary design was brought to ANSYS for local optimization at the device level. Then, a stress analysis was performed in order to determine the positions of the doped piezoresistors on the four flexure beams. The overall design and simulation effort using this technique is roughly 20 times shorter than with the built-in optimization function available within ANSYS.

Our desired structure comprises a square-shaped mass, anchors, and flexure beams as shown in Fig. 3. 3. The mass is a rigid plate, i.e. it is sufficiently thick to be treated as a rigid element. In this design, the dimension of the sensor die is fixed to $1.5\times1.5\times0.5$ mm^3 and the outer frame is fixed to 200 μm. Thus, the mass and the beams are evolved to achieve the design requirements. The connectivity of the center mass is represented by the four nodes shown in Fig. 3. 4. Positions of these connecting nodes are determined by parameters of the beams.

The MEMS designer can easily modify various process parameters such as Young's modulus, Poisson's ratio, the residual stress, and the coefficient of thermal expansion in the process file.

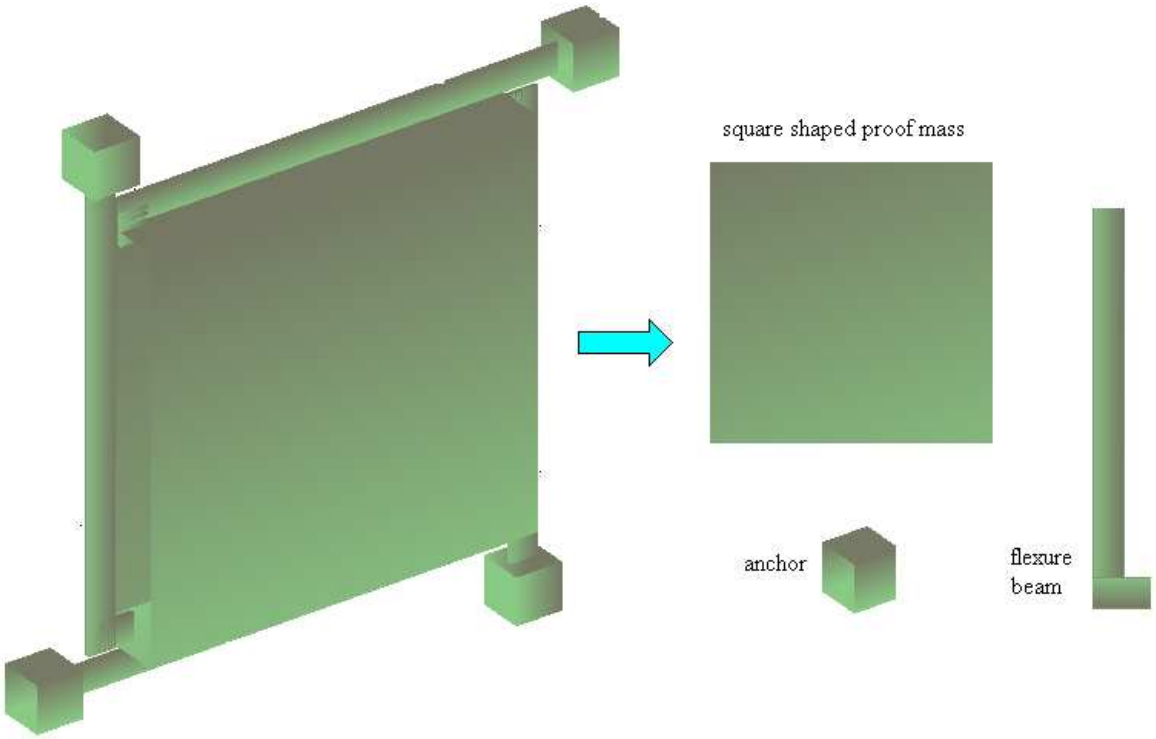

Fig. 3. 3 Separating the elements from the flexure structure

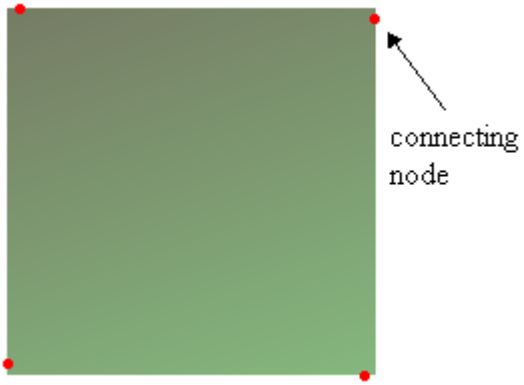

Fig. 3. 4 Connectivity of the proof mass

The modeling techniques and efficient analysis in SUGAR allow the creation of designs and the production of simulation results much faster than with conventional CAD software. Furthermore, its graphical user interface (GUI) provides convenient interactive visualization capabilities (see Fig. 3. 5).

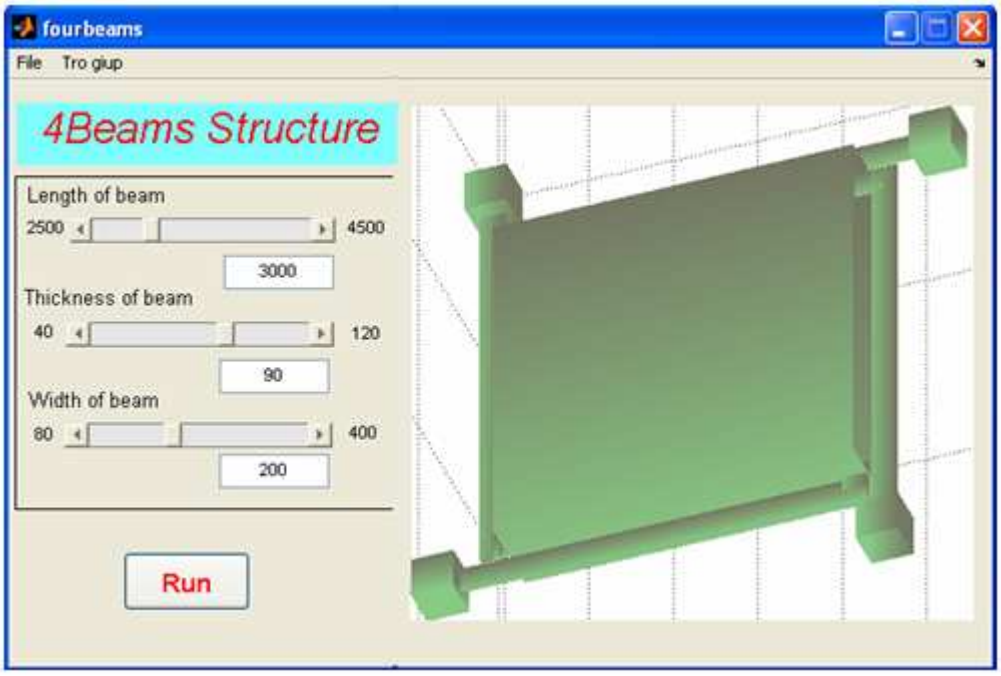

Fig. 3. 5 GUI of the four-beam structure

Two specification constraints are imposed on the structure to be designed: (1) the natural frequency in the Z direction must be about 1500 Hz and (2) the natural frequency in the X (or Y) direction must be about 100 kHz. Furthermore, a set of parameter constraints is listed in Table 3. 1. Note that the actions of various parameters are interdependent.

Table 3. 1 Parameter Constraints for Accelerometer

Proof mass			
Parameter		*Value*	
Max thickness		400 μm	
Min thickness		150 μm	
Max area		500 μm^2	
Min area		200 μm^2	
Flexure beam			
Longer spring		Shorter spring	
Parameter	*Value*	*Parameter*	*Value*
Max thickness	100 μm	Max thickness	100 μm

Min thickness	10 μm	Min thickness	10 μm
Max width	200 μm	Max width	200 μm
Min width	60 μm	Min width	60 μm
Max length	480 μm	Max length	200 μm
Min length	240 μm	Min length	10 μm

A MEMS device can have a surface structure or a bulk structure. Our case study accelerometer adopts the bulk-type structure. Fig. 3. 6 shows the 90% automated synthesis flow that was used to evolve the final design. In the first three steps, an automatic refinement procedure is employed where the step size of a given parameter is varied adaptively. For example, the step size of the beam's width (λ) is initially set at 50 μm. When the resonant frequency overshoots across the desired frequency, we move back to the previous step point and scale back the step size in order to reach to optimum point (see Fig. 3.9).

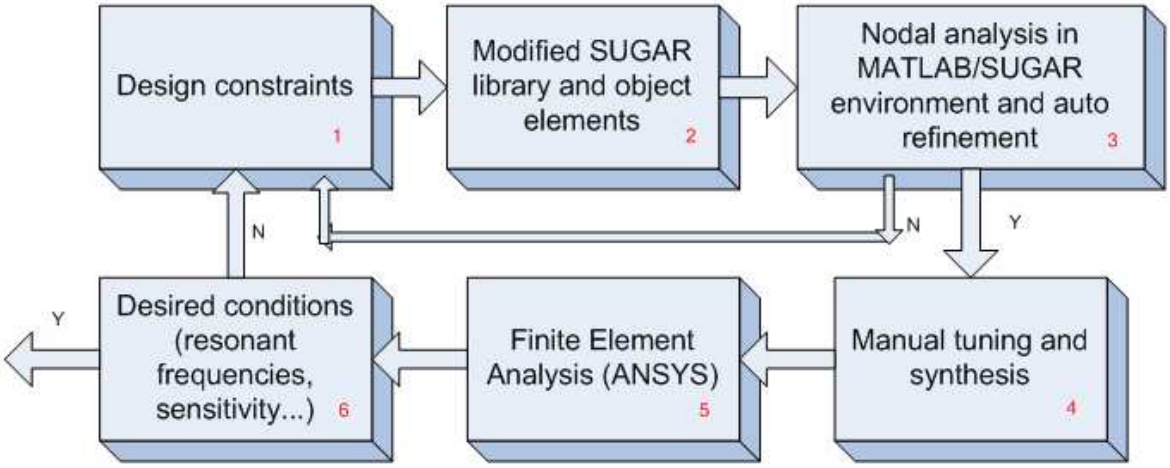

Fig. 3. 6 Flow chart of the optimizing design

Fig. 3. 7 shows the resonant frequency variation in terms of the beam width, when we fixed the beam thickness to a minimal value and the proof mass thickness to a maximal value in order to get the maximum sensitivity. These extreme values are based on process constraints, i.e. design rules. The beam width was iteratively refined in order to make the first resonant frequency reach the desired value. We

can see that the resonant frequency decreases rapidly when the beam width decreases. It takes 8 iterations to reach the optimum value and the process overshoots twice.

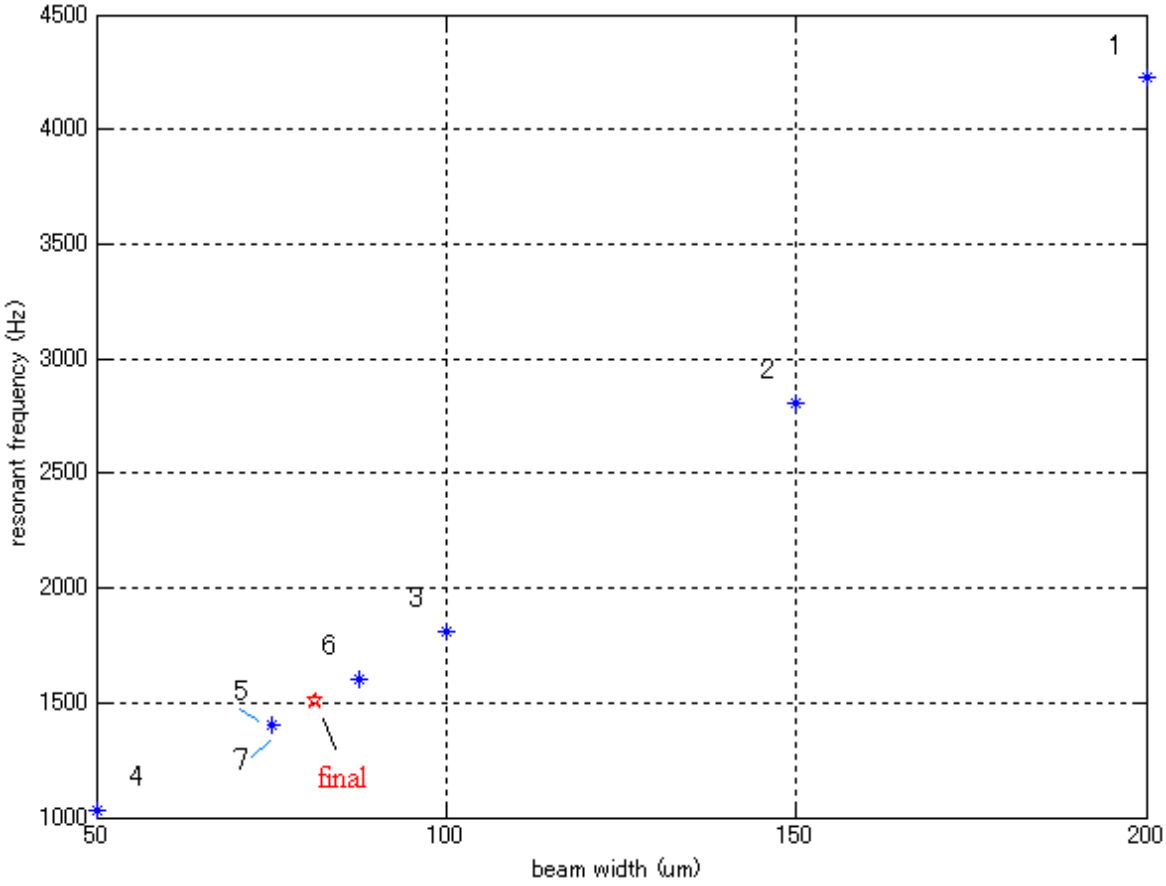

Fig. 3. 7 Determining the optimum beam width when the thicknesses of the beam and mass are fixed to 10 μm and 400 μm, respectively.

Fig. 3. 8 shows again that the design process converges in eight steps. Theoretically, we can get the exact desired resonant frequency, but this is not very meaningful because of the 10% gap between SUGAR and reality [66].

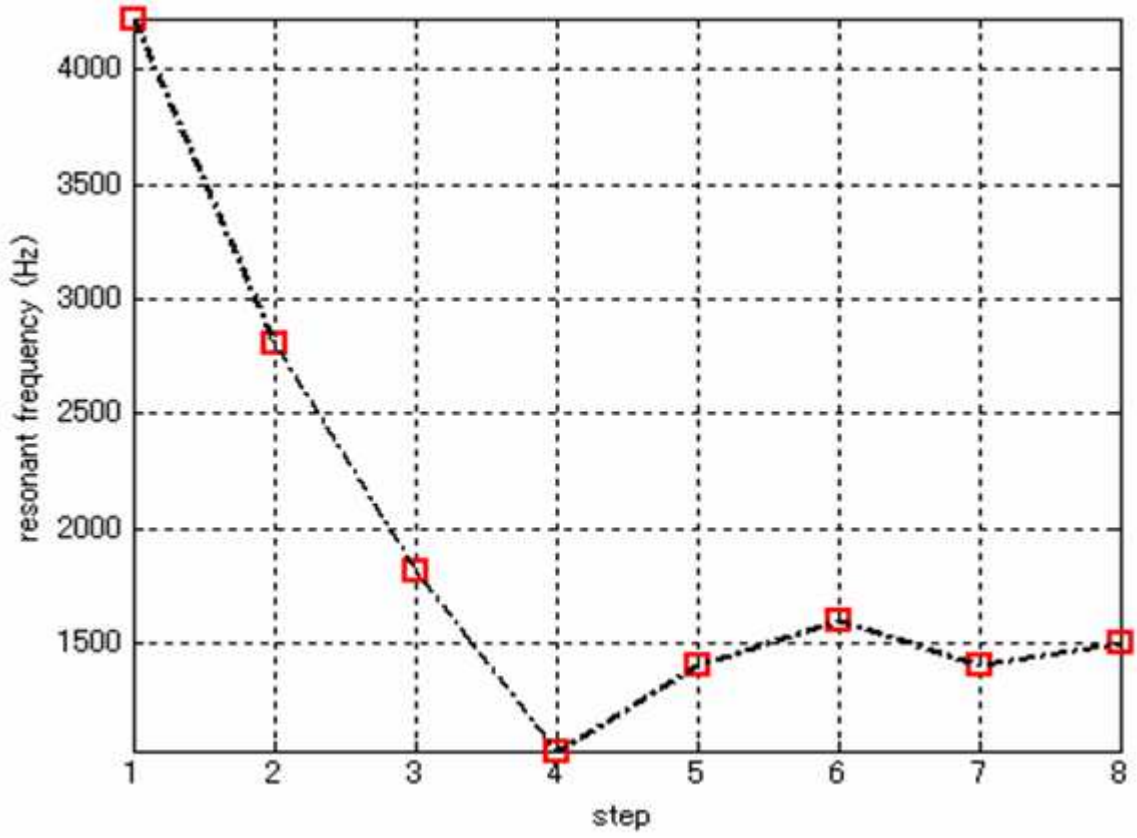

Fig. 3. 8 The convergence of the design process in the 3rd block

The initial value of the step size in this algorithm should be chosen wisely. Fig. 3. depicts a case with no overshoot where the final result is reached in just 5 steps. This was accomplished by simply reducing the initial step size with respect to Fig. 3. 9.

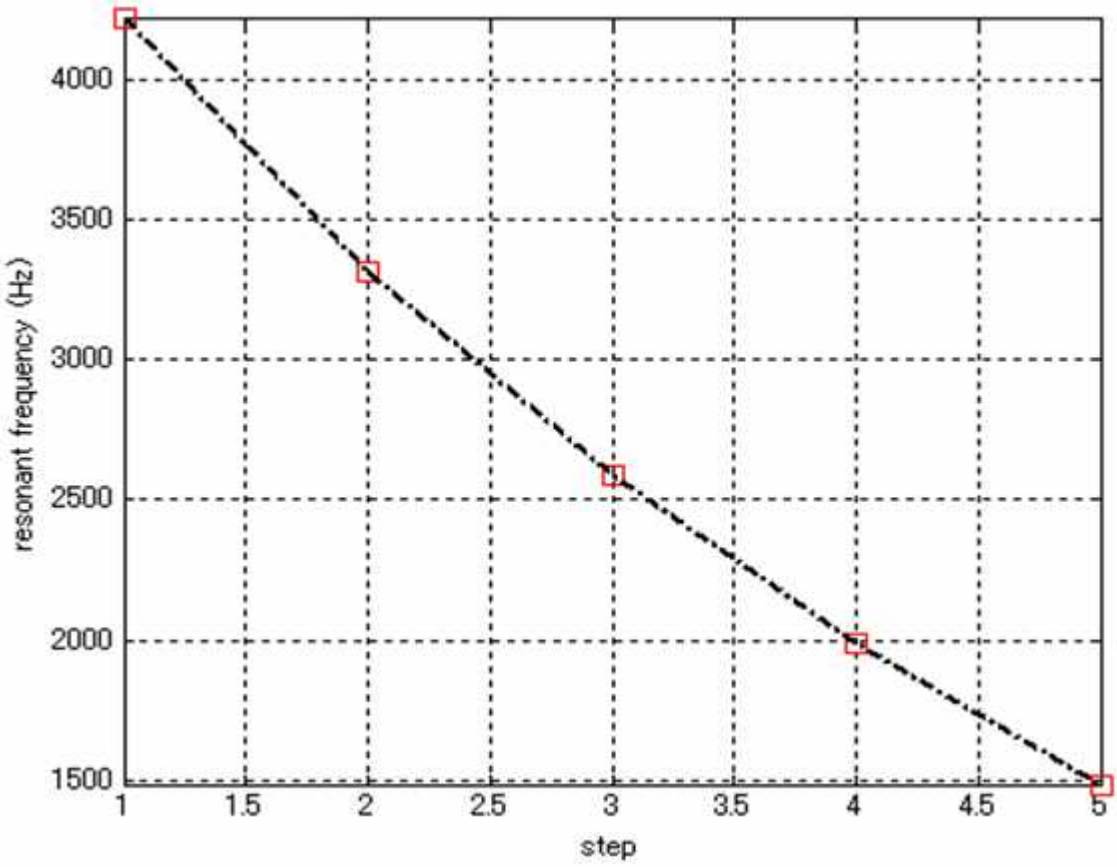

Fig. 3. 9 Convergence of design parameters (resonant frequency) showing how sensitive the time expenditure is to the initial value of the step size

The best designs resulting from the 4th block (Table 3. 2) are brought to the Finite Element Method (FEM) process. Finite Element Analysis (FEA) based tools – although complex – yield more complete and precise numerical results and especially are more flexible in choosing the device geometry.

Table 3. 2 Sensor Parameters after Manual Tuning and Synthesis Block

	Size
Mass	845×845×400 μm^3
Beam	975×80×10 μm^3
Die size	1.5×1.5×0.5 mm^3
Outer frame width	200 μm

SUGAR is a simplified simulation method and is therefore prone to imprecision of various kinds. The main source of error in our case stem from beam overlapping. In exchange for much faster simulation speed, SUGAR does not include the actual conditions at the end of the beam. This problem can be avoided in ANSYS by joining all the beam polygons into a single polygon through a union operation, such that overlapping areas are subsumed.

Above all other considerations, the most important aspect of FEA in our design process is the analysis of the stress distribution in the flexure beams [45]. Based on this distribution, piezoresistors are positioned to eliminate cross-axis sensitivities and to maximize the sensitivity to the three acceleration components. The details of the design are presented in the next section.

3.4 Structure Analysis and the Design of the Piezoresistive Sensor

3.4.1 Structural analysis of the sensor and piezoresistor arrangement on beams

The finite element model of the sensing chip was analyzed by using ANSYS software. In order to perform stress analysis, an appropriate meshing is need. Fig. 3. 10 shows the mesh generation for analysis. Based on the stress, piezoresistors are placed to eliminate the cross-axis sensitivities and to maximize the sensitivities to three components of acceleration.

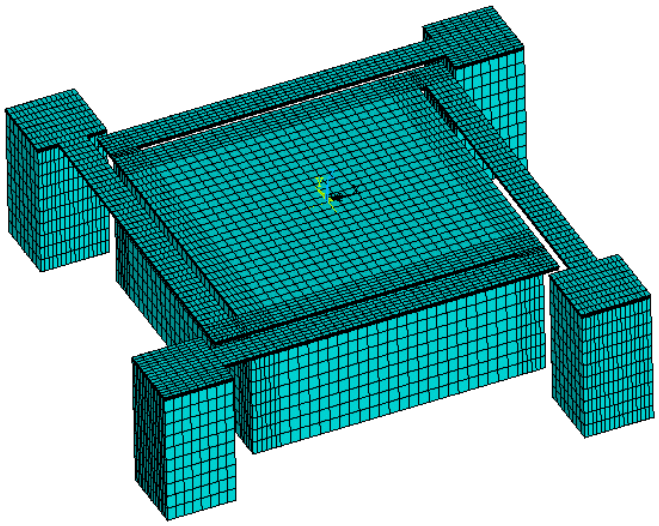

Fig. 3. 10 The dense mesh generation of the FEM model

3.4.2 Detection of AZ Acceleration

Fig. 3. 11 shows the stress distribution on the beam when the sensor is under a 1g vertical acceleration Az. Fig. 3. 12 shows the stress distribution in the X-oriented, Y-oriented and Z-oriented of the first beam caused by the acceleration Az. Clearly, the stress distribution in the direction along the beam is much larger than the others'.

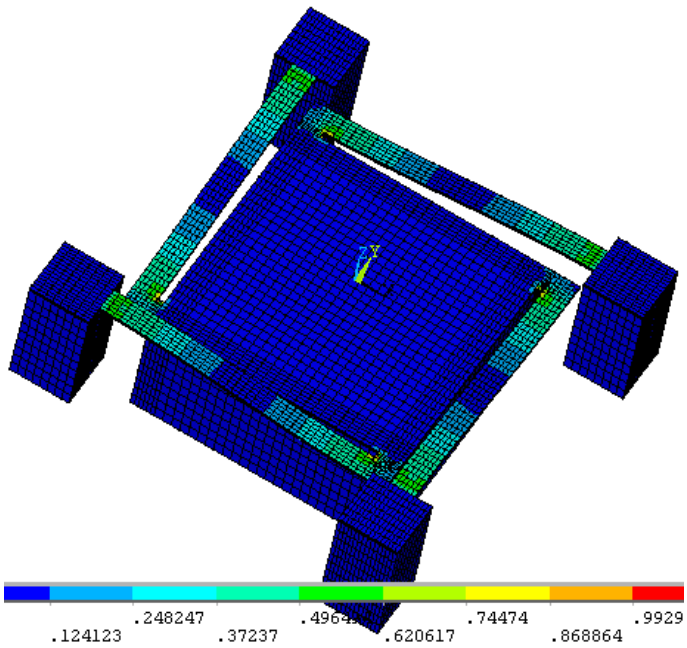

Fig. 3. 11 The stress distribution on the beams caused by the acceleration Az.

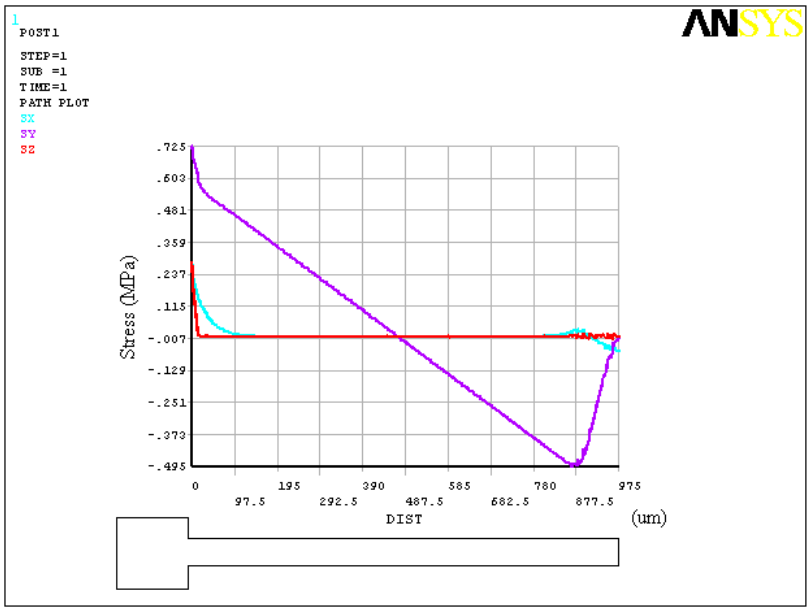

Fig. 3. 12 The stress distribution on the first beam

3.4.3 Detection of AY Acceleration

Fig. 3. 13 shows the stress distribution in the case there is a transverse acceleration Ay applying to the sensing chip.

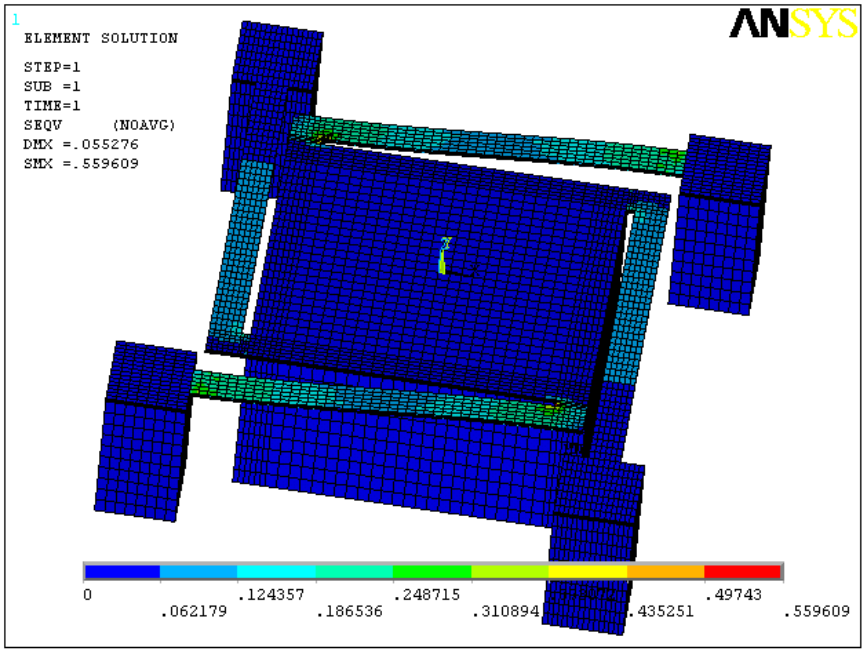

Fig. 3. 13 The stress distribution on the beams caused by the acceleration Ay.

Fig. 3. 14, Fig. 3. 15, Fig. 3. 16, and Fig. 3. 17 represent the stress distribution in four beams when applying AY to the sensing chip, respectively.

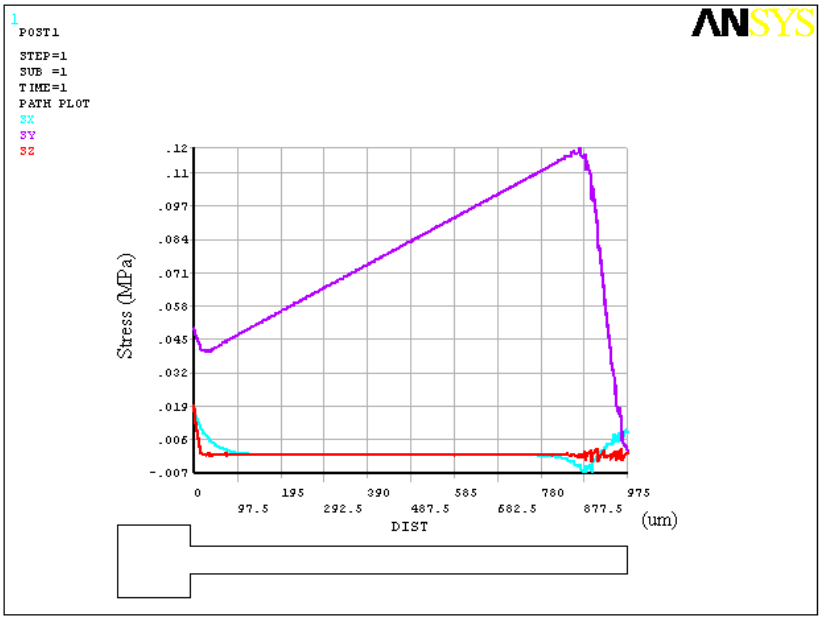

Fig. 3. 14 Stress distribution on the surface of the first beam due to the 1g acceleration Ay

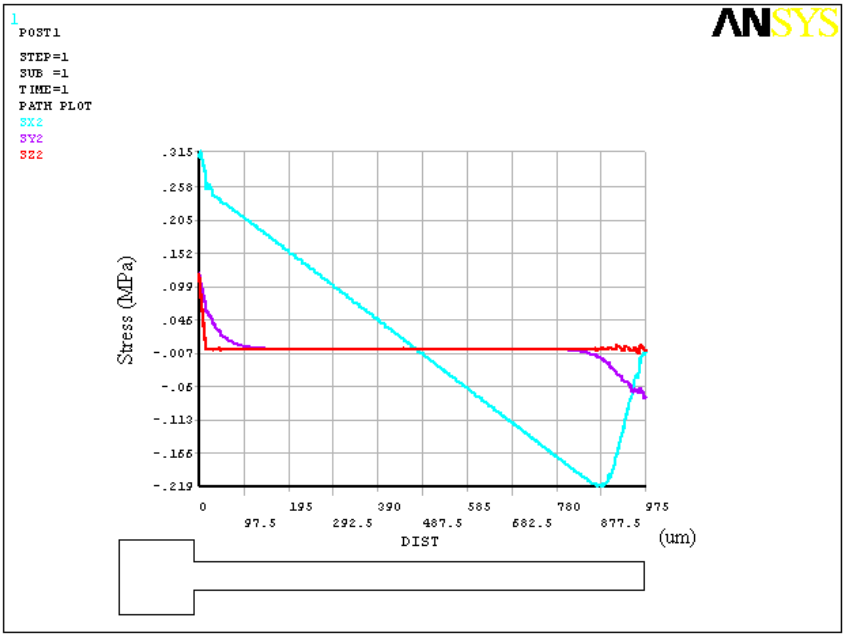

Fig. 3. 15 Stress distribution on the surface of the second beam due to the 1g

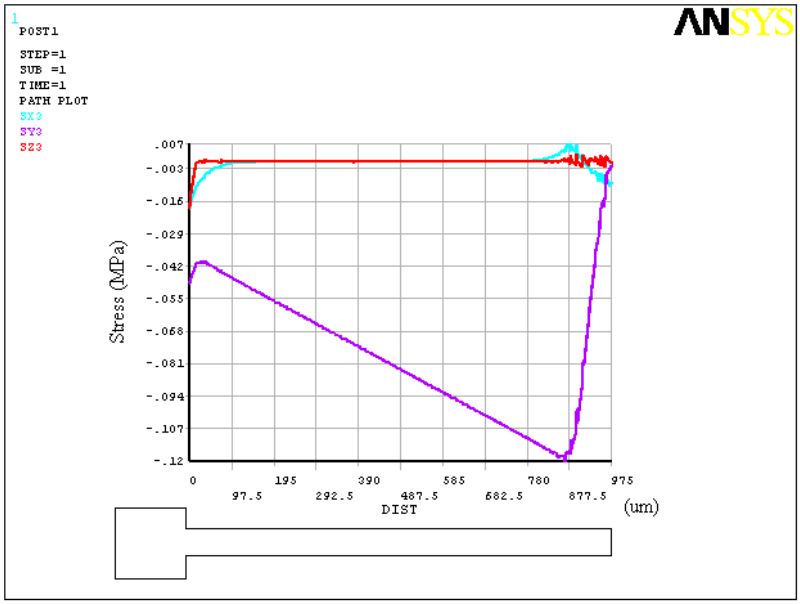

Fig. 3. 16 Stress distribution on the surface of the third beam due to the 1g acceleration Ay

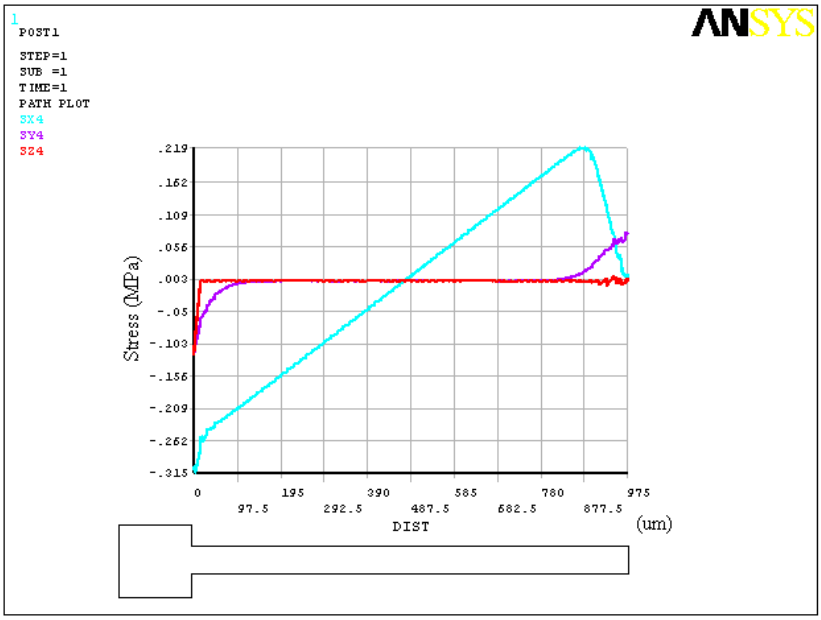

Fig. 3. 17 Stress distribution on the surface of the fourth beam due to the 1g acceleration Ay

Fig. 3. 18 shows the stress analysis results along the 1st and the 3rd beams when the sensor is submitted to acceleration in three directions (X, Y and Z). From this figure, we can pinpoint the optimal locations for the piezoresistors in order to sense accelerations Ax and Az without cross-talk. By the same token, acceleration Ay can

be sensed via four piezoresistors on the 2nd and the 4th beams.

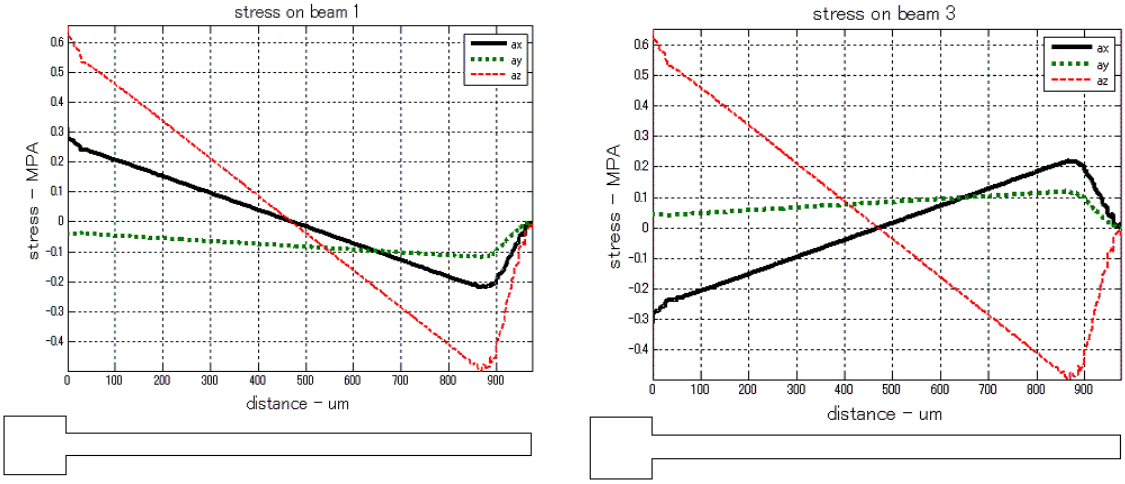

Fig. 3. 18 Longitudinal stresses on the surface of the 1st and the 3rd beams due to the 1g acceleration

Based on the stress distribution in the flexure beams, twelve piezoresistors are placed to maximize the sensitivities to three components of acceleration and eliminate the cross-sensitivity. The sensing principle of the sensor is based on the characteristic of the p-type piezoresistor. These identical piezoresistors are diffused on the surface of the beams to form three Wheatstone bridges.

3.5 Measurement Circuits

Based on the stress distribution in the flexure beams, twelve piezoresistors are placed to maximize sensitivity to the three acceleration components and minimize cross-sensitivity. The behavior of the sensor is captured in Table 1 based on the characteristics of the p-type piezoresistor [71]. The resistance decreases when the sensor is exerted by a compressive stress and increases when it is exerted by a tensile stress. These identical piezoresistors are diffused on the surface of the beams to form three Wheatstone bridges as shown in Fig. 3. 19.

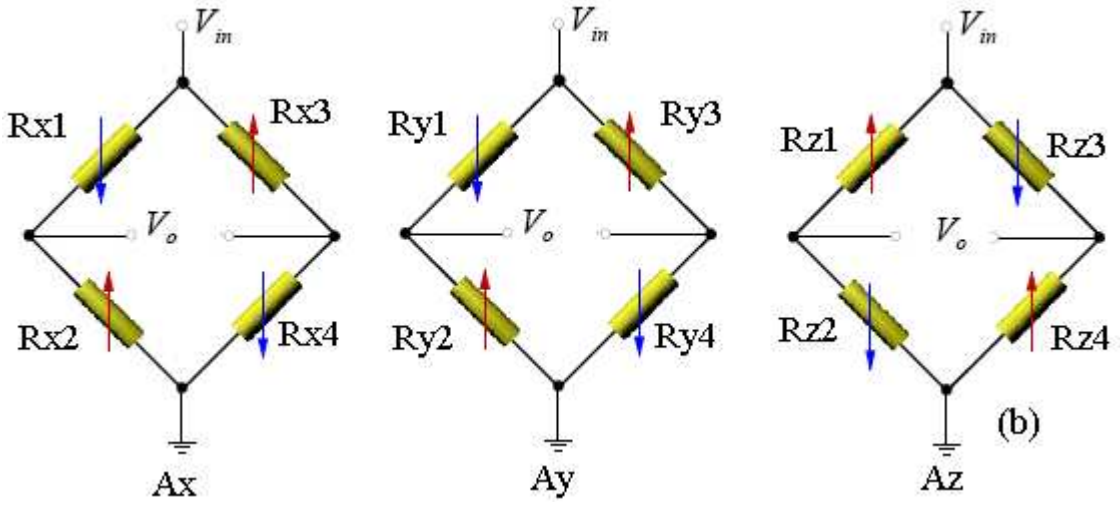

Fig. 3. 19 Three Wheatstone bridges

In this design, a micro Wheatstone-bridge circuit consisting of four p-type piezoresistors is used as shown in Fig. 3. 19. With an input voltage V_{in}, the output voltage V_{out} can be expressed as a function of resistances of four piezoresistors R_1-R_4:

$$V_{out} = \left(\frac{R_1}{R_1 + R_2} - \frac{R_3}{R_3 + R_4} \right) \tag{3.3}$$

Taylor expansion on the first-order terms can be written as follows to describe the relationship between V_{out} and ΔR_i where ΔR_i is the individual resistance change.

$$V_{out} = V_{offset} + \sum_{i=1}^{4} \left(\frac{\partial V_{out}}{\partial R_i} \right) \Delta R_i \tag{3.4}$$

where V_{offset} is the output voltage when there is no stress.

Replace (3.3) to (3.4), we can obtain:

$$V_{out} = V_{offset} + \left[\frac{R_1 R_2 \left(\frac{\Delta R_1}{R_1} - \frac{\Delta R_2}{R_2} \right)}{(R_1 + R_2)^2} + \frac{R_3 R_4 \left(\frac{\Delta R_4}{R_4} - \frac{\Delta R_3}{R_3} \right)}{(R_3 + R_4)^2} \right] V_{in} \tag{3.5}$$

Because the resistance values of $R_1 - R_4$ are nearly the same, the equation (3.5) can be rewritten to:

$$V_{\text{out}} = \frac{1}{4}\left(\frac{\Delta R_1}{R_1} - \frac{\Delta R_2}{R_2} - \frac{\Delta R_3}{R_3} + \frac{\Delta R_4}{R_4}\right)V_{in} \tag{3.6}$$

In our case, when the structure is in a balanced state, the output voltage is zero. When the sensor is undergoing acceleration, the Wheatstone bridges become unbalanced and a voltage appears at their output. When the sensor is submitted to acceleration in an arbitrary direction, the output is given by:

$$\begin{aligned} V_1 &= \frac{1}{4}\left(\frac{\Delta Rx1}{Rx1} - \frac{\Delta Rx2}{Rx2} - \frac{\Delta Rx3}{Rx3} + \frac{\Delta Rx4}{Rx4}\right)V_{in} \\ V_2 &= \frac{1}{4}\left(\frac{\Delta Ry1}{Ry1} - \frac{\Delta Ry2}{Ry2} - \frac{\Delta Ry3}{Ry3} + \frac{\Delta Ry4}{Ry4}\right)V_{in} \\ V_3 &= \frac{1}{4}\left(\frac{\Delta Rz1}{Rz1} - \frac{\Delta Rz2}{Rz2} - \frac{\Delta Rz3}{Rz3} + \frac{\Delta Rz4}{Rz4}\right)V_{in} \end{aligned} \tag{3.7}$$

From stress analysis above, we found that $\sigma_l >> \sigma_t$. Thus, we can rewrite the equation (3.2) as:

$$\frac{\Delta R}{R} \approx \pi_l \sigma_l \tag{3.9}$$

We can summarize the change of resistance value with three components of acceleration in Table 3. 3. The values a, b, c_1, and c_2 are illustrated in Fig. 3. 20 where $0 < c_1 < c_2 << b < a$.

Table 3. 3 Resistance changes due to application of accelerations

	$\Delta Rx_1/R$	**$\Delta Rx_2/R$**	**$\Delta Rx_3/R$**	**$\Delta Rx_4/R$**	**$\Delta Ry_1/R$**	**$\Delta Ry_2/R$**	**$\Delta Ry_3/R$**	**$\Delta Ry_4/R$**	**$\Delta Rz_1/R$**	**$\Delta Rz_2/R$**	**$\Delta Rz_3/R$**	**$\Delta Rz_4/R$**
Ax	**b**	**-b**	**-b**	**b**	**$-c_1$**	**$-c_2$**	**c_2**	**c_2**	**-b**	**b**	**-b**	**b**
Ay	**$-c_1$**	**$-c_2$**	**c_1**	**c_2**	**b**	**-b**	**-b**	**b**	**-b**	**b**	**-b**	**b**
Az	**a**	**-a**	**a**	**-a**	**a**	**a**	**-a**	**-a**	**-a**	**a**	**a**	**-a**

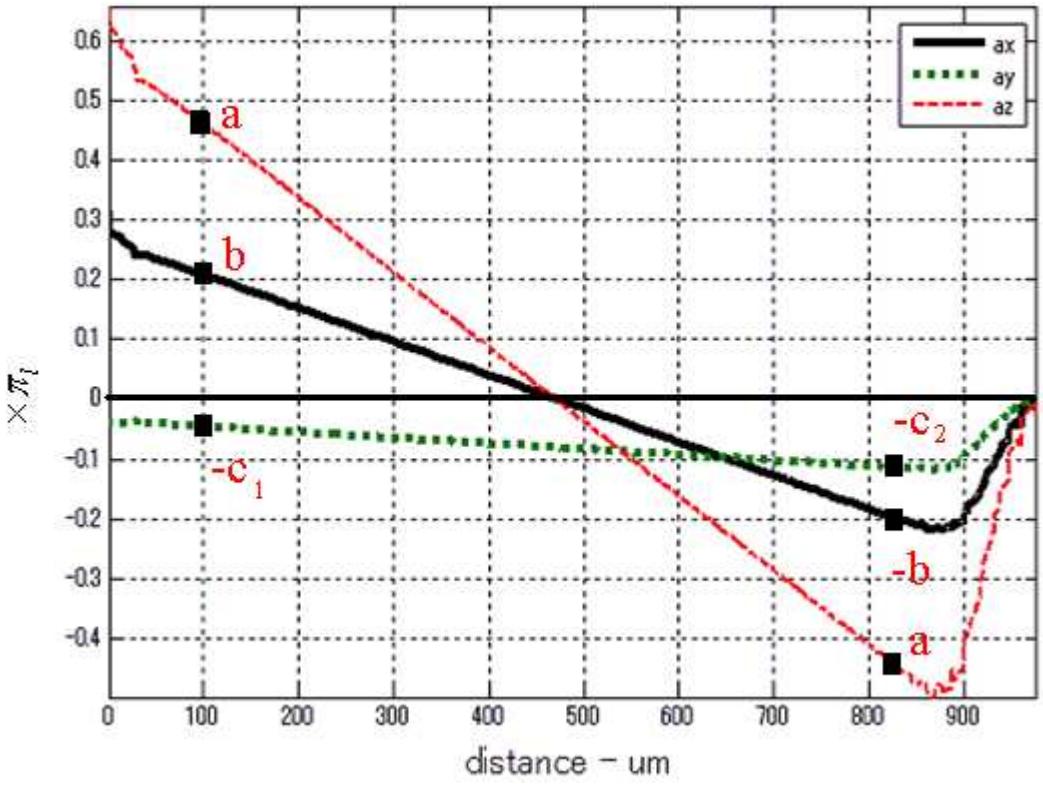

Fig. 3. 20 Illustrating the change of resistance values

When the sensor is only submitted to the Az acceleration component, the output can be easily found from equation (3.6) and Table 3. 3, i.e.:

$$\begin{aligned} V_1 &= 0 \\ V_2 &= 0 \\ V_3 &= \frac{\Delta Rz_1}{Rz_1} V_{in} = a \end{aligned} \tag{3.11}$$

When the sensor is strictly reacting to the Ax acceleration component, we have

$$\begin{aligned} V_1 &= b \\ V_2 &= \frac{c_2 - c_1}{2} \to 0 \\ V_3 &= 0 \end{aligned} \tag{3.12}$$

Likewise, we can write

$$\begin{aligned} V_1 &= \frac{c_2 - c_1}{2} \to 0 \\ V_2 &= \mathrm{b} \\ V_3 &= 0 \end{aligned} \tag{3.13}$$

when only the Ay component is applied.

Table 3. 4 can simply replace for Table 3. 3 in order to summarize the increase (+), decrease (-), or invariable (0) in resistance of piezoresistors due to application of accelerations Ax, Ay, and Az.

Table 3. 4 Resistance changes due to application of accelerations Ax, Ay, and Az.

	Rx_1	Rx_2	Rx_3	Rx_4	Ry_1	Ry_2	Ry_3	Ry_4	Rz_1	Rz_2	Rz_3	Rz_4
Ax	+	-	-	+	-	-	+	+	+	-	+	-
Ay	-	-	+	+	+	-	-	+	+	-	+	-
Az	+	-	+	-	+	+	-	-	+	-	-	+

3.6 Multiphysic Analysis of the 3-DOF Accelerometer

In this section, a novel multiphysic analysis was developed for performance prediction of the designed sensor. ANSYS software was utilized again as the basis to simulate the thermal, mechanical, and piezoresistive properties of the silicon based accelerometer. This analysis is necessary to improve and optimize the performance of the device. The flow chart of the process is shown in Fig. 3. 21.

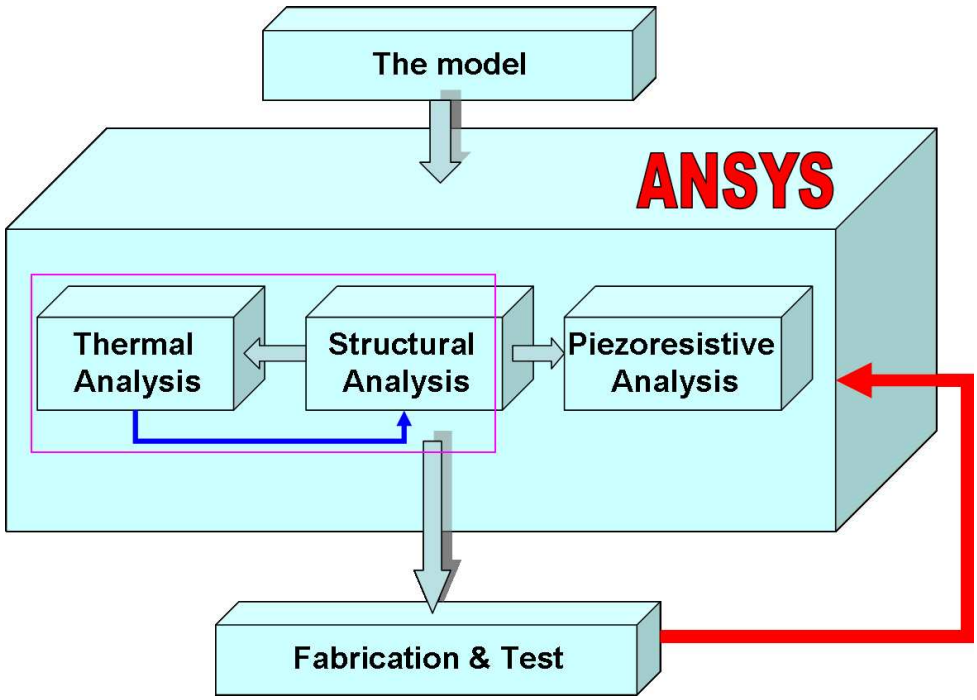

Fig. 3. 21 Flow chart of the coupled analysis

3.6.1 Thermal-Structural Coupled Analysis

Piezoresistive sensors have the disadvantage of being highly sensitive to temperature changes [6],[41][51]. To predict the characteristics of the piezoresistive accelerometer, a coupled-field model analysis is necessary [20]. Conventionally two different numerical codes were used for computations of the temperature distribution, structure sensitivity and voltage output, separately. Thus the time-consuming work of model establishment has to be done at each analysis step and errors are not ignored.

In this section, coupled field simulation program was utilized to analysis the sensitivity performance of the accelerometer. The program consists of two phases: thermal and mechanical analyze based on ANSYS software. This commercial software also provides the ability to link between thermal and structural analyses. Obviously this linked coupled-field analysis is more efficient because the model can be established by single software and the related data can be transferred easily in between elements due to same mesh employed. The SOLID87 and SOLID92 elements were used for thermal-structural calculations, respectively.

Silicon acceleration sensors suffer from the temperature, which will affect the circuitry performance of the sensor. These piezoresistor can act as heat sources due to forming the Wheatstone circuits [51][52]. The thermal stress is induced by a temperature distribution. This stress is then converted into electrical signals by using Wheatstone bridge circuits. To estimate the change in temperature due to self heating, different pathways of heat transfer have been considered as shown in Fig. 3. 22.

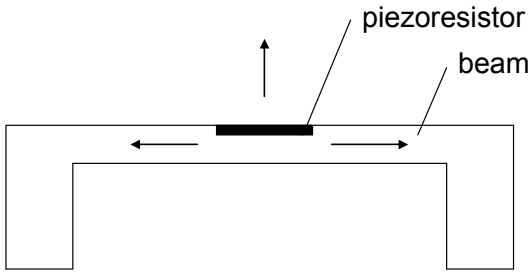

Fig. 3. 22 Piezoresistor acts like a heat source in the sensor with different heat transfer paths

Along the beam one has to deal with heat conduction. The basic assumption in

applying the heat equation to this kind of MEMS sensor is that there is no convection or radiation loss from the lower end of the beam. So this region is an adiabatic region. The heat source in this case is self heating phenomena.

In general, heat conduction can be described by the Fourier's law [13]:

$$q = -k\nabla T = -k\left(i\frac{\partial T}{\partial x} + j\frac{\partial T}{\partial y} + m\frac{\partial T}{\partial z}. \right) \tag{3.13}$$

or

$$q = -k\frac{\partial T}{\partial n.} \tag{3.14}$$

where q represents heat flux on direction n, k represents heat conductivity, ∇ represents three-dimension operand, T represents vector temperature field, i, j, m represent the unit vector of three-dimensions Cartesian coordinate (x, y, z).

According to heat conduction theory, the energy and Fourier's conversion in three-dimensional Cartesian coordinate is:

$$\frac{\partial}{\partial x}\left(k\frac{\partial T}{\partial x} \right) + \frac{\partial}{\partial y}\left(k\frac{\partial T}{\partial y} \right) + \frac{\partial}{\partial z}\left(k\frac{\partial T}{\partial z} \right) + Q = \rho.c_P.\frac{\partial T}{\partial t} \tag{3.15}$$

where $\rho.c_P.\frac{\partial T}{\partial t}$ represents the change rate of the internal energy of the unit volume in pace with time; Q represents the rate of producing energy in a unit volume:

$$Q = \frac{q}{k} = -\frac{P}{k.V} \tag{3.16}$$

where P is the power consumption of the piezoresistor and V is the volume of the piezoresistor.

The relevant boundary conditions are as follows:

$$\frac{\partial T}{\partial n} = 0 \qquad at \qquad n = 0 \tag{3.17}$$

Assumed the piezoresistor to be perfect conductor, so:

$$-k\frac{\partial T}{\partial n} = h\left(T - T_{amb} \right) \quad at \qquad x = l, y = w, z = t \tag{3.18}$$

where h is the proportionality constant known as the heat transfer coefficient which depends on the material and the surrounding atmosphere T_{amb}.

Because it is often difficult to find the analytical solution, we can use FEM method

or simply the problem as shown in [64]. According to his research, the steady state of temperature rise can be calculated:

$$v = \frac{R_T P}{1 + \alpha_R R_T P} \approx R_T P \tag{3.19}$$

where

R_T=16.5 K/W (thermal resistance)

α_R=2500e-6 K^{-1} (TCR)

P is the power consumption of each piezoresistor.

Approximation can be made because $1 >> \alpha_R R_T P$ with the value of power around 8 mW. Equation (3.19) shows the linear relation between v and P.

The most important aspect of FEA in our design process is the analysis of the stress distribution in the flexure beams. Based on this distribution, piezoresistors are positioned to eliminate the cross-axis sensitivities and to maximize the sensitivities to the three acceleration components. But silicon acceleration sensors suffer from the temperature, which will affect the circuitry performance of the sensor. These piezoresistor can act as heat sources due to forming the Wheatstone circuits. The thermal stress is induced by a temperature distribution. This stress is then converted into electrical signals by using Wheatstone bridge circuits.

Return to the case the vertical acceleration is applied to the sensor: Firstly, the structural analysis of the sensing chip was done by using ANSYS software. Fig. 3. 23 shows the stress distribution in the X-oriented, Y-oriented and Z-oriented of the first beam caused by the acceleration AZ. We should not utilize coupled field analysis directly at this step. The reason is that we have to determine where to place piezoresistors by structural analysis.

Thermal analyses are used to calculate the temperature distribution on the beams. The piezoresistors are modeled using the SOLID87. The ANSYS program uses a heat balance equation obtained from the principle of conservation of energy as the basis for thermal analysis. All three primary modes of heat transfer-conduction, convection, and radiation are handled by the ANSYS program. The thermal analysis

here is performed with assume there is no convection or radiation.

For simulation, the values of the various constants that have been considered are: k (thermal conductivity of silicon) = 150$Wm^{-1}K^{-1}$, h (heat transfer coefficient) = 2.219 $Wm^{-2}K^{-1}$, c (specific heat of silicon) = 712 $JKg^{-1}K^{-1}$ [51]. Note that the thermal conductivity calculated here may be not linear for the operating range of temperature. Fig. 3. 23 represents the thermal distribution in the structure of the sensor.

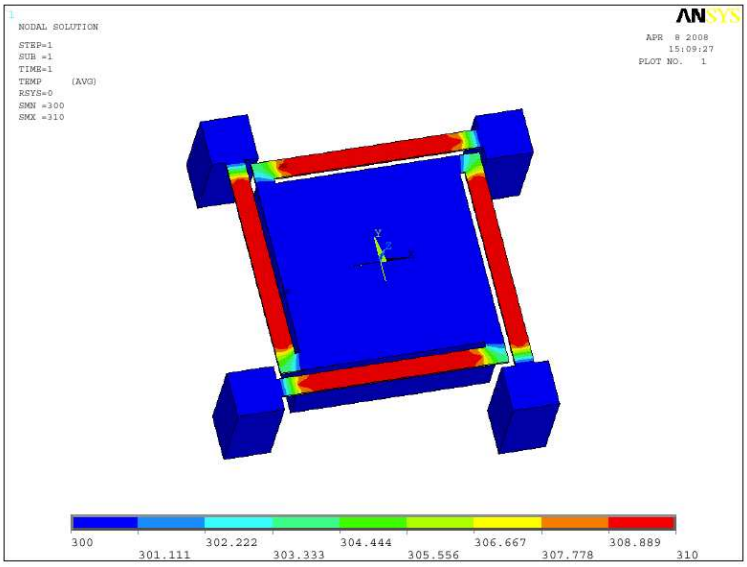

Fig. 3. 23 Thermal distribution in the sensor

The thermal stress on the sensor is calculated. It is observed that the temperature distribution at two fixed-ends of the beam is shown to be quite different. Note that greater the thickness of the beam, lesser is the effect of self heating. But, on the other hand, to increase the sensitivity, thickness of the beam needs to be reduced. Fig. 3. 24 shows the thermal stress distribution in the X-oriented, Y-oriented and Z-oriented of the first beam. The stress near two fix-end of the beam is quite large due to the temperature distribution.

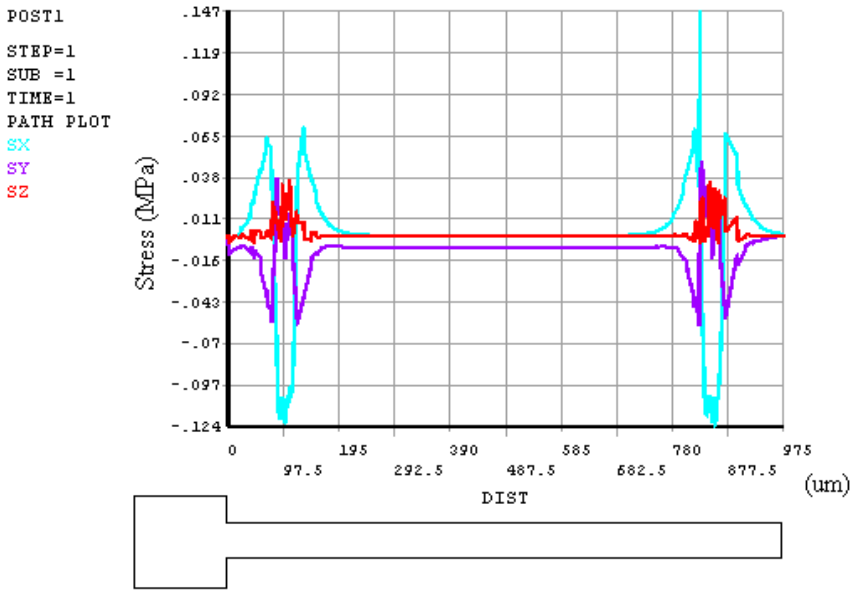

Fig. 3. 24 The stress distribution on the first beam due to thermal effect

Fig. 3. 25 shows the stress distribution in the X-oriented, Y-oriented and Z-oriented of the first beam caused by the acceleration Az and thermal effect, concurrently. This analysis is suitable for the real operating condition of the sensor.

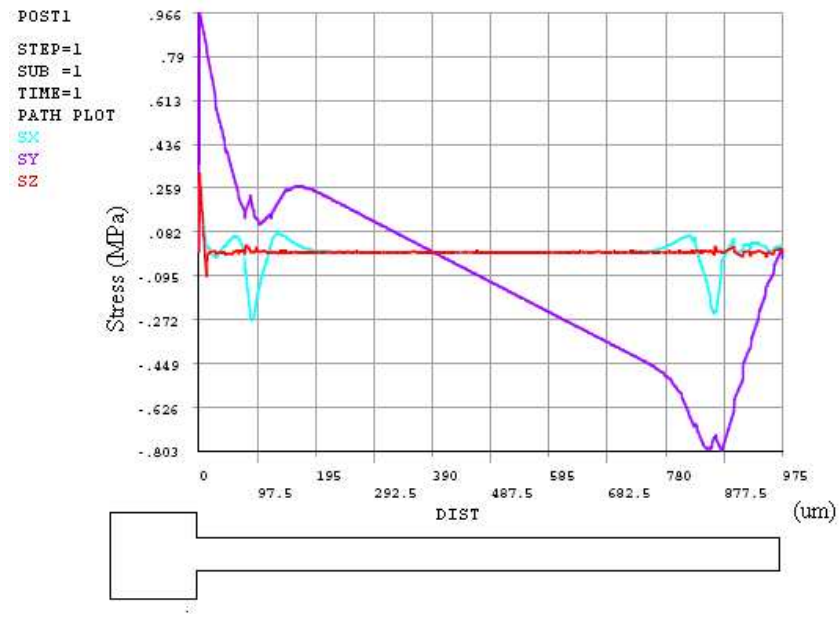

Fig. 3. 25 The stress distribution on the first beam due to the vertical acceleration and thermal effect

The sensitivity is compared to the structural solution with a different of 15%. This

coupled field analysis can also fill the gap between theoretical and experimental results. Obviously, the new analysis can give us more informative and reliable result than the previous one. Base on these analyses, an effective heat disinfestations system need to be developed.

3.6.2 Structural-Piezoresistive Coupled Analysis

The commercial FEA (Finite-Element-Analysis) code ANSYS provides the ability to link the piezoresistive analysis with structure analyses. The resistors areas are modeled using the piezoresistive option of the coupled-field solid SOLID227 while the structural part of the beam is modeled using SOLID92. The resistors are connected into a Wheatstone bridge arrangement by coupling the VOLT degrees of freedom on width sides of the resistors (see Fig. 3. 26). The supply voltage is applied to the master node of the driving electrode. The applied acceleration results in a stress distribution. The resistors (Ry_1 and Ry_4) are perpendicular to the applied stress, and change their resistance due to the piezoresistive effect. A static analysis is performed to determine the output voltage Vo.

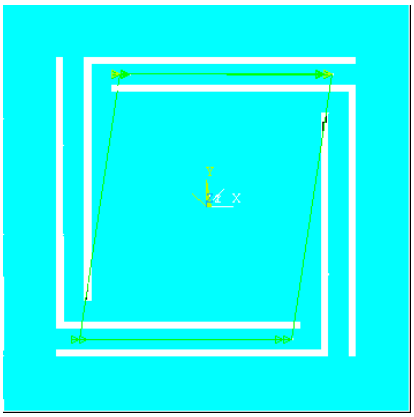

Fig. 3. 26 The Wheatstone bridge of the AY acceleration

The applied acceleration results in stress redistribution, leading to the variation of the piezoresistors, giving rise to an output voltage that depends on the input acceleration as shown in Fig. 3. 27.

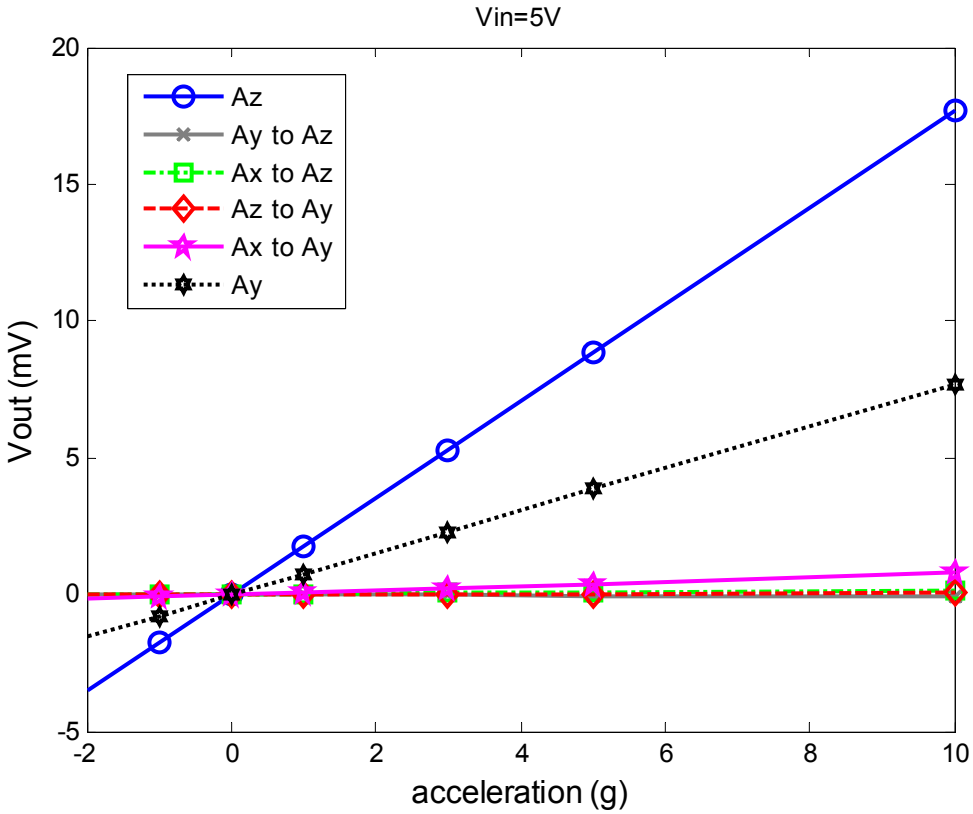

Fig. 3. 27 The sensing and crosstalk voltages obtained by the ANSYS program

3.7 Noise Analysis

This section describes the effect of noise to desired signal. The analysis of noise is very necessary for design and fabrication. In practice, the sensitivity is affected by these following effects: the intrinsic noise due to damping, the noise from the measuring circuit, residual calibration errors and drift problems…In the scope of this thesis, we consider the noise voltage for the detection circuit consists of thermal (Johnson), 1/f noise, and thermo-mechanical noise [23].

Cross axis sensitivity is another important characteristic. The sensor should be sensitive in one axis only. Misalignment of the device can lead to cross-axis sensitivity. But the sensor can also have an intrinsic cross axis response.

Using measuring circuit and good calibration technique, we can reduce electric noises to quite low values but the Johnson, 1/f and thermo-mechanical noise.

3.7.1. Johnson noise

Johnson noise (thermal noise) is the electronic noise generated by the thermal agitation of the charge carriers inside an electrical conductor when applying an arbitrary voltage. The power spectral density (PSD) of thermal noise is nearly constant throughout the frequency spectrum. It means that Johnson noise can be assumed to be White noise.

In fact, it is hardly to observe this noise in a realistic accelerometer because electrical noise in the measurement circuit is often larger. The rms voltage of equivalent acceleration noise in each piezoresistor is:

$$V_i^{Johnson} = \sqrt{4k_B T B_i R} \quad i = X, Y, Z \tag{3.20}$$

where k_B= 1.38 x 10^{-23} J/K is Boltzmann's constant, T is temperature in resistors, R is resistance value of the piezoresistor, and B is measured bandwidth. The bandwidth can be determined by many parameters such as the sampling frequency, analogue filtering, the resonant frequency of the mechanical structure, or losses in the wires, etc. Fig. 3. 28 illustrates the impact of Johnson noise on typical acceleration while switching between +g and –g.

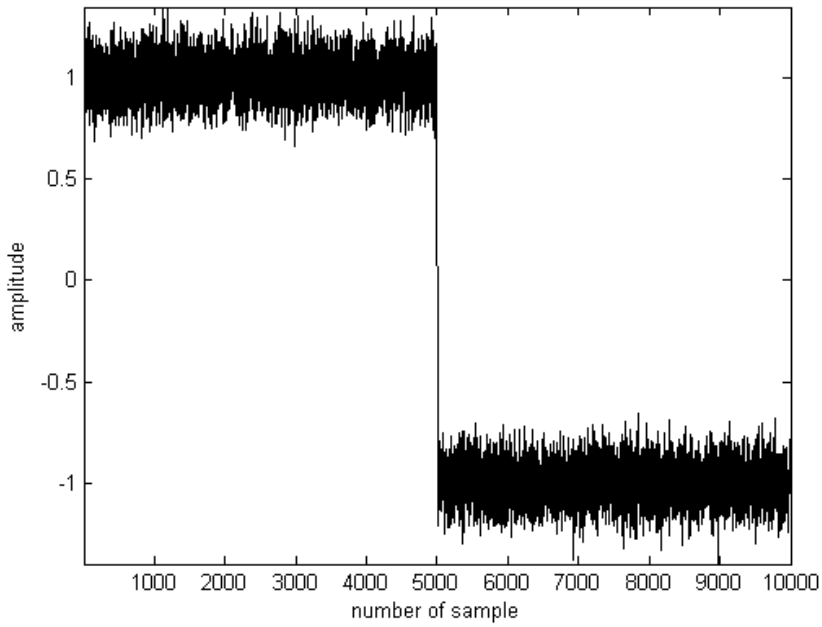

Fig. 3. 28 Impact of Johnson noise to acceleration signal

To design a high performance accelerometer, the minimum detectable acceleration must be reduced. It can be done by increasing the proof mass and reducing the

spring constant to minimize the resonant frequency. Further more, the oscillations near resonant frequency should be considered in the design (see Fig 2. 3).

3.7.2 Flicker noise (1/f noise)

Flicker noise presents in resistors, diodes, and transistors, and among other components. It is dependent on the total number of carriers, input voltage, and measured bandwidth [28]:

$$V_i^{1/f} = \sqrt{\frac{\alpha V_{in}^2}{N} \ln\left(\frac{f_{\max}^i}{f_{\min}^i}\right)} \quad i = X, Y, Z \tag{3.21}$$

where

V_{in} is input voltage across a piezoresistor,

N is total number of carriers and proportional to the volume of piezoresistors,

$f_{\max}^i$ and $f_{\min}^i$ determine the band of measurement frequency as: $B^i = f_{\max}^i - f_{\min}^i$

α is Hooge parameter which is a constant and dimensionless value [74]

Fig. 3. 29 shows the frequency response of a flicker noise. It is shown that the impact of flicker noise in the range of low frequency is stronger than the other.

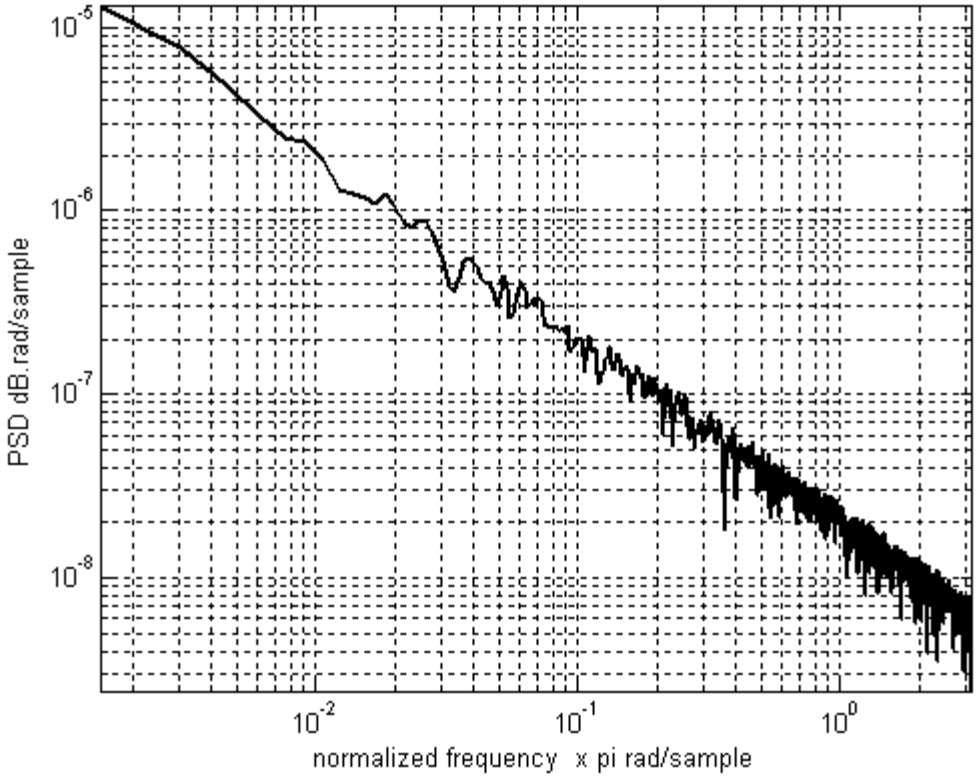

Fig. 3. 29 Power spectrum density of the flicker noise

3.7.3 Thermo-mechanical noise

Thermo-mechanical noise is analogous to the Brownian motion of particles. It can be interpreted as mechanical analog of Johnson noise in a resistor. This noise can be simplified as an equivalent force noise given by:

$$F_{thermomechanical,rms} = \sqrt{\frac{4k.k_B TB}{Q\omega_n}} \tag{3.22}$$

where

k is the sensor spring constant

$k_B T$ is the thermal energy

B is the measured bandwidth

Q is the mechanical quality factor

ω_n the resonance frequency.

In practice, all of the above-mentioned noise sources can act concurrently. The total noise spectral density is the sum of the each noise contributions. However, the thermo-mechanical noise is very small when comparing to Johnson and flicker noises. Thus, in this thesis total internal noise can be calculated as:

$$V_i^{noise} = \sqrt{\left(V_i^{Johnson,rms}\right)^2 + \left(V_i^{1/f}\right)^2} \quad i = X, Y, Z \tag{3.23}$$

In practical, we should mention to other noises caused by unstable input voltage, amplified circuit, ADC card (quantization noise).

.

Resolution is defined as the noise divided by the sensitivity.

$$R_i = \frac{V_i^{noise}}{S_i} \qquad i = X, Y, Z \tag{3.24}$$

The performance of the sensor can be summarized in Table 3. 5 with the input voltage V_{in} is 5 V. It is easy to see that the vertical direction is the most sensitive direction due to its smallest resonant frequency.

Table 3. 5 Performance parameters of the sensor

	Sensitivity (mV/V/g)	Johnson noise per 1 piezoresistor (μV)	1/f noise (μV)	Resolution (mg)
Az	0.336	0.415	0.031	0.495
Ax, Ay	0.152	0.513	0.036	1.353

3.8 Mask Design

The MEMS fabrication process requires precise photo masks to accurately create micro-scale patterns and structures. In this thesis, the sensor is fabricated with six photo masks for photolithography step in piezoresistor patterning, contact hole opening, interconnection wiring, crossbeam forming, and deep reactive ion etching from backside. The mask layout design was drawn using L-EDIT software.

- The first mask is used for positioning and patterning the piezoresistors on the silicon wafer.
- The second mask is used to define the contact hole. The contact hole plays a role as a window to make the Ohmic contact between the piezoresistor and the electrical wire.
- The third mask is to define a pattern on the back side of the mass
- The fourth defines the crossbeam of the sensor.
- The fifth masks are used to define the interconnection wiring in order to form Wheatstone circuits.
- The sixth mask is used to form the beam separation lines from the back side of the chip

3.8.1 Designing the Mask-1

Fig. 3. 30 shows the mask of a two-terminal piezoresistor. This mask is used for positioning and patterning the piezoresistors on the silicon wafer.

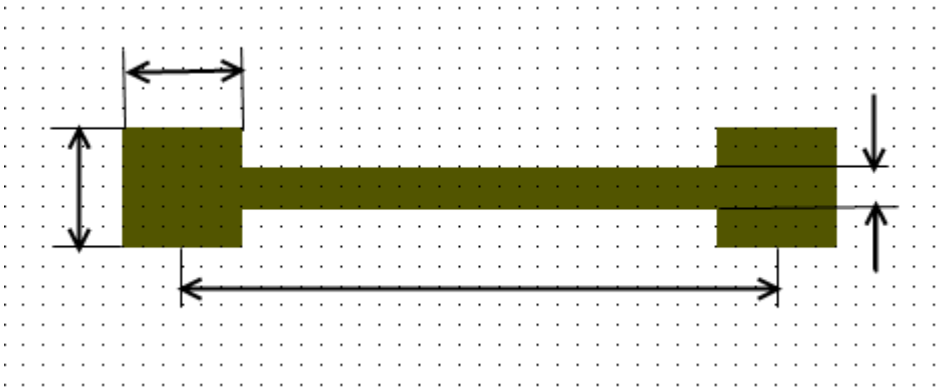

Fig. 3. 30 The first mask

3.8.2 Designing the Mask-2

Fig. 3. 31 shows the second mask of the contact hole. This mask is used for making the direct contact between the piezoresistor and the electrical wire.

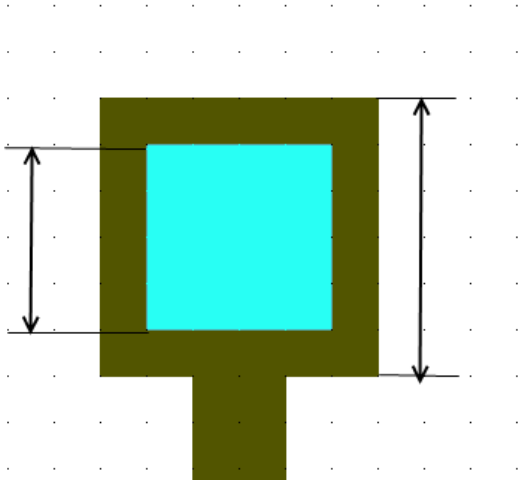

Fig. 3. 31 The second mask

3.8.3 Designing the Mask-3

The third mask shown in Fig. 3. 32 is used to define a pattern on the back side of the mass. It can help to reduce the mass height from the back side to make gap between bond surface of the sensor and the mass.

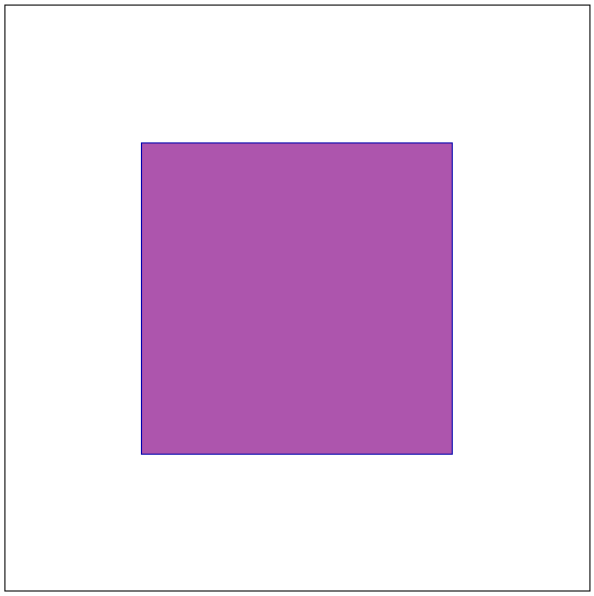

Fig. 3. 32 The third mask

3.8.4 Designing the Mask-4

The fourth mask shown in Fig. 3. **33** is used for forming the beam of the accelerometer.

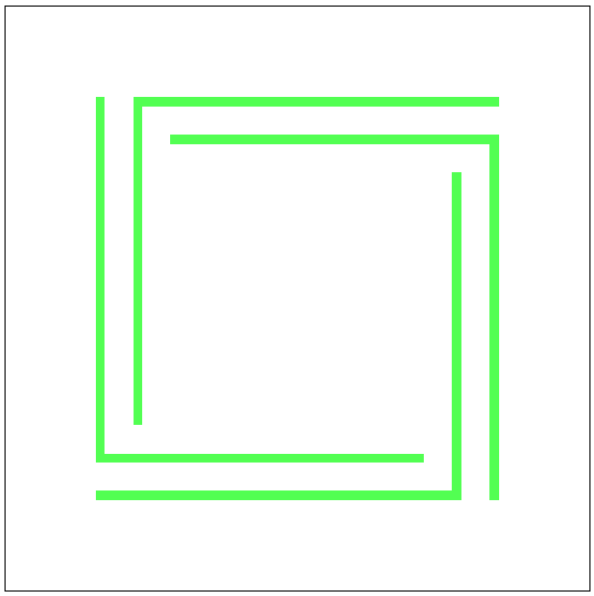

Fig. 3. 33 The fourth mask

3.8.5 Designing the Mask-5

The fifth mask can be used to pattern the wires interconnecting piezoresistor to form Wheatstone circuits. The mask drawing of interconnections and bonding pads of the sensor is shown in Fig. 3. 34.

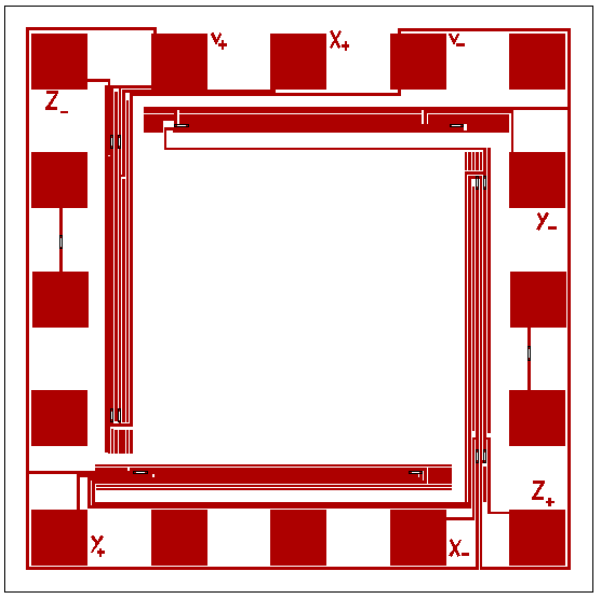

Fig. 3. 34 The fifth mask

3.8.6 Designing the Mask-6

The sixth mask shown in Fig. 3. 35 can be used to form the beam separation lines from the back side of the chip.

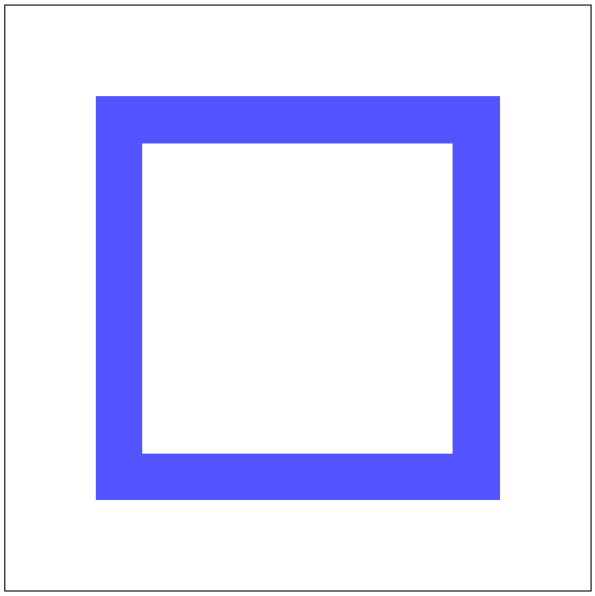

Fig. 3. 35 The sixth mask

Fig. 3. 36 shows an overlapped mask layout of the 3-DOF sensor. Note that we have six masks and we have to use four alignment steps

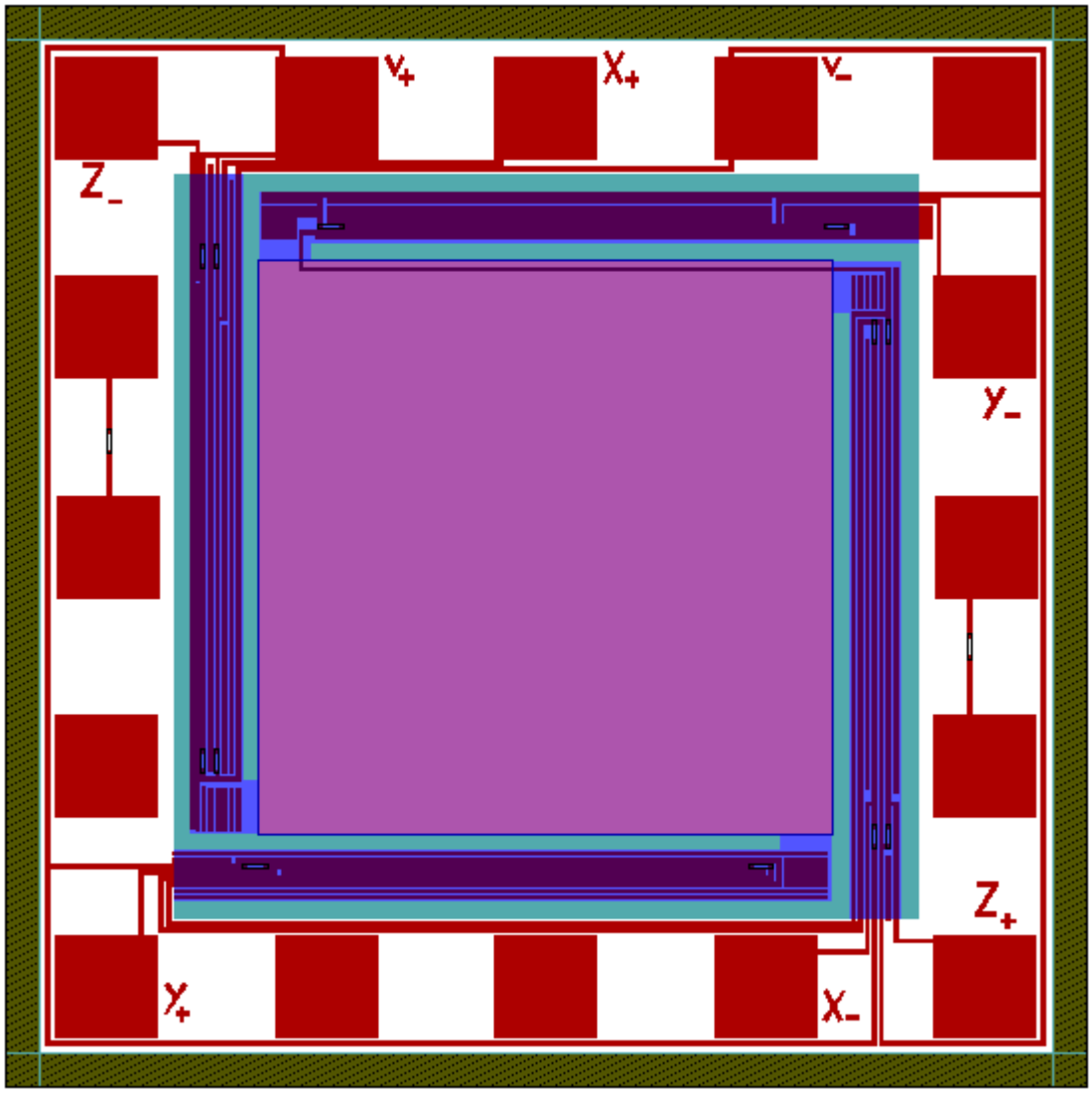

Fig. 3. 36 Overlapped mask layout of the 3-DOF sensor

3.9 Summary

This chapter presented a hierarchical MEMS design synthesis and optimization process developed for and validated by the design of a specific structure of accelerometer. The iterative synthesis design is largely based on the use of a MNA tool called SUGAR in order to meet multiple design specifications. After some human interactions, the design is brought to FEM software such as ANSYS for final validation and further optimization (such as placement of the piezoresistors in our case study). The optimal configuration was reached by exploiting the advantages of both types of simulations.

Also in this chapter, the more details on the design of the 3-DOF accelerometer were carefully analyzed. The structural analysis plays a major role in determining the positions to place the piezoresistors in order to eliminate cross-axis sensitivities and to maximize the sensitivity to the three acceleration components. Further more, the effects of electrical heating, the sensing and crosstalk sensitivities were investigated by thermal, mechanical and piezoresistive coupled-field simulations. To fully understand the sensor's performance, the instinct noises were also calculated. Finally, the main features of the masks were described to complete the design process.

CHAPTER 4

FABRICATION AND CALIBRATION OF THE 3-DOF ACCELEROMETER

4.1 Fabrication Process of the Acceleration Sensor

In this section, the fabrication of the accelerometer based on the integrated circuit (IC) technology is presented [26]. The whole fabrication process was implemented in MiNiDel lab, Japan. There are two main processes that mostly affect the sensor performance are ion diffusion and deep reactive ion etching (DRIE).
We can list the main processes for the fabrication of the 3-DOF accelerometer as the following [54]:

- Staring material SOI
- The oxidation process
- Piezoresistor patterning
- Contact hole opening
- Wire interconnection
- Beam formation by RIE
- Backside mass gap formation

4.1.1 Staring material SOI

The n-type SOI wafer illustrated in Fig 4. 1 is aligned with the plane (100). The thickness of the device layer, buried silicon layer, and substrate is 10 μm, 0.5 μm, and 480 μm, respectively.

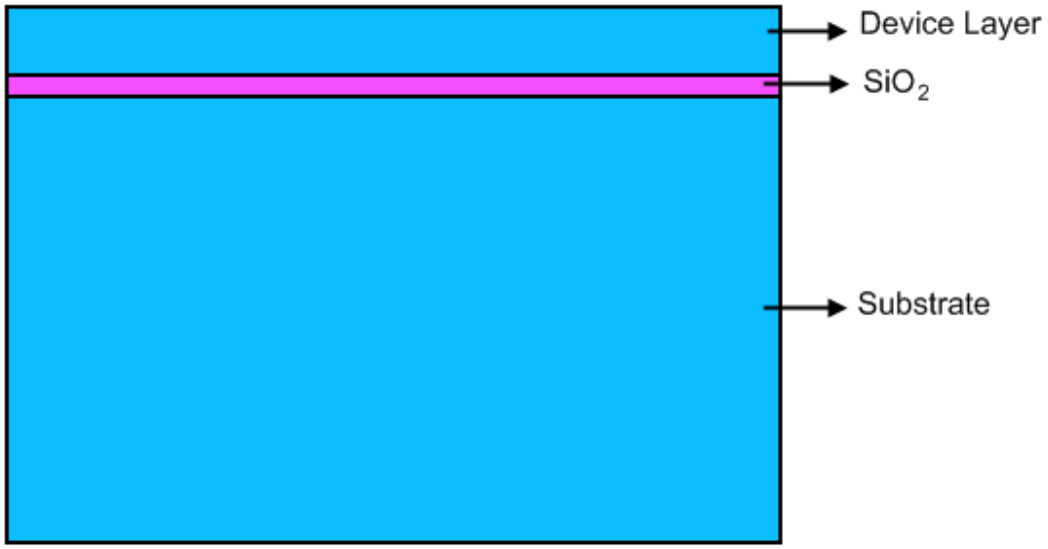

Fig 4. 1 The n-type SOI (100) wafer

4.1.2 The oxidation process

The thermal oxidation is the major process in MEMS technology. Fig 4. 2 illustrated the wafer after thermal oxidation process. The chemical reaction of this process is:

$$Si + 2H_2O \rightarrow SiO_2 + 2H_2$$

This process is obtained by taking the wafer into oxygen environment at high temperature (in the range of 900 to 1200 ^{o}C). The achieved SiO_2 insulator has the thickness of 0.3 μm.

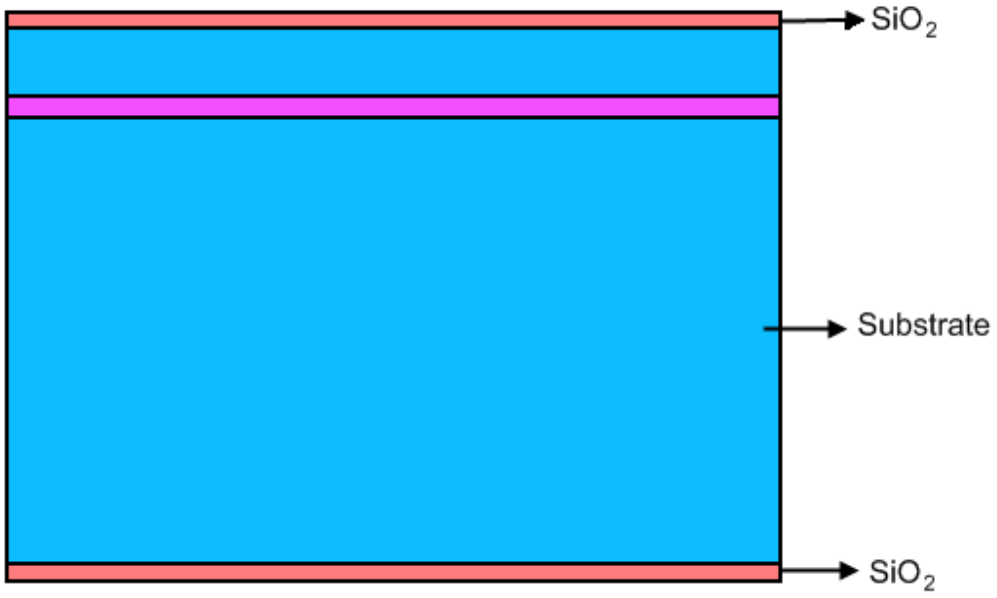

Fig 4. 2 The SiO_2 layer was formed in the wafer

4.1.3 Piezoresistor patterning

This is a very important process, which has strong influence to the performance of the sensor. The purpose of this process is to diffuse suitably boron ions into n-type silicon substrate to form p-type silicon piezoresistors. The piezoresistors were patterned so that their longitudinal axis aligns with the crystal directions <110> and $<1\bar{1}0>$ of n-type silicon (100).

The SiO_2 obtained in the second process have the ability to mask impurities during high temperature diffusion. Firstly, the piezoresistor pattern is formed by photolithography. Then the SiO_2 is etched by wet etching with hydrofluoric (HF) as the following reaction:

$$SiO_2 + 6HF \rightarrow H_2SiF_6 + 2H_2O$$

The wafer schematic after piezoresistors patterning is shown in Fig 4. 3. The piezoresistors are formed on the surface of the beam when boron ions are diffused by two step process. Fig 4. 4 is the wafer after the diffusion process. The more detail can be found in Ref [18].

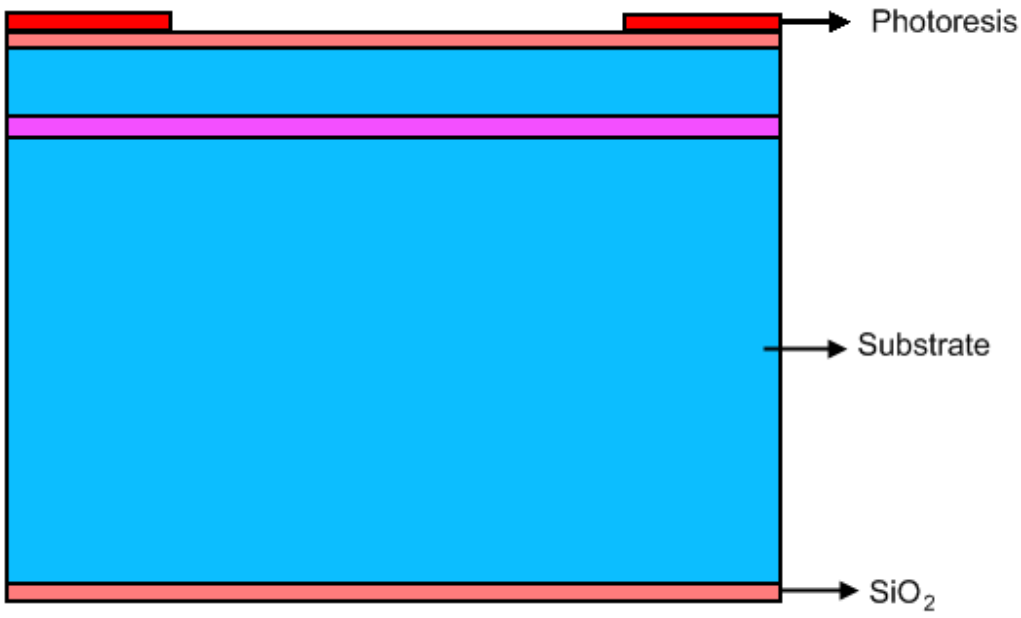

Fig 4. 3 Wafer after piezoresistors patterning

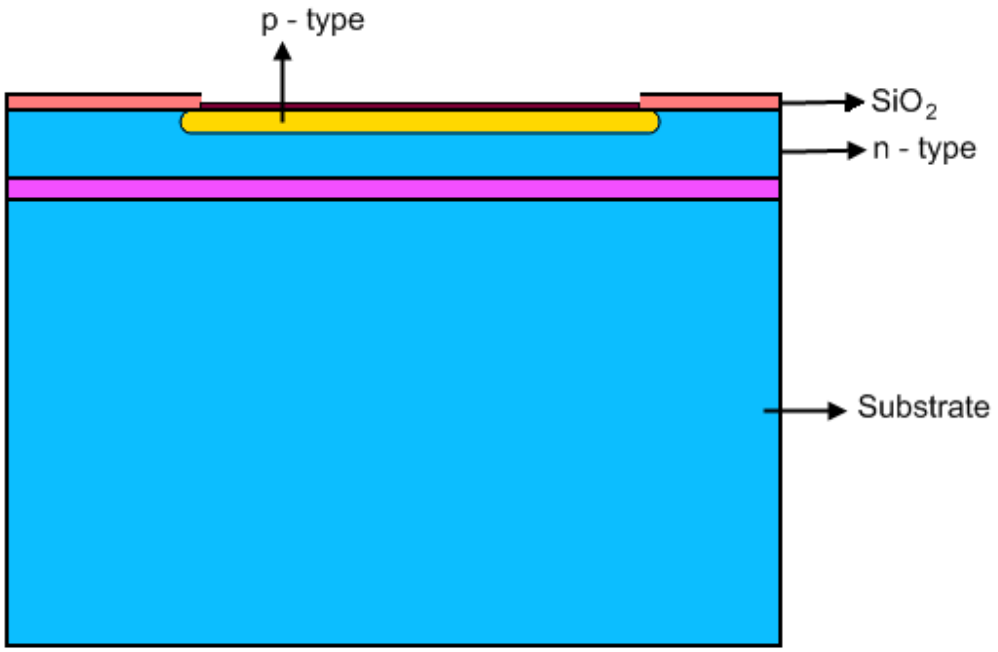

Fig 4. 4 The wafer after boron diffusion process

4.1.4 Contact hole opening

In this step, the photolithography process is applied to patterned contact holes (see Fig 4. 5). The contact holes will make the direct contact between piezoresistors and electrodes which will be formed in the fifth step. The BHF solution is then used to etch by wet etching process.

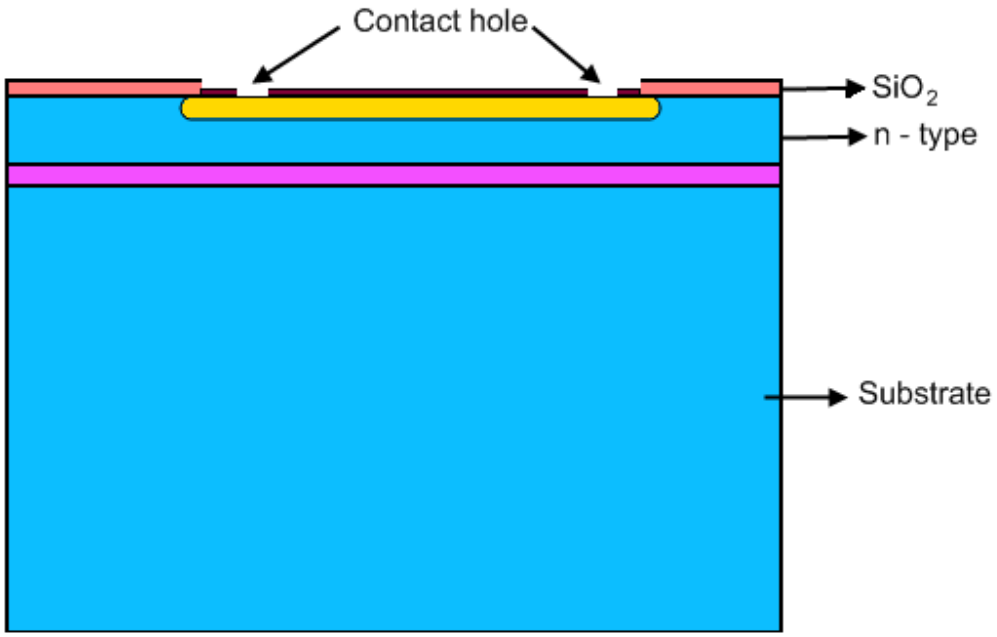

Fig 4. 5 The wafer after contact hole opening

4.1.5 Wire interconnection

Aluminum is chosen to be the material for interconnection wiring. The reason is that it has low resistivity and adheres well to SiO_2. After vacuum evaporation, photolithography, and etching processes, the wires and bonding pad are patterned (see Fig 4. 6). To make an Ohmic contact, we need also a sintering process. This process will make the strongly contact between metal and semiconductor.

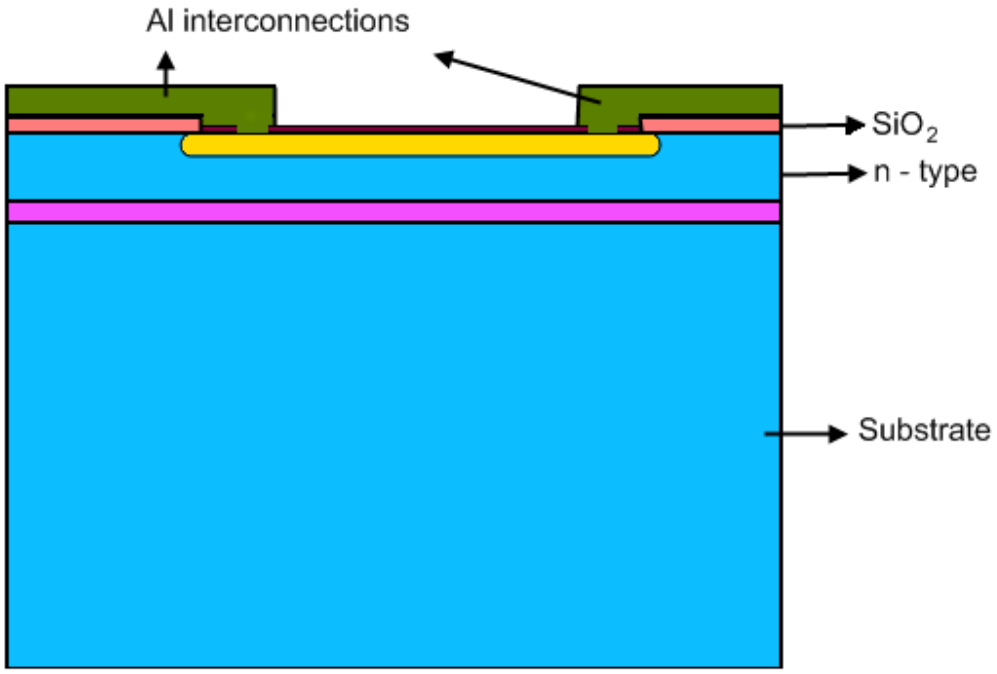

Fig 4. 6 The wafer after metallization process

The I-V characteristics of piezoresistors before and after sintering are shown in Fig. Fig 4. 7 and Fig 4. 8. From the Fig 4. 8 we can see that the resistance of the piezoresistors is about 702 Ω, corresponding to the sheet resistance is about 47 Ωcm^2. Thus, we can find the surface impurity concentration of Cs ≈ 5×10^{19} atoms cm^{-3}.

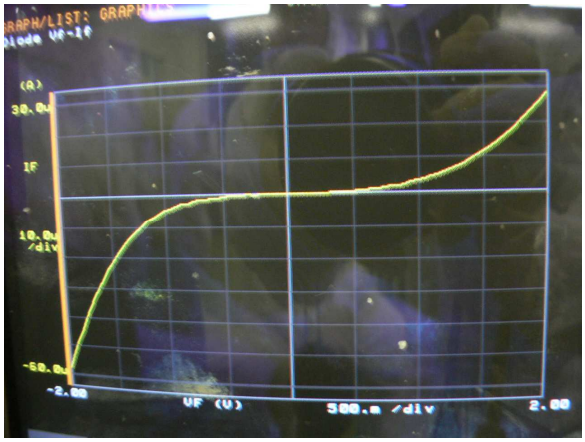

Fig 4. 7 I-V characteristic of piezoresistor before sintering process

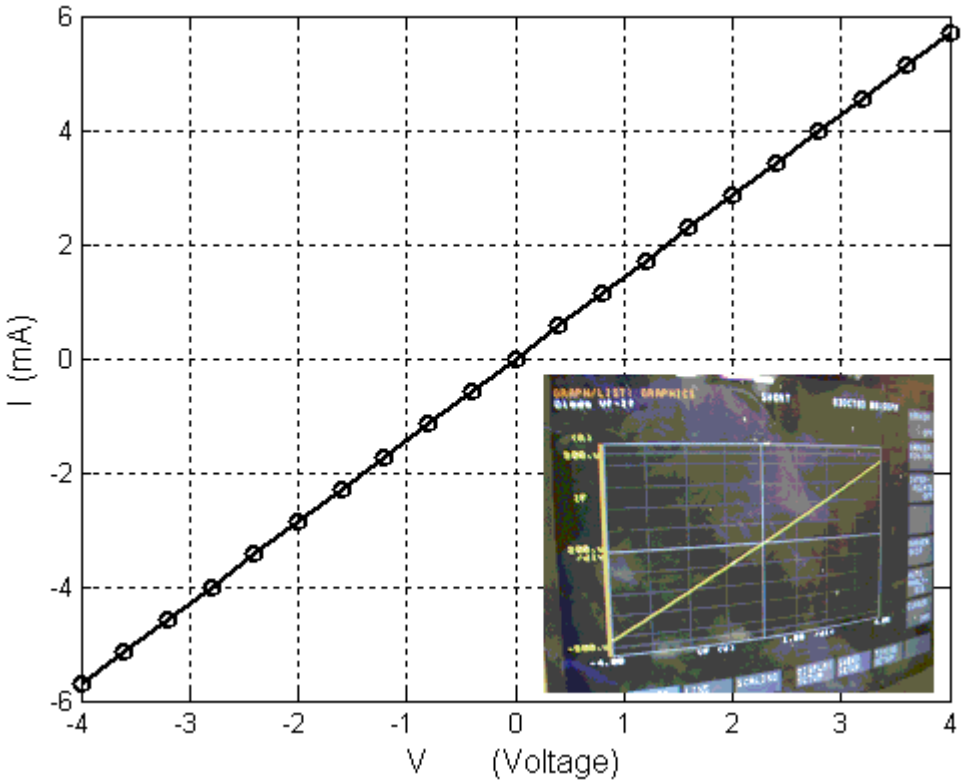

Fig 4. 8 I-V characteristic of piezoresistor after sintering process

4.1.6 Beam formation by D-RIE (Deep reactive ion etching)

To create deep, steep sided holes with high aspect ratios, we have to applied DRIE technology (see Fig 4. 9). It is a key process which was developed for MEMS. D-RIE is normally done using an inductively coupled plasma (ICP) reactor. Etching masks which can be used in D-RIE process are photoresists, silicon dioxide, or metals (aluminum or chromium). In our process, aluminum was selected to be etching mask because of its strong etching resistance. The detail process can be found in Ref [18].

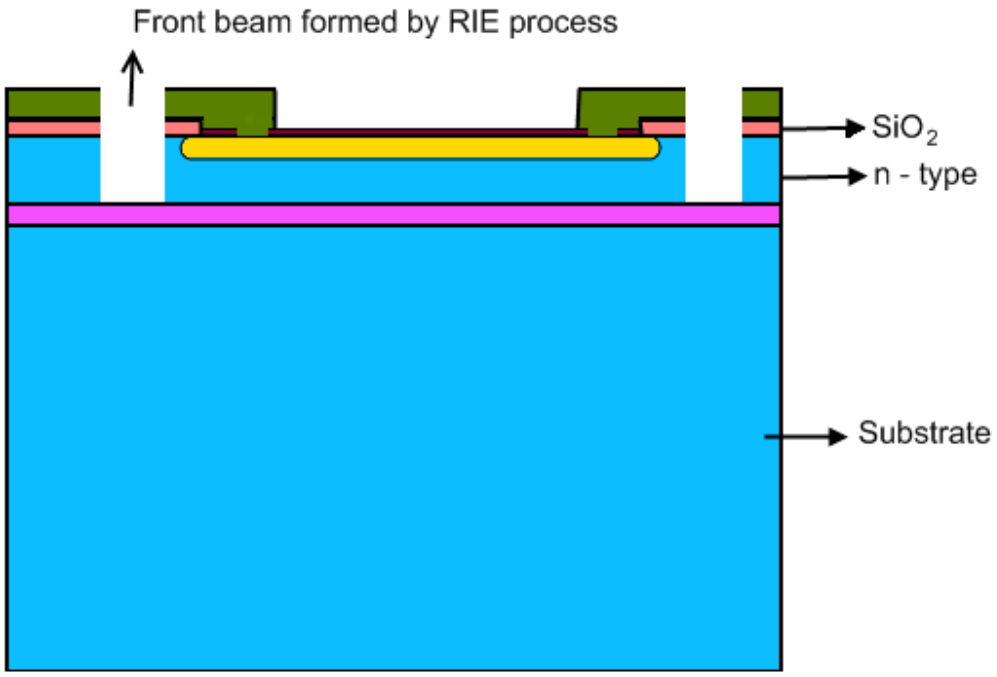

Fig 4. 9 The wafer after cross-beam forming

4.1.7 Backside mass gap formation

Backside mass gap was formed in order to protect sensor and control the air damping. The fabrication process is shown in Fig 4. 10.

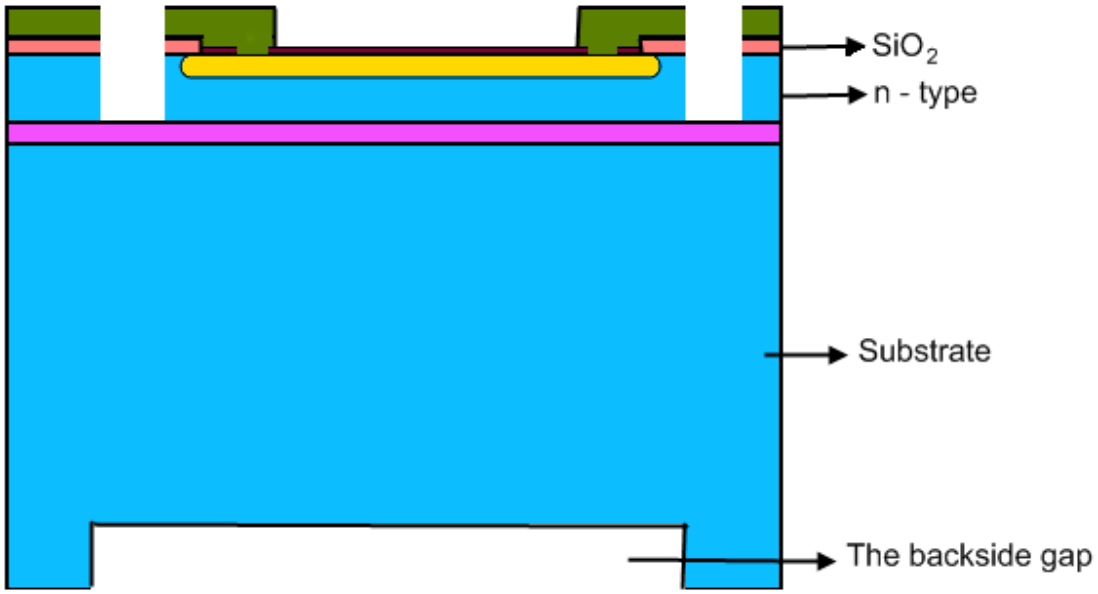

Fig 4. 10 The wafer after back-side mass forming

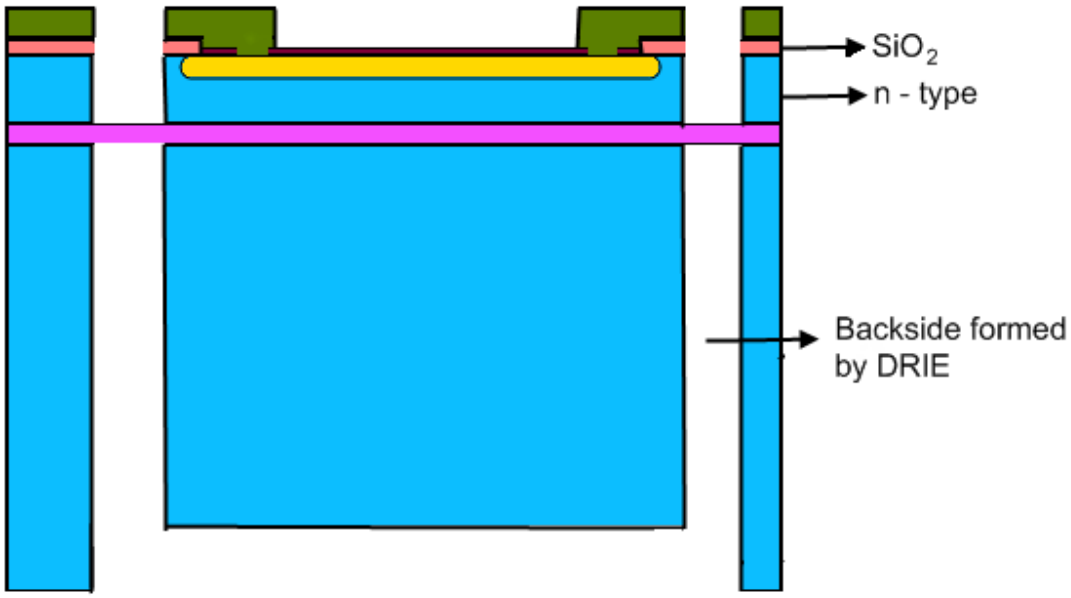

Fig 4. 11 The wafer after back-side etching

Fig 4. 12 and Fig 4. 13 show two corner views of a upper surface of a sensor. It is easy to see the unique between fabrication (left hand) and the L-EDIT design (right hand).

Fig 4. 14 is micrograph of a fabricated chip and Fig 4. 15 is the sensor after bonding.

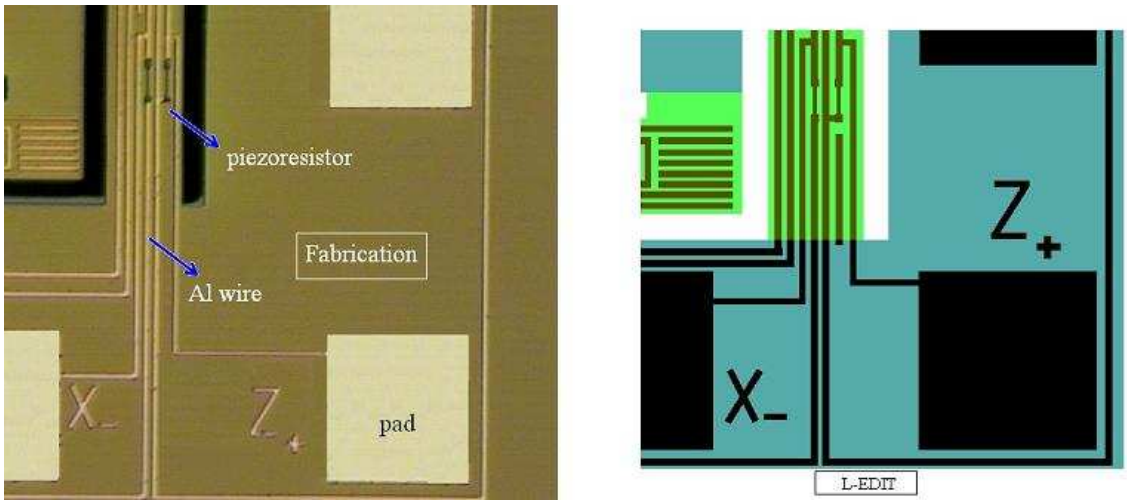

Fig 4. 12 The first quarter of the sensing chip

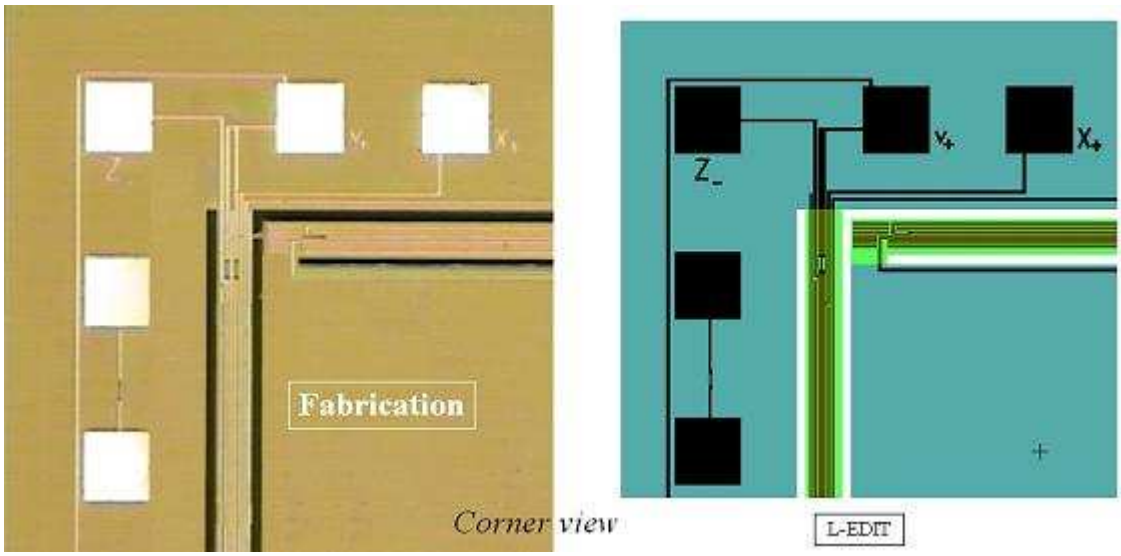

Fig 4. 13 The second quarter of the sensing chip

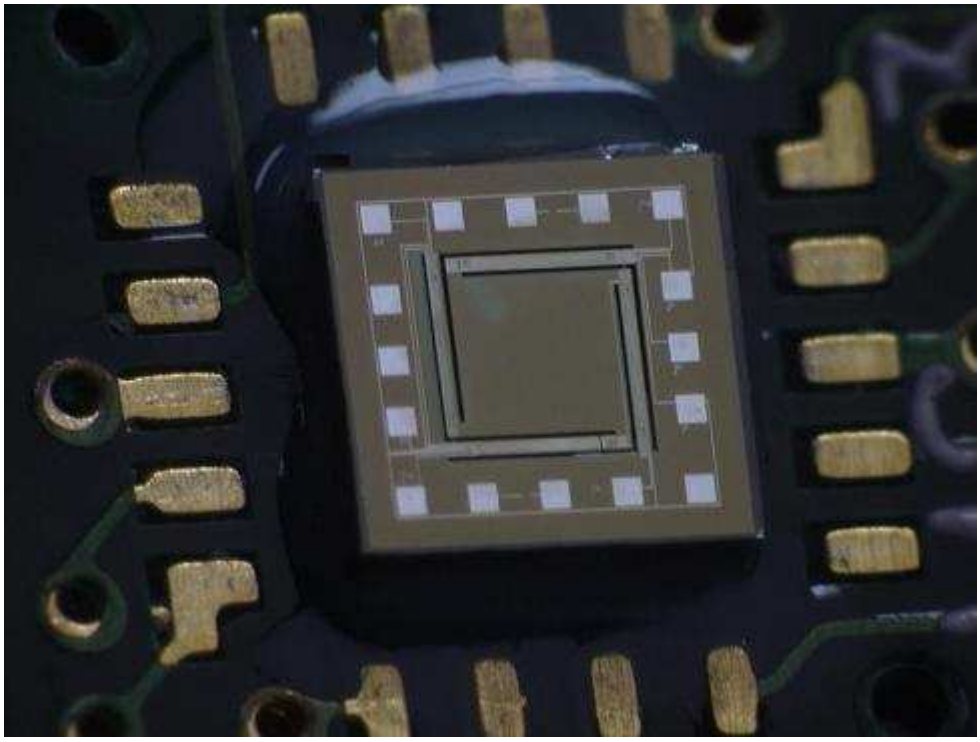

Fig 4. 14 The photo of the fabricated chip

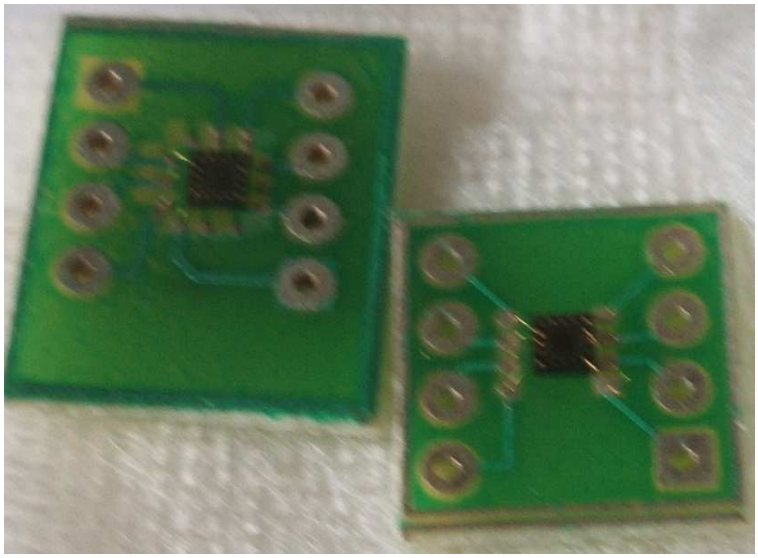

Fig 4. 15 The sensing chips after bonding

4.2 Measurement Results

Measurement and calibration after fabrication step play important role in order to both verify and further optimize the sensor design [70][31]. The fabrication of the acceleration sensor have been summarized in section 5.1. In this section, the calibration process have been carried out to confirm the characteristics of the sensor. After wire bonding, electronics connection between the accelerometer and the substrate was establish (see Fig 4. 15). To measure static and dynamic responses, the sensor was connect to a printed circuit board as show in Fig 4. 16.

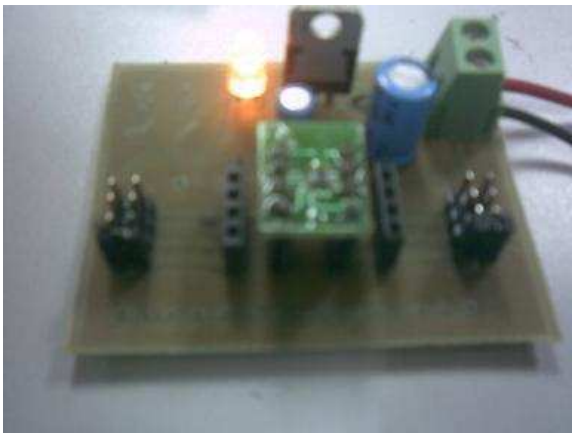

Fig 4. 16 Photo of the sensor assembled with PCB

4.2.1 Static measurement

To calibrate the acceleration AZ, the rotation disk was utilized to change the sensing acceleration from +g to –g (see Fig 4. 17). The static sensitivity of the fabricated sensor is characterized by rotating the accelerometer's sensitive axes around the earth's gravitational vector from 0^o to 180^o that correspond to the acceleration range of 2g (g=9.8 m/s^2). By normalizing the sensitivity at 1 g, the steady state response of the voltage is shown in Fig 4. 18.

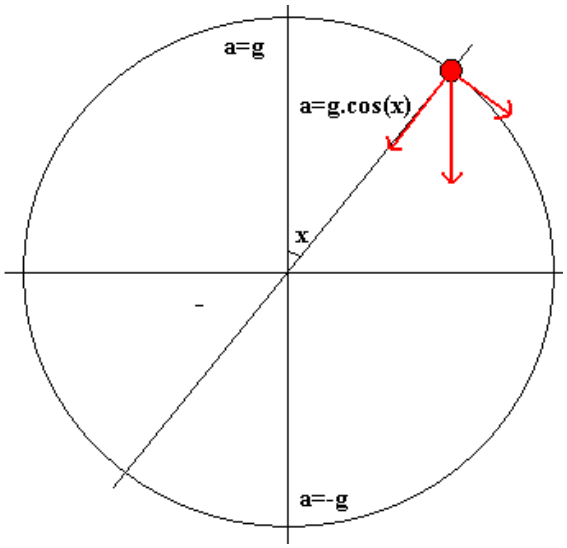

Fig 4. 17 Schematic view of AZ-calibration

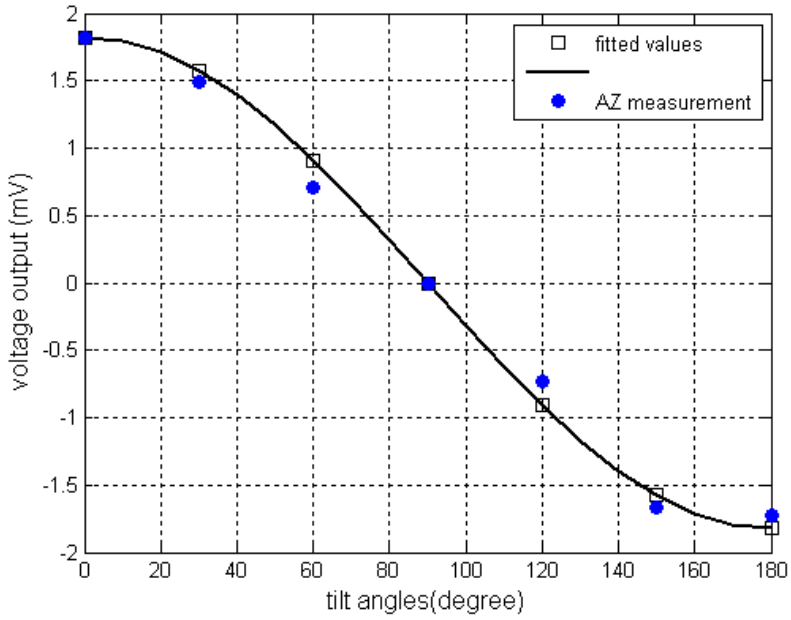

Fig 4. 18 The output response of the accelerometer vs. orientation to gravity

In order to determine the linearity of this sensor, we assume that the offset voltage is zero. Hence, the relationship between acceleration input and voltage output can be obtained as shown in Fig 4. 19.

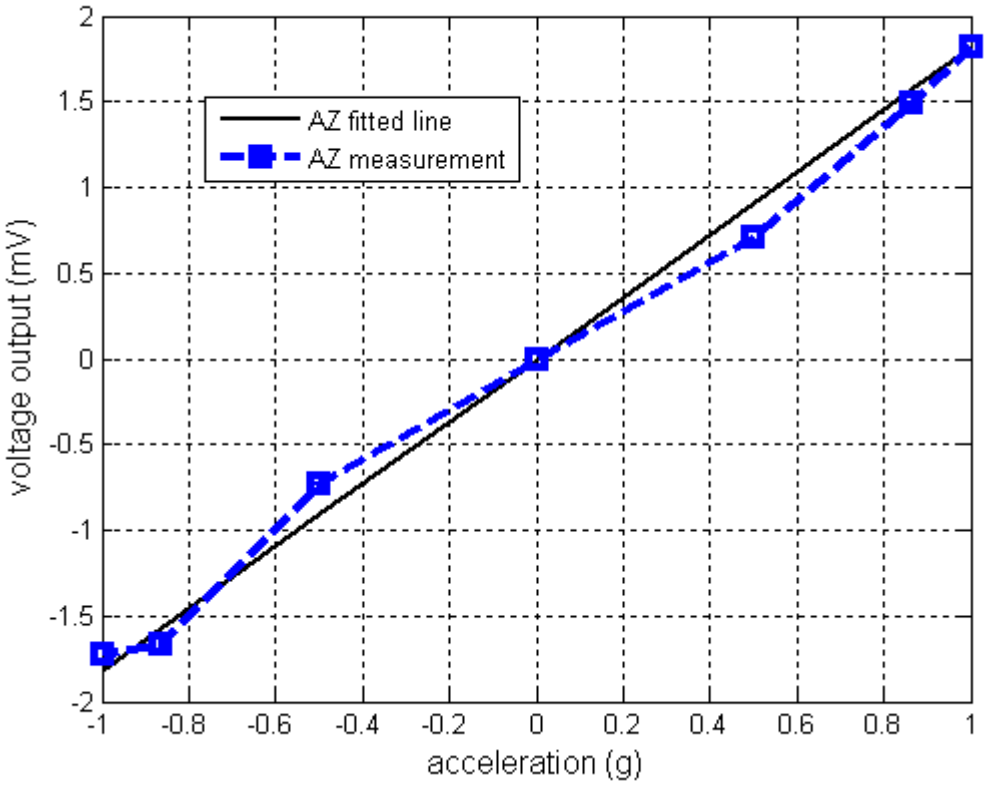

Fig 4. 19 The static response of the AZ oriented acceleration

Fig 4. 20 shows the output voltages of the sensing chip when the acceleration is increased from –g to +g. From this figure we can see that the experimental sensitivities are closed to simulated ones.

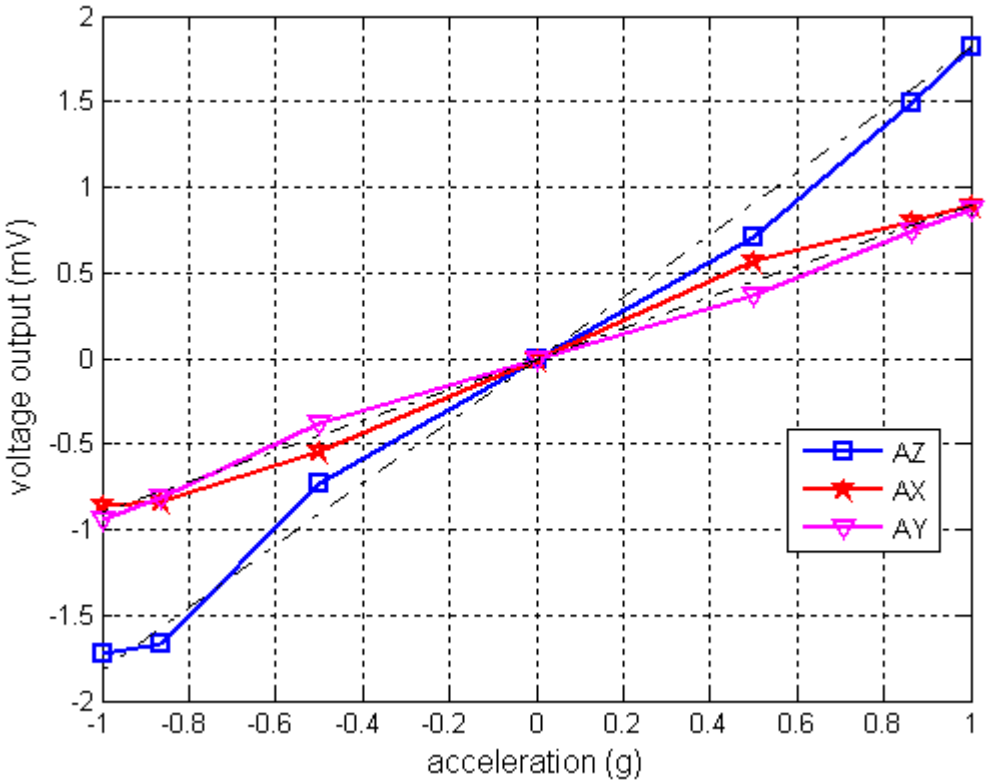

Fig 4. 20 Output voltages response to the simultaneous applications of three components Ax, Ay, and Az

4.2.2 Dynamic Responses

Fig 4. 21 is the schematic of vibration system which includes a function generator, a power amplifier, a shaker, a reference accelerometer (ADXL202), a fabricated sensor, and a data acquisition system. The acquisition system was developed by MEM & Microsystem Lab, COLTECH. There are two vibration measurements performed in this section: the first is applying a constant acceleration value at different frequencies; and the second is applying a changeable acceleration at a certain frequency.

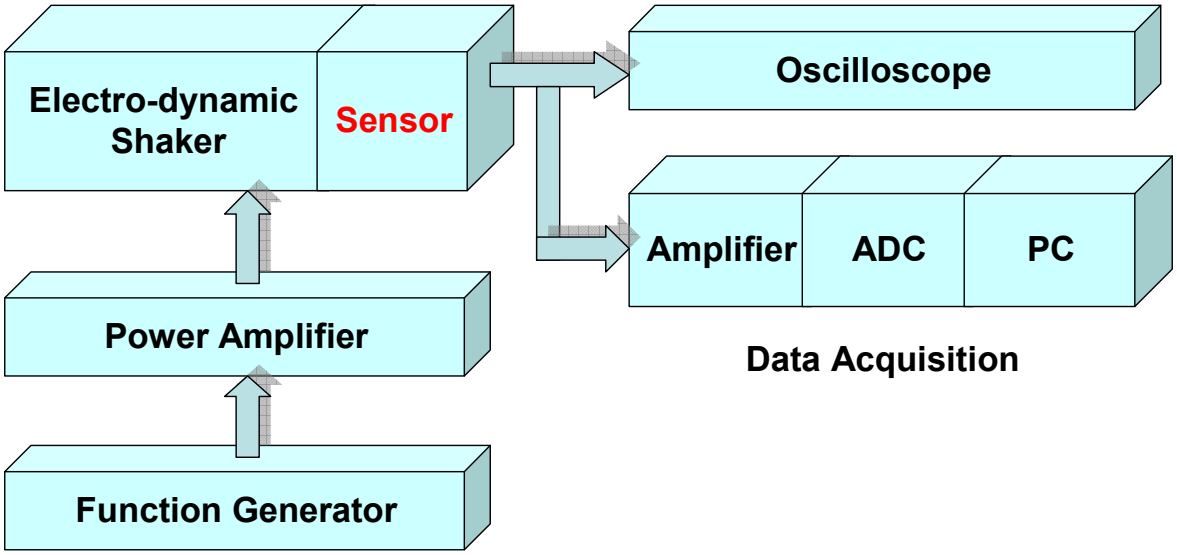

Fig 4. 21 Schematic of the vibratory system

The frequency responses of the system are shown in Fig 4. 21 and Fig 4. 23 with an acceleration of 5g. They can be understood as over-damped cases caused by effect of air damping of microstructures [81].

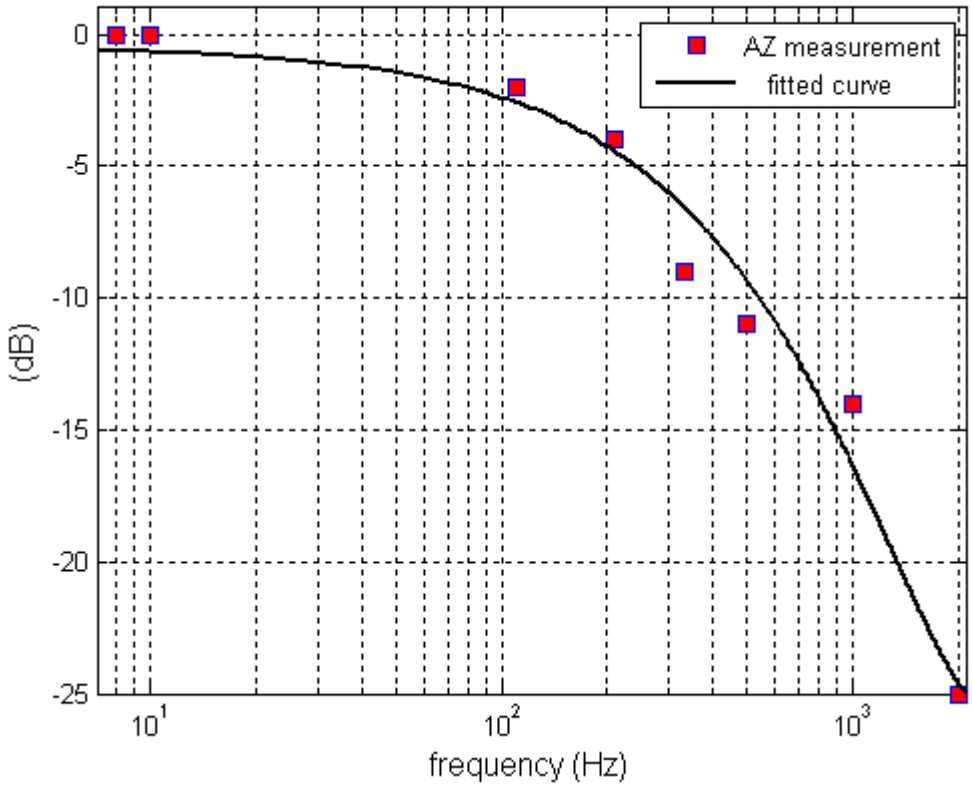

Fig 4. 22 Frequency response of the AZ oriented axis vibration

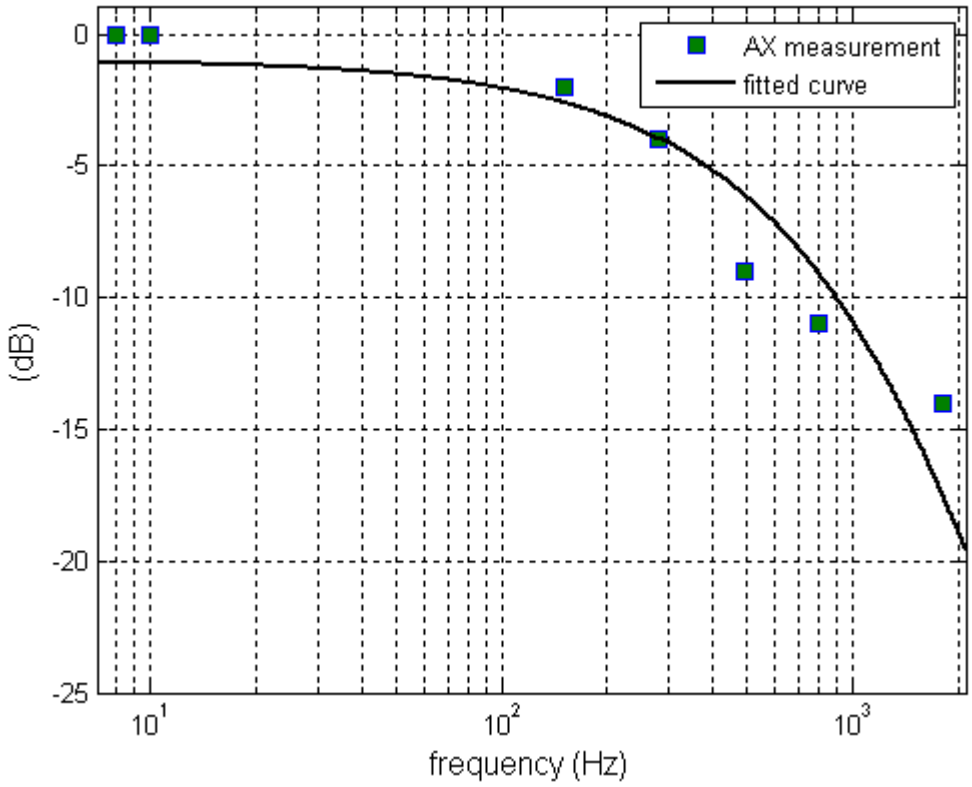

Fig 4. 23 Frequency response of the AX oriented axis vibration

To analyze the linearity of the sensor, the frequency is fixed at 20 Hz and the accelerations were changed from 0 to 5g. The sensing and crosstalk voltages are shown in Fig 4. 24. From this figure we can see that the cross-talk voltages between X-oriented and Y-oriented are much larger than other cross-talk components.

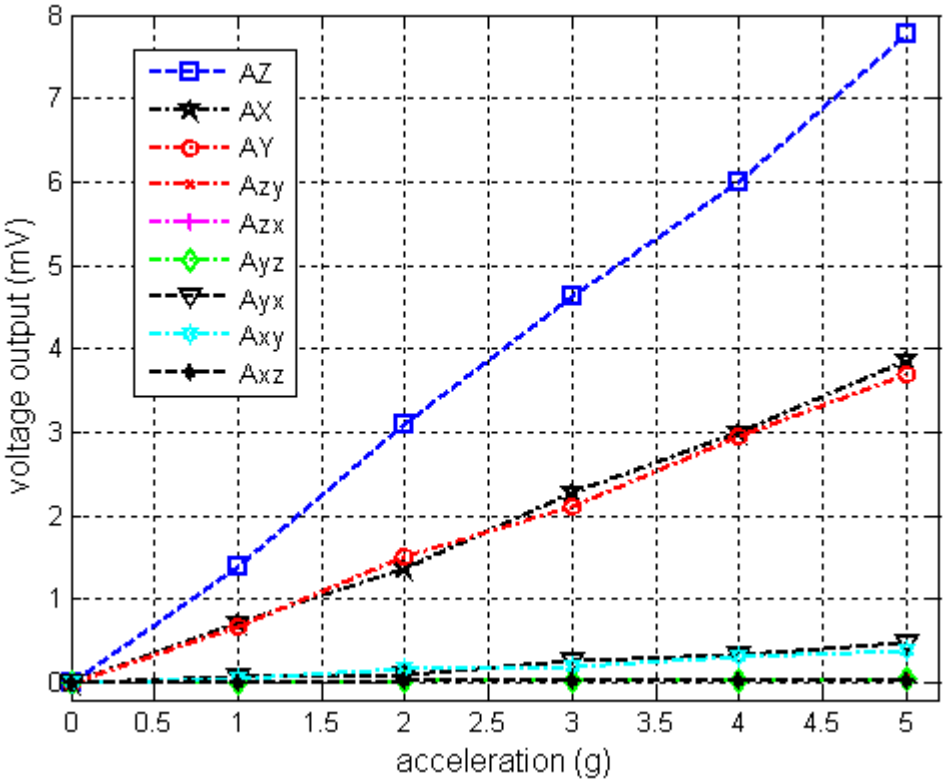

Fig 4. 24 The sensing and crosstalk voltages obtained from vibration system

4.2.3 Errors determination of the fabricated sensor

In order to bring the accelerometer to realistic applications, the errors determination is necessary. The key contributors to the electronic noise of this sensor are thermal noise and low frequency 1/f noise. Further more, in the interface circuit, an amplifier will contribute to the overall electronic noise of the measurement system. The errors can be classified into deterministic errors and stochastic errors. To eliminate the deterministic errors, we can specify them quantitatively by calibrating the device. For the stochastic errors, we have tried two different methods PSD and Allan variance. The PSD is known as a classical method to analyze signal, while Allan variance is a new method which can show more information than the PSD. Combining these two methods will give us a reliable noise model that is applied directly to the signal processing process [77].

The output data of the AZ-axis component collected during 20 minutes is shown Fig 4. 25. The sampling frequency here is 20 Hz which is suitable for the standing still status of the sensor.

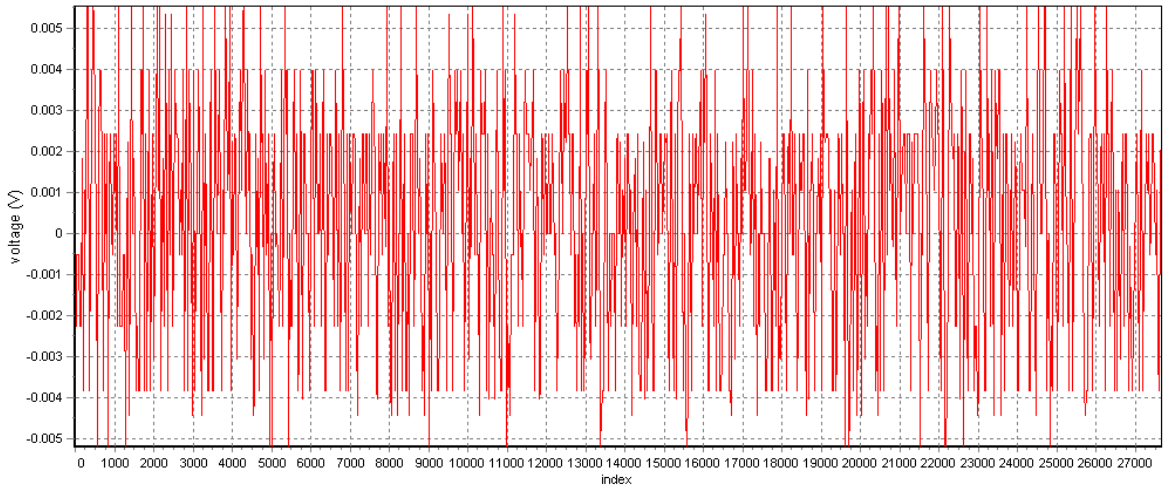

Fig 4. 25 The time plot of the AZ-oriented acceleration

4.2.3.1 Power spectral density analysis

The Power Spectral Density Analysis (PSD) describes how the power is allotted along the frequency axis [26]. Fig 4. 26 shows a log-log plot of the PSD of the Z-axis acceleration component. The slopes of the curve comprise 0 which means that there is only present of the white noise in Z-axis acceleration component.

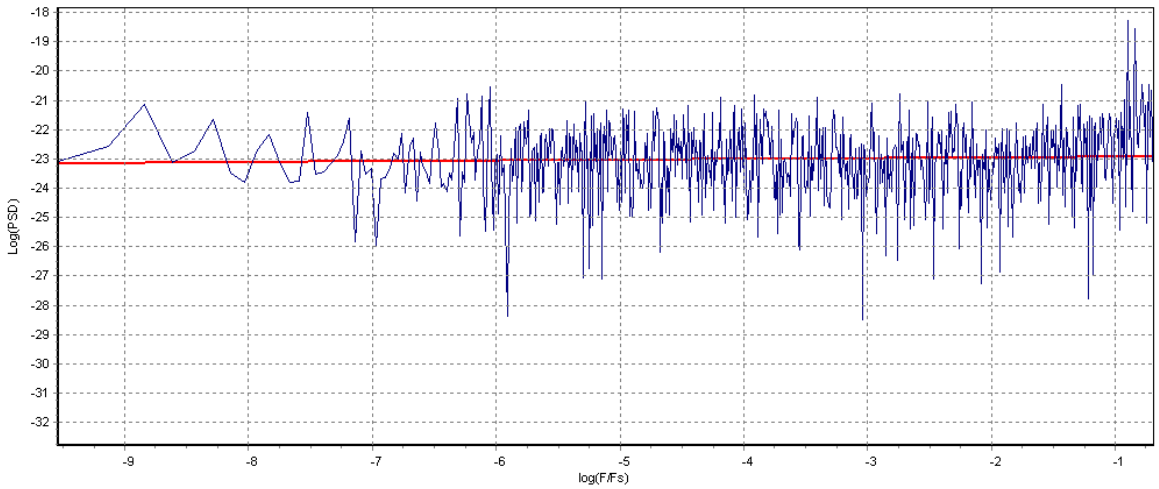

Fig 4. 26 The PSD plot of the AZ-axis acceleration component

4.2.3.2 Allan variance analysis

The Allan variance is statistical measure to characterize the stability of a time-frequency system [43]. The PSD can only extract white noise standard deviation. In contrast, using the Allan variance, several other error parameters can be comprehensively derived.

The basic idea of the Allan variance is to take a long data sequence and divide it into segments based on an averaging time τ to process. Let give a sequence with N elements y_k, k= 0,1,…, N-1. Then, we define for each n=1,2,3,...,M$\leq$N/2 a new sequence of averages of subsequence with length n:

$$x_j(n) = \frac{y_{nj} + y_{nj+1} + ... + y_{nj+n-1}}{n}, \qquad j = 0,1,...,\left[\frac{N}{n}\right] - 1 \tag{5.1}$$

If the sampling time is Δt, the time span within an averaged sequence of length n is $\tau = n\Delta t$. The Allan variance, for a given subsequence length n, is defined as:

$$\sigma_a^2(\tau, N) \overset{\Delta}{=} \frac{1}{2\left(\left[\frac{N}{n}\right] - 1\right)} \sum_{j=0}^{\left[\frac{N}{n}\right]-2} (x_{j+1}(n) - x_j(n))^2 \tag{5.2}$$

The typical slopes of the Allan variance for the AZ-oriented accelerometers in log-log plot are shown in Fig 4. 27 with data collected during 20 minutes. To determine the noise parameters, we need to fit the standard slopes in this figure. It is realized that the slope -1/2 appear in the log-log plot of the Allan standard deviation. Thus, the noise model in this acceleration component is very closed to white noise. This result is gain well consistent with that from the PSD plot.

Similar steps can be performed with the AX and AY acceleration components. The noise parameters of the 3-DOF accelerometer were summarized in Table 4. 1.

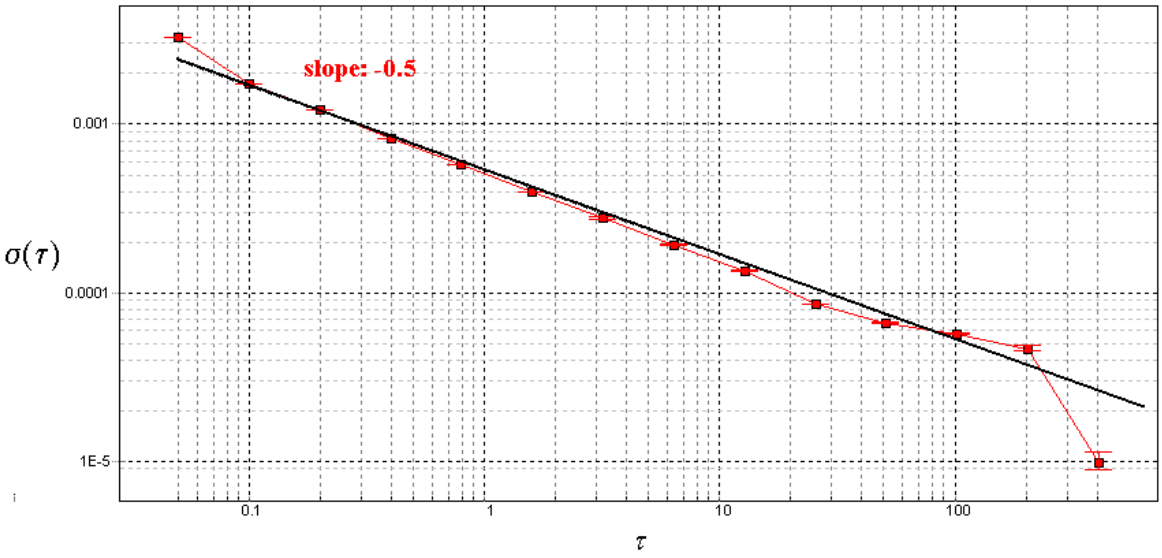

Fig 4. 27 The Allan standard deviation of AZ-oriented acceleration component

Table 4. 1 The comparison between the PSD and the Allan variance

	Accelerometers	
	PSD($[V\sqrt{s}]$)	Allan($V\sqrt{s}$)
X	$4.9*10^{-4}$	$5.3*10^{-4}$
Y	$9.5*10^{-3}$	$8.9*10^{-3}$
Z	$9.1*10^{-3}$	$9.3*10^{-3}$

4.2.4 Application to a Spectrum Analysis Application

One of the most accelerometer's applications is that using sensor for vibration analysis. In this section, the fabricated accelerometer was utilized to detect an unknown vibration signal from the shaker. The system was established as shown in Fig 4. 21 with the "unknown" signal is a 6-Hz sinuous signal. To detect the vibration signal, the FFT firstly was carried out in 15 minutes and the result was shown in Fig 4. 28. From this figure we can see that it is difficult to detect the vibration signal. Thus, the Welch method, a non-parametric utilized to improve estimation of power spectra. Fig 4. 29 show the good result when the 6-Hz signal is detected successfully. In the future, the latter version of this sensor may be applied to measure the heart motion as shown in [30].

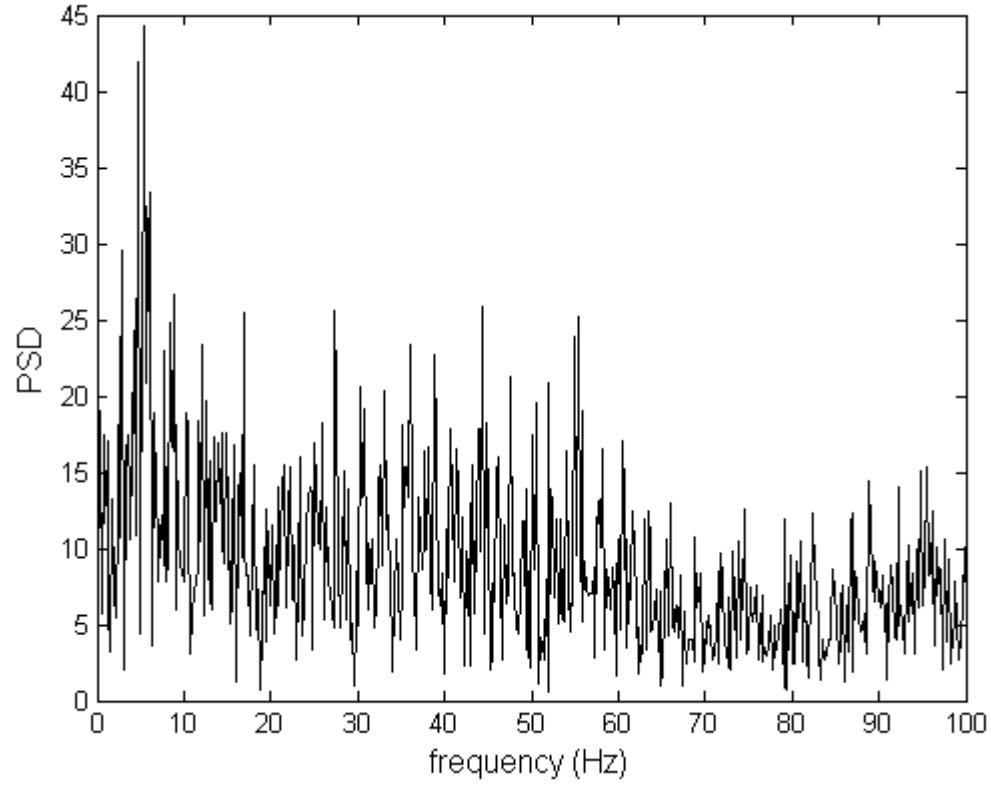

Fig 4. 28 The PSD of the unknown vibration

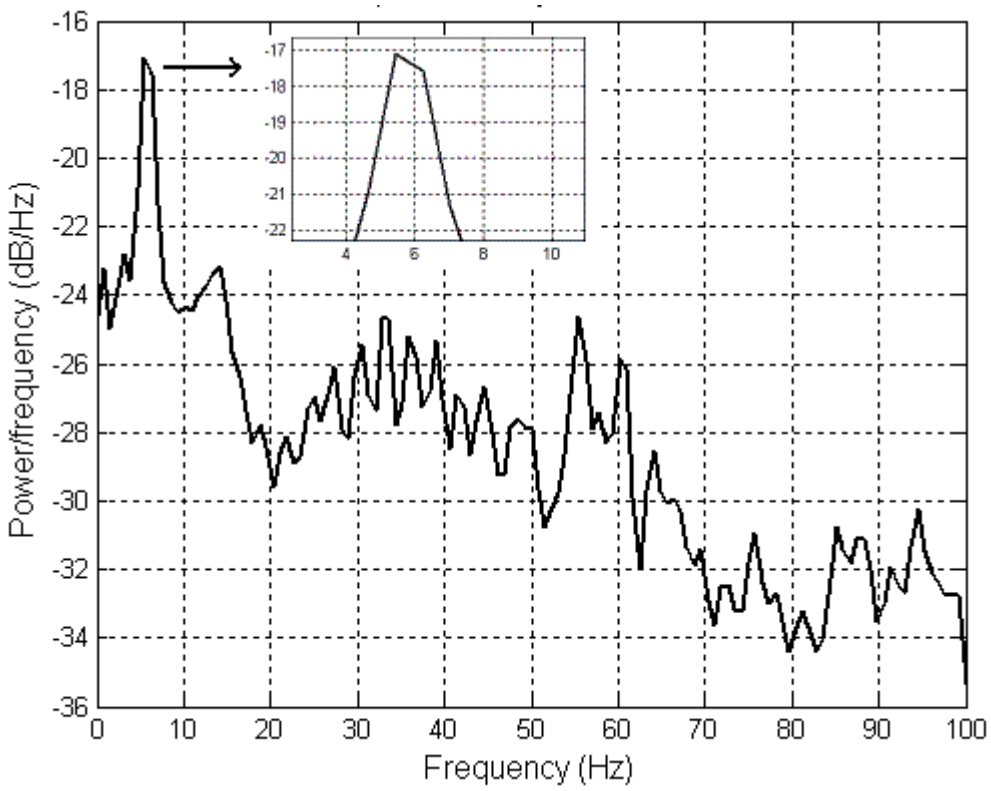

Fig 4. 29 The PSD of the signal obtained by Welch method

In general, the results measured in this chapter were rather closed to that of adjust simulations. The differences between experiment and design may be caused by misalignment during set-up procedure, slight unmatched conditions with the conditions in the fabrication and simulation. Experimental results show that the sensor can be applied directly to several applications such as 3-D inclination or vibration measurements.

4.3 Summary

The accelerometer has been fabricated successfully due to the support of MiNiDel lab. The sensing chip was fabricated by micromachining process where the starting material is a SOI wafer. Thermal diffusion is performed to define p-type Si, EB lithography and RIE to create piezoresistors, metallization process to make interconnection, and DRIE to form the beam and proof mass.

The static and dynamic responses of the fabricated sensor are presented in this chapter. Two initial results on application of the sensor to declination and vibration systems are also investigated. Further more, the PSD and Allan Variance methods were utilized to determine the noises from the sensor and interface circuit.

CHAPTER 5

OPTIMIZATION BASED ON FABRICATED SENSOR

5.1 Introductions

From the results of previous chapter, the proposed problem is that it is better to exam the quality of the fabricated sensor. Consequently, the optimization target based on this structure is needed to compare with the measured results. Furthermore, the optimum procedure can be simply applied to next generation of sensor's structures. The optimization problem here is formulated in terms of objective functions based on three performance parameters: sensitivity, noise, and resolution. The multi objective optimization is also called Pareto optimization [25] in which the complexity may be triple when we have to consider to three components of acceleration concurrently. The purpose of this process is to achieve the high sensitivity or resolution [15][47][73]. It has been done based on considerations of junction depth, the doping concentration of the piezoresistor, the temperature, the noise, and the power consumption. The result shows that the sensitivity of the optimized accelerometer is improved while the resolution is small compared to previous experimental results.

5.2 Pareto Optimality Processes

The electronic sensitivity of the piezoresistive accelerometer is defined as the ratio of its electronic output and to it acceleration input slope of the calibration curve relating the output with zero offset voltage:

$$S_i = \frac{V_{out}}{a} \qquad i = X, Y, Z \tag{5.1}$$

Substitute from (3.7) to (3.5), we obtain:

$$S_i = \frac{1}{a}\frac{\Delta R}{R} V_{in}^i \qquad i = X, Y, Z \tag{5.2}$$

or

$$S_i \approx \frac{1}{a}\pi_l^i \sigma_l^i V_{in}^i \qquad i = X,Y,Z \tag{5.3}$$

Due to the second sub-function, the value of π_l also depends on the temperature T and the impurity concentration N. Further more, the value of σ_l depends on the sensor structure. In other word, this value depends on resonant frequency. For these reasons, the sensitivity depends on many parameters such as resonant frequency, impurity concentration, temperature, piezoresistor dimensions, and power consumption.

The key contributors to the electronic noise of the piezoresistor are thermal noise and low frequency 1/f noise. Thus, resolution defined as the noise divided by the sensitivity can be expressed as:

$$R_i = \frac{V_i^{noise}}{S_i} \qquad i = X,Y,Z \tag{5.4}$$

or

$$R_i = \frac{2\sqrt{\left(V_i^{Johnson,rms}\right)^2 + \left(V_i^{1/f}\right)^2}}{\frac{1}{a}\pi_l^i \sigma_l^i V_{in}^i} \qquad i = X,Y,Z \tag{5.5}$$

Fig 5. 1 shows the flowchart of the sensitivity/resolution optimization process. This process is performed by programming in MATLAB environment. An important constraint imposed in the optimization process is the power consumption. In various kinds of application such as structure health monitoring or patient monitoring that using wireless sensor, low power requirements are in great need [29][42].

At specific power consumption of a full bridge Wheatstone circuit, we have got series of input voltages, noises, sensitivities, and resolutions varied by a set of constraint parameters listed in Table 5. 1. Note that the cross-sectional area of piezoresistor is fixed to 2μm×1.5μm (W×T) and structure parameters of the accelerometer were mentioned in Table 3. 2.

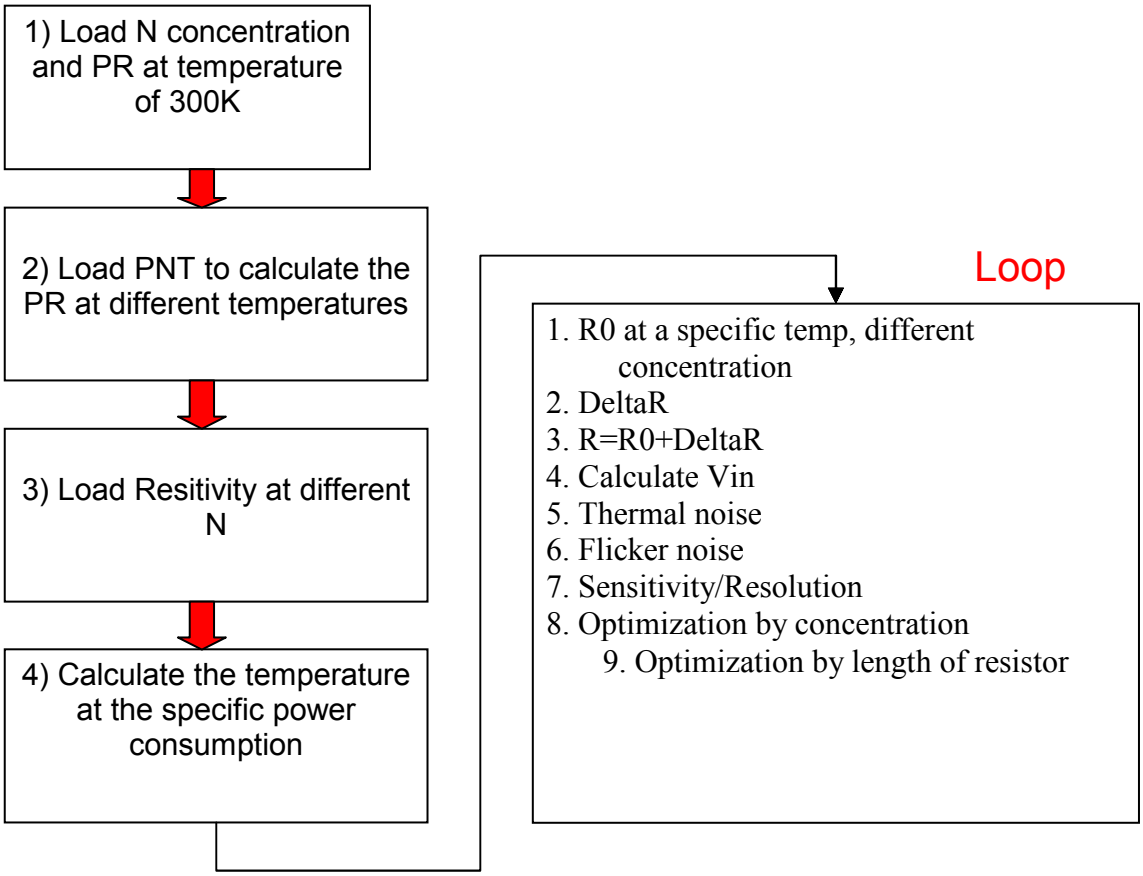

Fig 5. 1 Flowchart of the sensitivity/resolution optimization process.

Table 5. 1 Parameter constraints for optimization process

Parameter	Value	
	Min	Max
Length of piezoresistor *L*	6 μm	30 μm
Diffused concentration *N*	$1.26*10^{17}$ atoms cm^{-3}	$3*10^{20}$ atoms cm^{-3}
Input voltage V_{in}	1 V	6 V

It seeks to provide the best compromise among objectives. Different optimal designs are found for which one objective can not be improved without degradation in one of the other objectives [8],[24]. In the hyperspace of the Pareto front, there is no point that provides an improvement compared to any other with respect to both the sensitivity and the minimum detectable acceleration (resolution). Thus, we have got two approaches: maximizing the sensitivity and minimizing the noise (i.e. best resolution).

5.2.1 Sensitivity Optimization

At specific power consumption, the mathematical representation of the optimization problem is the maximization of three objective functions $S_i(x)$ denoted as:

$$S_i^{\max}(x) = \underset{x=L,N,T,Vin}{Maximize} \quad S_i(x) \qquad i = X,Y,Z \tag{5.6}$$

or

$$S_i^{\max}(x) = \frac{1}{a}.\underset{x=L,N,T,Vin}{Maximize} \quad \pi_l^i \sigma_l^i V_{in}^i \qquad i = X,Y,Z \tag{5.7}$$

The sensitivity varies significantly with the beam length. The piezoresistive effect on each piezoresistor is determined through the average value of stress. However, changing the length of piezoresistor from 6 μm to 30 μm does not affect this average value of stress. From results of the chapter 3, the value of σ_l^i can be fixed when the geometric structure is specific (see Table 3. 2). Thus, the equation (5.9) can be rewritten as:

$$S_i^{\max}(x) = \frac{1}{a}\sigma_l^i.\underset{x=L,N,T,Vin}{Maximize} \quad \pi_l^i V_{in}^i \qquad i = X,Y,Z \tag{5.8}$$

It is also observed that the sensitivity decrease monotonically with the impurity concentration. With a constant power, the high input voltage in company with high resistance value of piezoresistors is needed to increase the sensitivity. For these results, the solution to maximize three sensitivities (Sx, Sy, Sz) concurrently can be converge to an unique set of results (see Fig 5. 2).

For the AZ acceleration component at a specific power consumption of 7.7 mW, we found that the optimum length of piezoresistors and doping concentration are of 30 μm and 1.26×10^{17} atoms cm^{-3}, respectively. Concentration below 10^{17} atoms cm^{-3} is not practical due to instable Ohmic contact. The optimal sensitivity we can achieve is 1.91 mV/g (i.e. 0.37 mV/V/g). At this point, the resolution is 0.53 mg, the resistance of piezoresistor is 3.5 kΩ, the input voltage is 5.1 V, and the temperature is 305 K.

For the AX or AY acceleration component, we also found that the optimum length of piezoresistors and doping concentration are of 30 μm and 1.26×10^{17} atoms cm^{-3}, respectively. The optimal sensitivity we can achieve is 0.89 mV/g (i.e. 0.17

mV/V/g). At this point, the resolution is 1.27 mg, the resistance of piezoresistor is 3.5 kΩ, the input voltage is 5.1 V, and the temperature is 305 K.

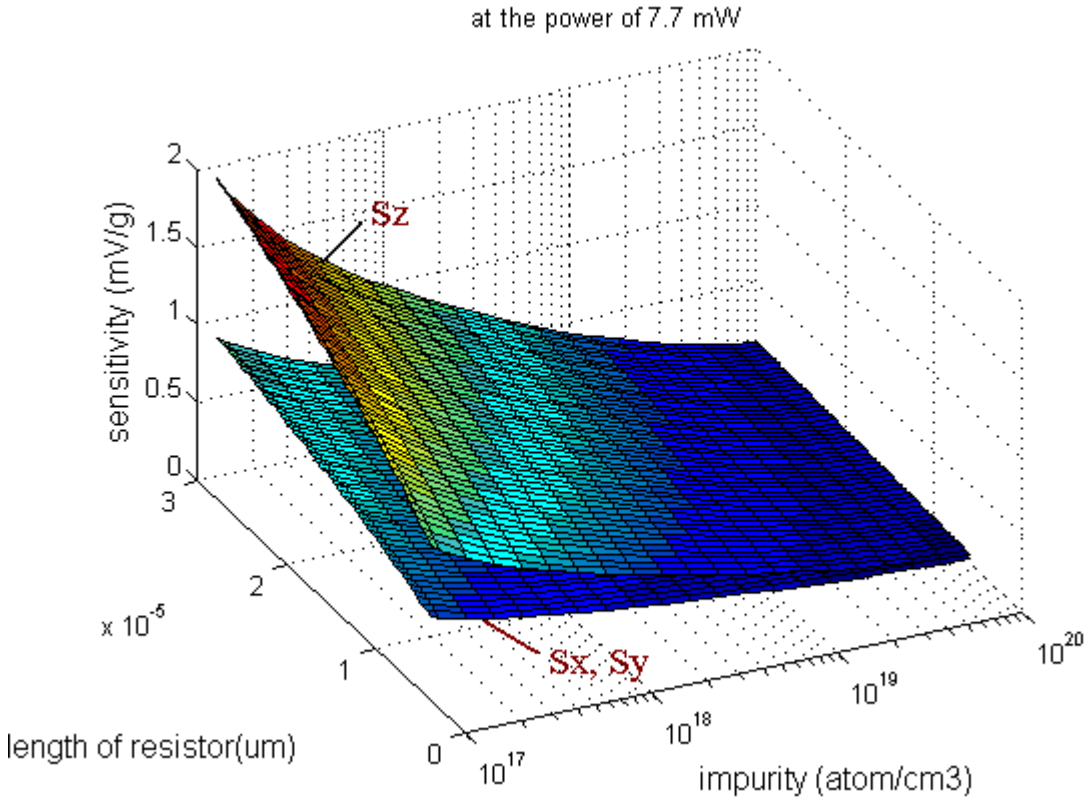

Fig 5. 2 Variation of sensitivity for different piezoresistor lengths and doping concentrations

Fig. 5.3 shows the variation of sensitivities of the acceleration components with length of piezoresistor for different power consumptions. Obviously, at the higher power, we can obtain the higher the sensitivity despite of higher noises.

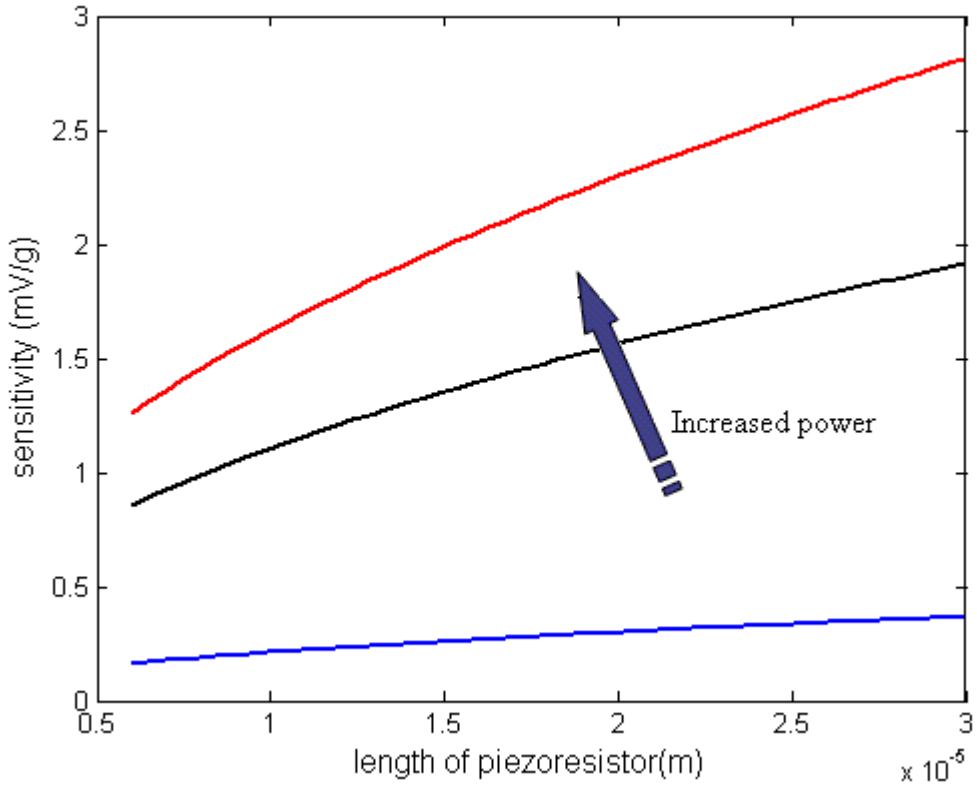

Fig 5. 3 Variation of sensitivity for different power consumptions

5.2.2 Resolution Optimization

Resolution is defined as the noise divided by the sensitivity. It defines the lower end of the dynamic range which piezoresistive accelerometer can resolve in the presence of noise. The optimization problem is formulated in terms of objective functions based on performance parameters: sensitivity, noise, and resolution.

It is observed that optimization of the resolution has been achieved by increasing the sensitivity and reducing the noise [78]. The noises depend on the bandwidth of sensor, the temperature, the geometry of piezoresistor, the doping concentration and also the thickness of the beam.

The mathematical representation of the optimization problem is the minimization of three objective functions $R_i(x)$ denoted as:

$$R_i^{\min} = \underset{x=L,N,T,Vin}{Minimize} \; R_i(x) \qquad i = X,Y,Z \tag{5.9}$$

or

$$R_i^{\min} = \frac{2a}{\sigma_l^i} \underset{x=L,N,T,Vin}{Minimize} \frac{\sqrt{\left(V_i^{Johnson,rms}\right)^2 + \left(V_i^{1/f}\right)^2}}{\pi_l^i V_{in}^i} \qquad i = X,Y,Z \tag{5.10}$$

Substitute equations (3.20) and (3.21) to (5.12), we obtain:

$$R_i^{\min} = \frac{2a}{\sigma_l^i} \underset{x=L,N,T,Vin}{Minimize} \frac{\sqrt{4k_B T B_i R + \frac{\alpha V_{in}^2}{N} \ln\left(\frac{f_{\max}^i}{f_{\min}^i}\right)}}{\pi_l^i V_{in}^i} \qquad i = X,Y,Z \tag{5.11}$$

where $B_i = f_{\max}^i - f_{\min}^i$

From the equation (5.11) we can see that if we chose a unique bandwidth for three acceleration components (by using low-pass filters) we can get the same solution for three resolutions (Rx, Ry, Rz) concurrently (see Fig 5. 4).

The flowchart of the optimization is also shown in Fig 5. 1. The optimization problem can be implemented in MATLAB environment using the *fmincon* function that utilize sequential quadratic programming for nonlinear constrained problems and calculating the gradients by finite difference method. The details solution can be summarized as following:

For the AZ acceleration component at a specific power consumption of 7.7 mW, the optimal resolution we can achieve is 0.33 mg. At this point, impurity concentration is 4.47×10^{18} atoms cm^{-3}, the sensitivity is 0.61 mV/g (i.e. 0.36 mV/V/g), the resistance of piezoresistor is 370 Ω, the input voltage is 1.7 V, and the temperature is 305 K, respectively.

For the AX or AY acceleration component, the optimal resolution we can achieve is 0.86 mg at impurity concentration of 4.47×10^{18} atoms cm^{-3}. At this point, the sensitivity is 0.28 mV/g (i.e. 0.17 mV/V/g), the resistance of piezoresistor is 370 Ω, the input voltage is 1.7 V, and the temperature is 305 K, respectively.

The variation of the resolution of three acceleration components with specific power consumption of 7.7mW for different doping concentrations and different piezoresistor lengths is shown in Fig 5. 4. Unlike the sensitivity, the optimum resolution is achieved with a different impurity concentration. This is because the optimal values are achieved by the compromise among different parameters. The optimal resolutions for all three acceleration components can be reached at the

piezoresistor length of 30 μm, the doping concentration of 4.47×10^{18} atoms cm^{-3}, and the input voltage of 1.7 V.

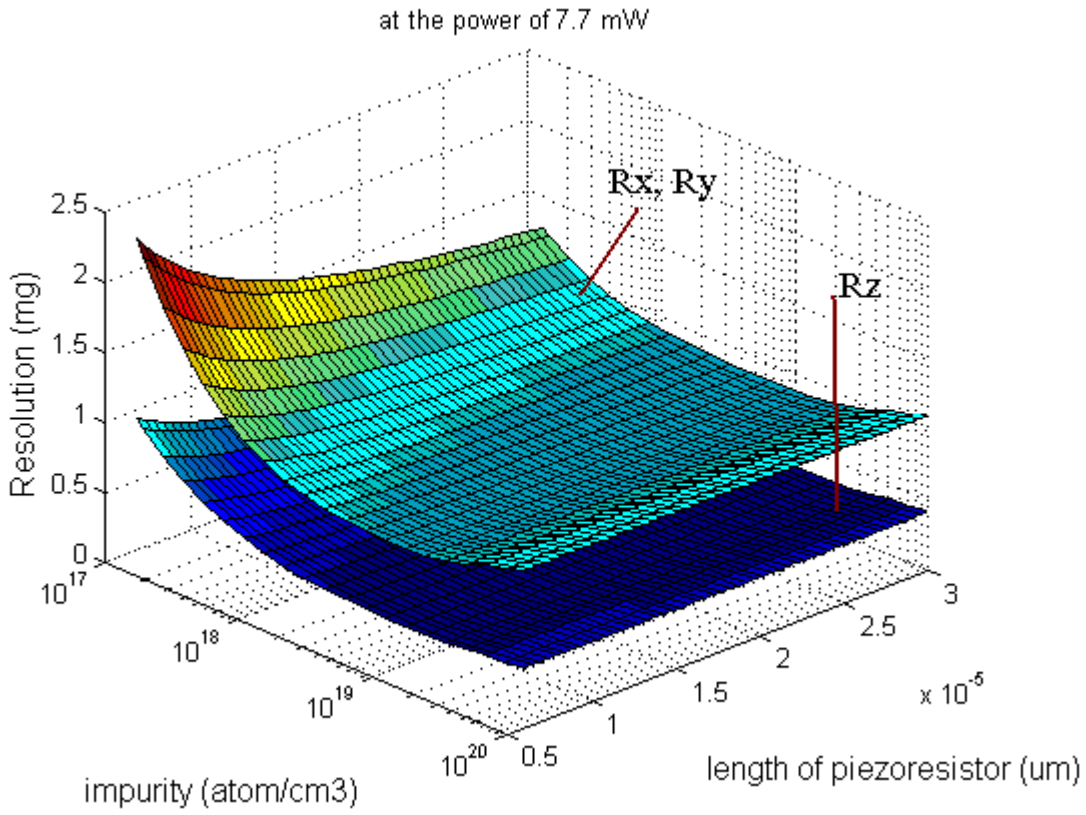

Fig 5. 4 Variation of resolution for different piezoresistor lengths and doping concentrations

From these results above, a trade-off between high sensitivity and high resolution is necessary to decide the doping concentration in the range from 1.26×10^{17} atoms.cm^{-3} to 4.47×10^{18} atoms.cm^{-3}.

Fig 5. 5 shows the variation of resolution with length of piezoresistor for different power consumptions. Obviously, at the higher power, we can obtain the better the resolution despite of higher noises.

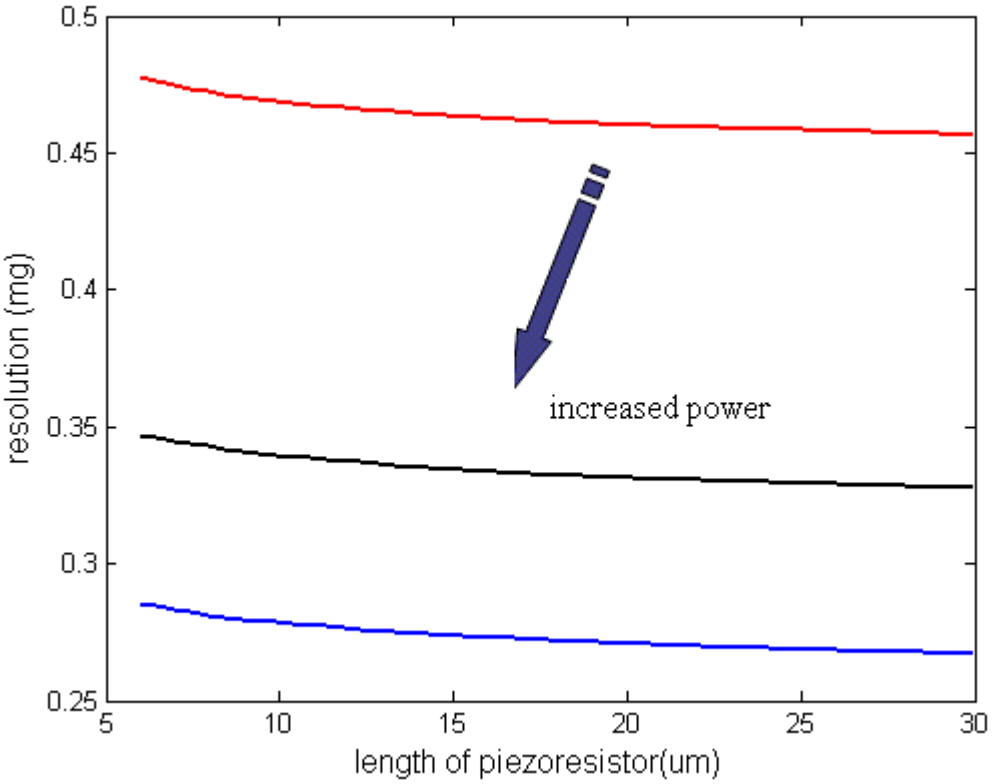

Fig 5. 5 The dependence of resolution on length of the piezoresistor at different power consumptions.

The optimization was applied to an available structure of acceleration sensor fabricated by micromachining process. Fig 5. 6 shows for comparison the expected result of our propose design and the testing in the previous result of the AZ acceleration component. Obviously, the new design gives higher sensitivity at lower power. Work on the fabrication of this optimized accelerometer is in progress.

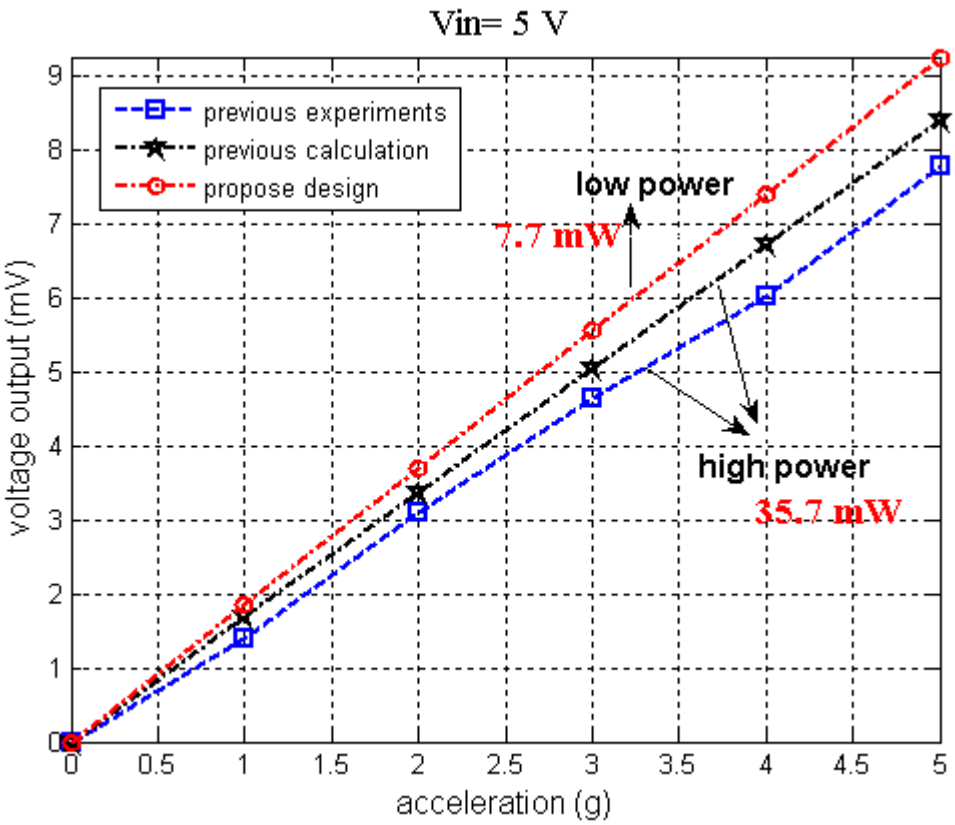

Fig 5. 6 Comparisons among previous experiment, previous calculation, and new proposed design

5.3 Summary

This chapter has been successful in optimization of the 3-DOF accelerometer with two performance parameters: sensitivity and resolution. The complexity was triple reduced by utilizing the frequency constraint. Two Pareto optimization procedures of sensitivity maximization and resolution minimizing were implemented in MATLAB environment with the considerable concern of piezoresistors' dimensions, the doping concentration of the piezoresistor, the temperature, the noise, and the power consumption.

CONCLUSIONS

In this thesis, the comprehensive research on silicon 3-DOF accelerometer utilizing MEMS technology has been presented.

One of the important contributions of this thesis is that a hierarchical MEMS design synthesis and optimization process have been developed for and validated by the design of a specific structure of MEMS based accelerometer. The iterative synthesis design is largely based on the use of a MNA tool called SUGAR in order to meet multiple design specifications. After some human interactions, the design is brought to FEM software such as ANSYS for final validation and further optimization. The optimal configuration was reached by exploiting the advantages of both types of simulations.

The positions of the piezoresistors have been found based on the stress distribution obtained by structural analysis. Three Wheatstone bridges have been formed by twelve piezoresistors in order to meet the requirements of maximizing the sensing sensitivities and minimizing the cross-axis sensitivities. The coupling simulation for thermal – mechanical – piezoresistive fields is extremely necessary to evaluate the sensor characteristics. The results are very helpful to further improve or optimize the performance of the sensor.

After the mask design and fabrication processes, sensors have been calibrated by static and dynamic measurements while both of the intrinsic sensor's noises and the interface circuit's noise could be determined by PSD and Allan variance methods.

The thesis was also successful in implementing of the optimization of high performance multi-degree of freedom silicon accelerometer. The purpose of this optimization is to achieve the high sensitivity or resolution. The optimization has been performed based on considerations of junction depth, the doping concentration of the piezoresistor, the temperature, the noise, and the power consumption. The result shows that the sensitivity of the optimized accelerometer is improved while the resolution is small compared to previous experimental results.

Work in the future will continue on optimizing the sensor performances and developing of effective temperature compensation. We expect that these contributions will be brought to commercialization soon.

REFERENCES

[1] Bechtold T., Rudnyi E.B., Korvink J.G., (2007), "Fast Simulation of Electro-Thermal MEMS: Efficient Dynamic Compact Models", *Springer*.

[2] Bouten C.V.C., Koekkoek K.T.M., Verduin M., Kodde R., Janssen J.D., (1997), "A triaxial accelerometer and portable data processing unit for theassessment of daily physical activity", *IEEE Transactions on Biomedical Engineering* Vol. 44(3), pp.136 – 147.

[3] B. Van Zeghbroeck, (2007), Principles of semiconductor devices, http://ece-www.colorado.edu/~bart/book.

[4] C Pramanik, H Saha and U Gangopadhyay, (2006), "Design optimization of a high performance silicon MEMS piezoresistive pressure sensor for biomedical applications", *J. Micromech. Microeng.* 16, pp. 2060-2066.

[5] Cimoo Song, (1997), *Commercial vision of silicon based inertial sensors*, TRANSDUCERS'97 Vol.2, Chicago, pp.839 - 842 vol.2

[6] Chiou J.A., Chen S., (2005), "Thermal Hysteresis Analysis of MEMS Pressure Sensors", *Journal of Microelectromechanical Systems* Vol.14(4), pp. 782 – 787.

[7] Cornelius T. Leondes el at, (2006), "MEMS/NEMS Handbook Techniques and Applications", *Springer Press*.

[8] Corley H, (1981), "A fixed point interpretation of Pareto optimization", *IEEE Transactions on Automatic Control* Vol.26(3), pp.766 – 767.

[9] Clark J.V., Bindel D., Kao W., Zhu E., Kuo A., Zhou N., Nie J., Demmel J., Bai Z., Govindjee S., Pister K.S.J., Gu M., Agogino A., (2002), *Addressing the needs of complex MEMS design*, The Fifteenth IEEE International Conference on Micro Electro Mechanical Systems, Las Vegas, NV, USA, pp. 204 – 209.

[10] Dale F.O. and M. Gyimesi, (2000), *Finite Element Based Reduced Order Modeling of Micro Electro Mechanical Systems (MEMS)*, MSM2000,USA.

[11] Danny Banks, (2006), "Microengineering, MEMS, and Interfacing: A Practical Guide", *CRC Press*.

[12] Djambazian H.H., Nerguizian C., Nerguizian V., Saad M., (2006), *3D Inclinometer and MEMS Acceleration Sensors*, IEEE International Symposium on Industrial Electronics, Canada, pp. 3338-3342.

[13] Dong Yiqun, Zhang Wuming, Liu Jiliang, Cheng Yuquan, (1995), *Mathematical model and heat conduction analysis of a silicon-basedthermoelectric enzyme sensor*, TENCON'95, pp. 367 – 370.

[14] Dragunov V.P., Shishkov A.A., (2002), *Modeling of the piezoresistance effect nonlinearity in p-Si*, The 6th Russian-Korean International Symposium on Science and Technology KORUS-2002, pp. 271- 274.

[15] Dumbravescu, N., Enescu, A., (2003), *Enhancements in design and technology applied to a high sensitivity piezoresistive accelerometer*, International Semiconductor Conference CAS 2003., pp. 205-208.

[16] Dzung Viet Dao, Toriyama T., Sugiyama S., (2004), *Noise and Frequency Analyses of a Miniaturized 3-DOF Accelerometer Utilizing Silicon Nanowire Piezoresistors*, Proceedings of IEEE Sensors, vol.3, pp. 1464- 1467.

[17] Dzung Viet Dao, Van Dau T., Hayashida M., Dinh T.X., Shiozawa T., Sugiyama S., (2006), *Fabrication and Characterization of 2-DOF Micro Convective Accelerometer*, 5th IEEE Conference on Sensors, pp.1353 – 1356.

[18] Dzung Viet Dao, (2003), *Doctoral thesis "Study on Silicon. Piezoresistive 6-DOF Force Moment sensor and application to. fluid Mechanics"*, Ritsumeikan University, Japan.

[19] E. Hild, J. K. Vij, P. Corcoran, G. Végh, (1989), "A graphical method for determining the parameters of a diffusion profile in silicon by infrared reflection spectroscopy", Solid-State Electronics, pp. 69-76

[20] Elena E. Antonova and David C. Looman, (2005), *Finite elements for thermoelectric device analysis in ANSYS*, 24th International Conference on Thermoelectrics ICT 2005, USA, pp. 215- 218.

[21] Ebrahim Abbaspour-Sani, Ruey-Shing Huang, Chee Yee Kwok, (1994), "A linear electromagnetic accelerometer", *Sensors and Actuators A* Vol.44(2), pp. 103-109.

[22] Garcia Valenzuela and M. Tabib-Azar, (1994), *Comparative study of piezoelectric, piezoresistive, electrostatic, magnetic, and optical sensors*, Proc. SPIE, USA, pp. 125–142.

[23] Gabrielson, (1993), "Mechanical-Thermal Noise in Micromachined Acoustic and Vibration sensors", *IEEE Transactions on Electron Devices* Vol. 40(5), pp. 903 – 909.

[24] Graeb H., Mueller D., Schlichtmann U., (2007), *Pareto optimization of analog circuits considering variability*, 18th European Conference on Circuit Theory and Design, pp. 28 – 31.

[25] Hailiang Zhao, Tsu-TianLee, (2003), *Research on multiobjective optimization control for nonlinear unknown systems*, 12th IEEE International Conference on Fuzzy Systems Vol.1, pp. 402 – 407.

[26] Hangyi Jiang, Chen W.R., Hong Liu, (2002), *Techniques to improve the accuracy and to reduce the variance in noise power spectrum measurement*, IEEE Transactions on Biomedical Engineering Vol.49(11), pp. 1270 – 1278.

[27] Harkey J.A., Kenny T.W., (2000), "1/f Noise Considerations For The Design And Process Optimization Of Piezoresistive Cantilevers", *Journal of Microelectromechanical Systems*, Vol. 9, pp. 226 – 235.

[28] Harkey J.A., Kenny T.W., (2000), "1/f noise considerations for the design and process optimization ofpiezoresistive cantilevers", *Journal of Microelectromechanical Systems* Vol. 9(2), pp. 226 – 235.

[29] Harte S., O'Flynn B., Martinez Catala R.V., Popovici E.M, (2007), *Design and implementation of a miniaturized, low power wireless sensor node*, 18th European Conference on Circuit Theory and Design, pp. 894-899.

[30] Hoff L., Elle O.J., Grimnes M., Halvorsen S., Alker H.J., Fosse E., (2004), *Measurements of heart motion using accelerometers*, Proceedings of IEEE Sensors Vol.3, pp. 1353 – 1354.

[31] J.C. Lotters, J. Schipper, P.H. Veltink, W. Olthuis, P. Bergveld, "Procedure for in-use calibration of triaxial accelerometers in medical applications", *Sensors and Actuators A* Vol.68(1-3), pp. 221-228.

[32] J. Ramos, (1997), "Sensitivity enhancement in lateral capacitive accelerometers by structure width optimsation", *Electronics Letters* Vol.33, pp. 384-386.

[33] J. V. Clark, N. Zhou, S. Brown, and K.S.J. Pister, (1998), *Nodal analysis for MEMS design using SUGAR v0.5*, International Conference on Modeling and Simulation of Microsystems, Semiconductors, Sensors and Actuators, Santa Clara, CA, pp. 308-313.

[34] J. V. Clark, D. Bindel, N. Zhou, S. Bhave, Z. Bai, J. Demmel, K. S. J. Pister, (2001), *Advancements in 3D Multi Domain Simulation Package for MEMS*, Proceedings of the Microscale Systems: Mechanics and Measurements Symposium, Portland, pp. 40-45.

[35] Jaeger R.C., Suhling J.C., Carey M.T., Johnson R.W., (1993), "Off-axis sensor rosettes for measurement of the piezoresistivecoefficients of silicon", *IEEE Transactions on Components, Hybrids, and Manufacturing Technology* Vol.16(8), pp. 925 – 931.

[36] Jaeger R.C., Suhling J.C., Ramani R., (1994), "Errors associated with the design, calibration and application of piezoresistive stress sensors in (100) silicon", *IEEE Transactions on Components, Packaging, and Manufacturing Technology, Part B: Advanced Packaging* Vol.17(1), pp. 97 – 107.

[37] Jono K., Hashimoto M., Esashi M., (1994), *Electrostatic servo system for multi-axis accelerometers*, IEEE Workshop on Micro Electro Mechanical Systems, pp. 251 – 256.

[38] Kanda Y., (1982), "A graphical representation of the piezoresistance coefficients in silicon", *IEEE Transactions on Electron Devices* Vol.29(1), pp. 64 – 70.

[39] Kazunori Matsuda, Yozo Kanda, Kazuhisa Yamamura, Katuhisa Suzuki, (1990), "Nonlinearity of piezoresistance effect in p- and n-Type silicon", *Sensors and Actuators A: Physical* Vol.21(1), pp. 45-48.

[40] Kruglick E.J.J., Warneke B.A., Pister K.S.J., (1998), *CMOS 3-axis accelerometers with integrated amplifier*, The Eleventh Annual International Workshop on Micro Electro Mechanical Systems, Heidelberg, Germany, pp. 631 – 636.

[41] Kyung Il Lee, Hidekuni Takao, Kazuaki Sawada, Makoto Ishida, (2003), "Low temperature dependence three-axis accelerometer for high temperature environments with temperature control of SOI piezoresistors", *Sensors and Actuators A* Vol.41(1), pp. 53-60.

[42] Lou E., Bazzarelli M., Hill, D., Durdle N., (2001), *A low power accelerometer used to improve posture,* Canadian Conference on Electrical and Computer Engineering Vol.2, pp. 1385 – 1389.

[43] Masry E., (1991), "Flicker noise and the estimation of the Allan variance", *IEEE Transactions on Information Theory* Vol.37(4), pp. 1173 – 1177.

[44] Maximillian Perez, Andrei M. Shkel, (2006), *Performance Trade-offs of an Interferometric Micro-g Resolution Accelerometer*, IEEE SENSORS 2006, Korea, pp. 1357-1360.

[45] Megson T.H.G., (1996), "Structural and stress analysis", Planta tree Publisher.

[46] Middelhoek S., Noorlag D. J. W., (1992), "Signal conversion in solid-state transducers, Sensors and Actuators" Vol. 2, pp. 211-228.

[47] Mukhiya R., Adami A., Bagolini A., Zen M., Kal S., (2006), *FEM Based Design and Simulation of Bulk Micromachined MEMS Accelerometers with Low Cross Axis Sensitivity*, EuroSime 2006, Italy, pp. 1- 5.

[48] Myer Kutz, (2006), "Mechanical Engineers' Handbook: Instrumentation, Systems, Controls, and MEMS", *John Wiley & Sons, Inc*.

[49] Myers D.S., Meyer J.L., DePasquale P., Hendricks R.W., (2001), *An interactive program for determining junction depths in diffused silicon devices*, Proceedings of the Fourteenth Biennial University/Government/Industry Microelectronics Symposium, pp. 213-221.

[50] N. Zhou, B. Zhu, A. Agogino, K.S.J. Pister, (2001), *Evolutionary Synthesis of MEMS Design*, Proceedings of ANNIE 2001, USA, pp. 197-202.

[51] Pramanik C., Banerjee S., Mukherjee D., Saha H., (2006), *Development of SPICE Compatible Thermal Model of Silicon MEMS Piezoresistive Pressure Sensor for CMOS- MEMS Integration*, the 5th IEEE Conference on Sensors, Korea, pp. 761-764.

[52] Pramanik C., Saha H., (2006), "Piezoresistive pressure sensing by porous silicon membrane", *IEEE Sensors Journal* Vol.6(2), pp. 301 – 309.

[53] Q. Zou, W. Tan, E.S. Kim and G.E. Loeb, (2008), "Single-axis and Tri-axis Piezoelectric Bimorph Accelerometer", *IEEE/ASME Journal of Microelectromechanical Systems* Vol.17(1), pp. 45 – 57.

[54] Ranjith Amarasinghe, Dzung Viet Dao, Toshiyuki Toriyama, and Susumu Sugiyama, (2006), "Simulation, fabrication and characterization of a three-axis piezoresistive accelerometer", *Smart Material and Structure* Vol.15, pp. 1691-1699.

[55] Rodjegard H., Andersson G., (2002), "Design optimization of three-axis accelerometers based on four seismic masses", Proceedings of IEEE Sensors Vol.2, pp. 1099 – 1104.

[56] Roylance L.M., Angell J.B, (1979), "A batch-fabricated silicon accelerometer", *IEEE Transactions on Electron Devices* Vol. 26(12), pp.1911 – 1917.

[57] Rudolf, A.Jornod, J.Bergqvist, H.Leuthold, (1990), "Precision accelerometer with µg resolution", *Sens. Actuator A21/A23*, pp. 297-302.

[58] Sankar A.R., Saini V., Das S., Kal S., (2004), *Temperature drift analysis in silicon micromachined piezoresistive accelerometer*, Proceedings of the IEEE INDICON 2004, India, pp. 561- 563.

[59] Santiram Kal, (2005), *Design and Fabrication of MEMS Accelerometer for Avionics Applications*, Proceedings of International Conference on Smart materials Structures and Systems, Bangalore, India, pp. 140- 146.

[60] Shinogi M., Kato K., Mandai M., Saitoh Y., (1996), *A novel structure of a piezoresistive accelerometer with lateraldetection using precise fabrication techniques*, International Electron Devices Meeting, USA, pp. 769-772.

[61] Smith C.S., (1962), "Piezoresistance Effect in Germanium and Silicon", *Physical Rev.* Vol.94, No.1, pp.42-49.

[62] Spangler C., Kemp C.J., (1996), "Integrated silicon automotive accelerometer", Sens. Actuators A54, pp. 523-529.

[63] Sridhar U., Foster R., (1992), *Temperature coefficient of resistance of piezoresistors*, 5th IEEE Solid-State Sensor and Actuator Workshop, pp. 54-57.

[64] Stephen D. Senturia, (2001), *Microsystem Design*, Kluwer Academic Publishers.

[65] Steve P. Beeby, Graham Ensel, Michael Kraft, (2004), *MEMS Mechanical Sensors*, Artech House Publishers.

[66] SUGAR, http://www-bsac.eecs.berkeley.edu/cadtools/sugar/sugar.

[67] Tabib Azar, A. Garcia-Valenzuela, (1995), "Sensing means and sensor shells: A new method of comparative study of piezoelectric, piezoresistive, electrostatic, magnetic, and optical sensors", *Sensors and Actuators A: Physical* Vol.58(2), pp. 87-100.

[68] T.Mineta, S.Kobayashi, Y.Watanabe, S.Kanauchi, I.Nagakawa, E.Suganuma, M.Esashi, (1995), *Three-axis capacitive accelerometer with uniform axial sensitivities*, Transducer 95, Stokholm, Sweden, pp. 544-577.

[69] T.Velten, P. Krause, E. Obermeier, (1996), *Two-axis Micromachined Accelerometer for Gesture Recognition*, MME'96, pp. 247-250.

[70] Taechung Yi and Chang-Jin Kim, (1999), "Measurement of mechanical properties for MEMS materials", *Measurement Science and Technology* Vol.10, pp. 706-716.

[71] Toshiyuki Toriyama and Susumu Sugiyama, (2002), "Analysis of Piezoresistance in p-Type Silicon for Mechanical Sensors", *Journal of Microelectromechanical Systems* Vol.11(5), pp. 598 – 604.

[72] Thomas Tschan, Nico de Rooij, (1991), Oil-damped piezoresistive silicon accelerometers, TRANSDUCERS '91, pp. 112-114.

[73] Wei Zhang, Yanfeng Zhang, Peiyuan Wan, Yangyuan Wang, (2004), *A novel piezoresistive accelerometer for high accuracy and overload ability*, 7th International Conference on Solid-State and Integrated Circuits Technology Vol.3, pp.1828- 1830.

[74] Van Der Ziel A., Handel P.H., "Xichen Zhu, Kuang Hann Duh, (1985), A theory of the Hooge parameterers of solid-state devices", *IEEE Transaction on Electron Devices* Vol. 32(3), pp. 667-671.

[75] Vijay Varadan, K. J. Vinoy, S. Gopalakrishnan, (2006), *Smart Material Systems and MEMS: Design and Development Methodologies*, John Wiley & Sons Ltd.

[76] Wilson C.J., Beck P.A, (1996), "Fracture testing of bulk silicon microcantilever beams subjected to a side load", *Journal of Microelectromechanical Systems* Vol.5(3), pp.142 – 150.

[77] Witt T.J., (2000), *Using the Allan variance and power spectral density to characterizedc nanovoltmeters*, Conference on Precision Electromagnetic Measurements Digest, pp. 667 – 668.

[78] Xiaomei Yu, Ting Li, Dacheng Zhang, (2004), *Noise-analyzing of piezoresistive silicon materials*, 7th International Conference on Solid-State and Integrated Circuits Technology Vol.3, pp. 2194- 2197.

[79] Yang S.M., Yin T. I., (2007), "Design and analysis of piezoresistive microcantilever for surface stress measurement in biochemical sensor", *Sensors and Actuators B*, pp. 736–744.

[80] Yanhong Zhang, Bingwu Liu, Litian Liu, Zhimin Tan, Zhaohua Zhang, Huiwang Lin, (2006), *A Novel Combined Pressure/Temperature Microsensor*, 1st IEEE International Nano/Micro Engineered and Molecular Systems, China, pp. 1241-1244.

[81] Yao-Joe Yang, Gretillat M.A., Senturia S.D., (1997), *Effect of air damping on the dynamics of nonuniform deformations of microstructures*, TRANSDUCERS'97, Chicago, Vol.2, pp. 1093 – 1096.

[82] Yozo Kanda, (1981), "Piezoresistance Effect of Silicon", *Sensors and Actuators* Vol. A28, pp. 83-91.

[83] Yuan Ma, Robinson A.M., Lawson R.P.W., Bing Shen, Strembicke D., Allegretto W., (1999), *Measuring the deflection of a micromachinedcantilever-in-cantilever device using a piezoresistive sensor*, IEEE Canadian Conference on Electrical and Computer Engineering, pp. 1632 – 1636.

[84] Z. Bai, D. Bindel, J. Clark, J. Demmel, K. Pister, N. Zhou, (2001), *New Numerical Techniques and Tools in SUGAR*, International Conference on Modeling and Simulation of Microsystems, USA..

[85] Xin Zhao, Lei Wang, Yiyong Tan, Guangyi Sun, Guizhang Lu, (2007), *A novel design methodology for MEMS device*, 7th IEEE Conference on Nanotechnology, Hong Kong, pp. 39-44.

LIST OF TABLES

LIST OF FIGURES AND GRAPHS

Design, Simulation, Fabrication and Performance Analysis of a Piezoresistive Micro Accelerometer